
National Laser Users' Facility and External Users' Programs

Under the governance plan implemented in FY08 to formalize the scheduling of the Omega Laser Facility as an NNSA facility, OMEGA shots are allocated by campaign. The majority of the FY09 target shots (56.6%) were allocated to the National Ignition Campaign (NIC), and integrated experimental teams from LLNL, LANL, SNL, and LLE conducted a variety of NIC-related experiments on both the OMEGA and OMEGA EP Laser Systems. Twenty percent (20%) of the FY09 shots were allocated to high-energy-density stewardship experiments (HEDSE) from LLNL and LANL. Under this governance plan, 25% of the facility shots were allocated to basic science experiments. Roughly half of these were dedicated to university basic science, i.e., the National Laser Users' Facility (NLUF) Program, and the remaining shots were allotted to the Laboratory Basic Science (LBS) Program, comprising peer-reviewed basic science experiments conducted by the national laboratories and LLE/FSC.

The Omega Facility is also being used for many experiments by teams from the Commissariat à l'Énergie Atomique (CEA) of France and the Atomic Weapons Establishment (AWE) of the United Kingdom. These programs are conducted on the basis of special agreements put in place by DOE/NNSA and the participating institutions.

The external users during this year included a record 11 collaborative teams that participated in the NLUF Program as shown in Table 120.IX. Ten teams from LLNL, LANL, and LLE were allotted shots under the LBS Program (Table 120.X). Integrated experimental teams from the national laboratories and LLE conducted 851 shots for the NIC, and investigators from LLNL, LANL, and LLE conducted over 232 shots for the HEDSE programs. A total of 56 shots were conducted by scientists from CEA and 35 shots were carried out by scientists from AWE.

Table 120.IX: FY09–FY10 NLUF Projects.

Principal Investigator	Affiliation	Proposal Title
F. Beg	University of California, San Diego	Systematic Study of Fast-Electron Transport and Magnetic Collimation in Hot Plasmas
R. P. Drake	University of Michigan	Experimental Astrophysics on the OMEGA Laser
R. Falcone	University of California, Berkeley	Detailed <i>In-Situ</i> Diagnostics of Multiple Shocks
U. Feldman	ARTEP, Inc.	OMEGA EP-Generated X-Ray Source for High-Resolution 100- to 200-keV Point-Projection Radiography
Y. Gupta	Washington State University	Ramp Compression Experiments for Measuring Structural Phase Transformation Kinetics on OMEGA
P. Hartigan	Rice University	Dynamics of Shock Waves in Clumpy Media
R. Jeanloz	University of California, Berkeley	Recreating Planetary Core Conditions on OMEGA, Techniques to Produce Dense States of Matter
K. Krushelnick	University of Michigan	Intense Laser Interactions with Low-Density Plasmas Using OMEGA EP
R. Mancini	University of Nevada, Reno	Three-Dimensional Studies of Low-Adiabat Direct-Drive Implosions on OMEGA
M. Meyers	University of California, San Diego	Response of BCC Metals to Ultrahigh Strain Rate Compression
R. D. Petrasso	Massachusetts Institute of Technology	Monoenergetic Proton and Alpha Radiography of Laser-Plasma-Generated Fields and of ICF Implosions

Table 120.X: Approved FY09 LBS Experiments.

Principal Investigator	Affiliation	Proposal Title	Facility Required
R. Betti	LLE/FSC	Ultra-Strong Shock and Shock-Ignition Experiments on OMEGA EP	OMEGA EP long pulse/short pulse
H. Chen	LLNL	Electron–Positron Jets	OMEGA EP short pulse/2 beams
J. H. Eggert	LLNL	Powder X-Ray Diffraction on OMEGA: Phase Transitions in Tin	OMEGA
M. B. Hegelich	LANL	Proton and Light Ion Production for Fast Ignition and Warm Dense Matter Applications	OMEGA EP short pulse
D. G. Hicks	LLNL	A New Technique for Efficient Shockless Compression to Several Mbar: Studies Using X-Ray Absorption Spectroscopy	OMEGA 40 beams
A. J. MacKinnon	LLNL	Fast Electron Transport in Hot Dense Matter	OMEGA EP long pulse
H.-S. Park	LLNL	Study of High-Z Material Properties Under Compression Using High Energy Backscatter Diffraction	OMEGA EP long pulse/short pulse
P. K. Patel	LLNL	Fundamental Benchmarking of Relativistic Laser–Matter Interaction Physics	OMEGA EP short pulse
S. P. Regan	LLE	Probing Hydrogen–Helium Warm Dense Matter (WDM) with Inelastic X-Ray Scattering: Toward the Equation of State of Jupiter's Core	OMEGA
W. Theobald	LLE	Integrated Core Heating for Fast Ignition	OMEGA and OMEGA EP

In this section, we briefly review all the basic science activity on OMEGA during FY09, including NLUF and LBS Programs, briefly summarize the FY09 NIC and high-energy-density experiments, and conclude with a summary of CEA and AWE activities.

FY09 NLUF Programs

FY09 was the first of a two-year period of performance for the NLUF projects approved for the FY09–FY10 funding and OMEGA shots. Eleven NLUF projects were allotted OMEGA and OMEGA EP shot time and received a total of 165 shots on OMEGA and 43 shots on OMEGA EP in FY09. Some of this work is summarized in this section. A new solicitation will be issued by the DOE in FY10 for NLUF grants for the period FY11–FY12.

Systematic Study of Fast-Electron Generation and Transport

Principal Investigators: T. Yabuuchi and F. N. Beg (University of California, San Diego)

Co-investigators: H. Sawada (University of California, San Diego); R. B. Stephens (General Atomics); M. H. Key and P. Patel (LLNL); D. Batani (University of Milano, Bicocca); and L. A. Gizzi (IPCF-CNR)

Understanding fast-electron generation and transport in the cone and hot, dense plasma is crucial to the success of the cone-guided fast-ignition scheme. The goal of the University of California at San Diego's NLUF project is to investigate the fast-electron transport in hot plasmas and to demonstrate collimation of fast electrons by an external magnetic field. The project consists of three steps: (1) characterization of fast-electron source and transport through the cone tip; (2) study of fast-electron transport in hot, dense plasmas; and (3) demonstration of fast-electron collimation with an external magnetic field. The first step of the project is described here: a copper wire is attached to the tip of a hollow gold cone to investigate the characteristics of the fast electrons through the tip of the cone after they are generated by the OMEGA EP 10-ps pulse.

Figure 120.52 shows the schematic of the experimental setup of cone/wire shots on the OMEGA EP laser. The one short pulse (interaction pulse) was focused into the cone/wire target. Here, the wire (40- μm diam, 1 mm long) was made of copper and attached to the tip of a gold cone with a 20- μm -thick sidewall capped with 6- μm -thick, 30- μm -inner-diam foil. The detailed target information is shown in the inset of Fig. 120.52. The Cu K α x-ray emission from the wire was diagnosed with a highly oriented pyrolytic graphite (HOPG) spectrometer at

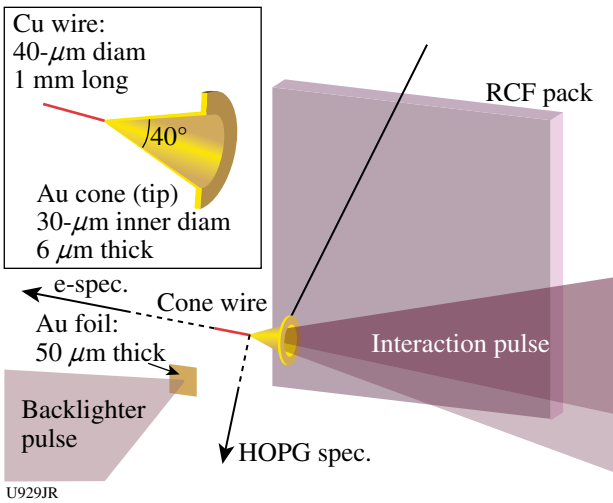


Figure 120.52

Experimental setup for cone/wire shots with proton deflectometry. The directions of the x-ray and electron spectrometers are indicated in the figure. The detailed cone/wire information is shown in the inset.

the normal direction to the wire axis. The energy spectra of the fast electrons were measured along the wire direction, i.e., on the interaction laser axis. In addition, the second short pulse (backlighter pulse) was used to generate a high-energy proton beam to measure the electrostatic field around the cone/wire target using a proton deflectometry technique. The backlighter pulse axis was perpendicular to the axis of the interaction pulse. A stack of radiochromic films (RCF's) was positioned on the

axis of the backlighter pulse to detect protons at various energies, which can provide the electric field information at various timings, depending on the proton energies with a magnification of 9. The detectable proton energy range was 5 MeV to 60 MeV. The temporal resolution of the proton deflectometry was 10 ps to 50 ps. In the experiment, the interaction pulse energy was varied from 260 J to 820 J at a 10-ps pulse duration. At the best-focus position, 80% of the laser energy was contained within a 45-μm-diam spot. The beam-pointing stability was monitored with an x-ray pinhole camera that can also monitor the plasma inside the cone. A 0.7-ps pulse duration was used as the backlighter pulse to minimize the proton-generation time window. The energy of the backlighter pulse was up to 300 J.

The Cu K_α signal was observed on the HOPG spectrometer with a signal-to-background contrast of up to 1.4. The Cu K_α x-ray signal was observed to be linearly dependent on the interaction pulse energy as shown in Fig. 120.53(a). The results indicate that the coupling efficiency from the laser to the K_α photons is quasi-constant in the energy range of 260 J to 814 J; therefore, more electrons pass through the tip of the cone at the higher laser energy. The energy spectra of the vacuum electrons observed at 260-J and 814-J shots are shown in Fig. 120.53(b). Preliminary data analysis of the spectra shows that the slope temperature varies from 1.7 MeV to 2.5 MeV.

Figure 120.54 shows the proton radiographs observed on a shot with 260 J in the interaction pulse. Figure 120.54(a) shows a radiograph taken before the interaction pulse is incident on

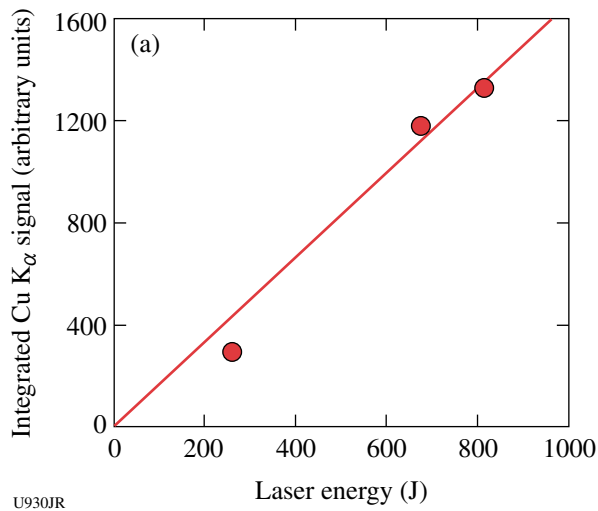
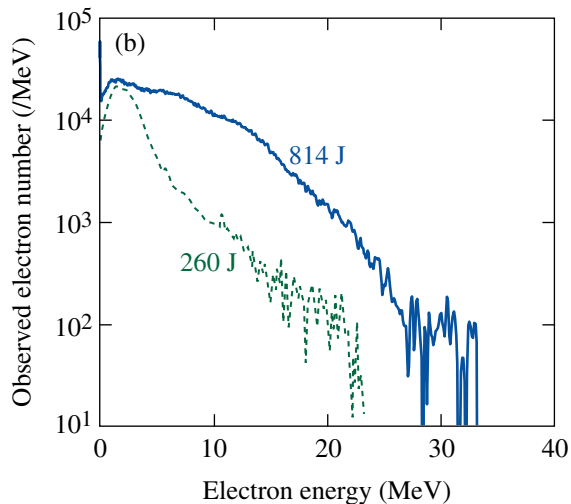


Figure 120.53

(a) Dependence of integrated Cu K_α signal on laser energy. The straight line is a linear fit to the data. (b) Energy spectra of vacuum fast electrons measured on the wire axis.



the cone/wire target by protons with an energy of \sim 18 MeV. The proton beam deflected by the electrostatic field around the target was observed with low-energy protons (5 MeV) as shown in Fig. 120.54(b). Protons were deflected by the electrostatic field only in the vertical direction in the figure because the magnetic field was in the azimuthal direction around the wire and canceled out any deflection. The electrostatic field strength observed in Fig. 120.54(b) was estimated at approximately tens of kV/ μ m using a simple calculation of proton ray tracing. Note that the maximum field strength could be higher than this estimate because the field strength can vary within a much shorter time scale than the temporal resolution of the diagnostic setup. Hybrid/PIC (particle-in-cell) modeling has been performed to investigate the fast electrons propagating through the cone tip. The transport study with such fast electrons in hot, dense plasmas and in an external magnetic field will be performed in the coming year.

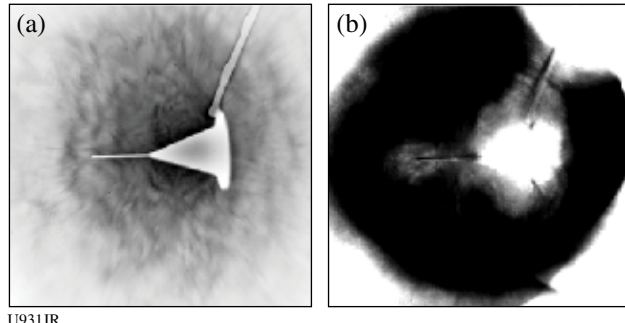


Figure 120.54

Cone/wire target proton backlight images observed with (a) \sim 18-MeV and (b) 5-MeV protons at an interaction pulse energy of 260 J. The 5-MeV protons passed through the cone/wire target at about 200 ps after the interaction pulse hits the target.

Experimental Astrophysics on the OMEGA Laser

Principal Investigator: R. P. Drake (University of Michigan)
Co-investigators: D. Arnett (University of Arizona); T. Plewa (Florida State University); J. Glimm, D. Swesty, X. Li, and A. C. Calder (State University of New York-Stony Brook); I. Sokolov, J. Holloway, and K. Powell (University of Michigan); J. P. Knauer and T. R. Boehly (LLE); and B. A. Remington, H. F. Robey, J. F. Hansen, A. R. Miles, S. H. Glenzer, and D. H. Froula (LLNL)

The OMEGA laser can create conditions of very high energy density that are relevant to astrophysical phenomena. This is feasible because OMEGA can produce pressures greater than 10 Mbar on areas of square millimeters. This project explores the contribution of hydrodynamic instabilities to structure in

supernovae and the dynamics of radiative shock waves. Radiative shock waves produce shocked matter so hot that it radiates away most of its thermal energy. This causes a complex, three-dimensional internal structure to develop, perhaps made even more complex by an instability. This three-dimensional structure is studied using x-ray radiography and other diagnostics. To better diagnose it, a stereoscopic imaging experiment was recently performed.

In the experiment, ten OMEGA laser beams irradiated a beryllium drive disk with UV light for 1 ns. The beams deposited a total energy of \sim 3.8 KJ, giving an average irradiance of $\sim 7 \times 10^{14}$ W/cm², generating an ablation pressure of \sim 46 Mbar in the beryllium drive disk. The ablation pressure first shocked and then accelerated the Be material, which then acted as a piston to drive a shock down a cylindrical shock tube filled with xenon gas. The shock moved through the xenon with an average velocity of the order of 150 km/s, which was fast enough to cause radiative effects to play a dramatic role in the shock dynamics. An additional ten OMEGA laser beams irradiated two vanadium foils on the stereoscopic backlighting target for 200 ps, creating the x rays used to image the shock tube through pinholes. To investigate the radiative shock at different velocities, we varied the drive-disk thicknesses and backlighting times. The two detectors were spaced at 37.4° and collected the x rays onto film backed by image plates. Figure 120.55 shows the images from a single target, taken 1 ns apart.

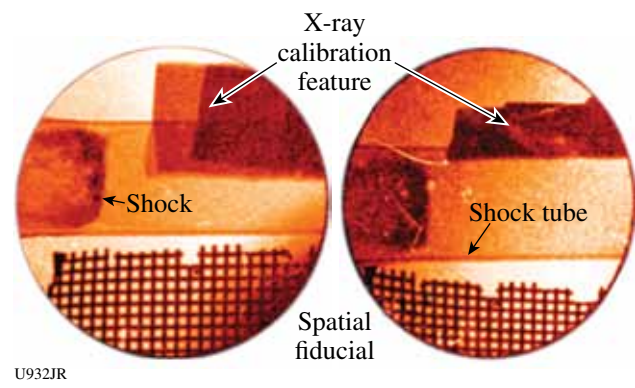


Figure 120.55

Stereoscopic radiographs of a radiative shock in xenon gas. One can see the radiating shock, shock tube, the spatial fiducial, and the x-ray calibration feature used in the experiment. The shock, which moved from left to right within the shock tube, produced dense xenon that absorbed the diagnostic x rays, revealing its structure.

Detailed In-Situ Diagnostics of Multiple Shocks

Principal Investigators: R. W. Falcone (University of California, Berkeley); H. J. Lee (SLAC); and T. Döppner, O. L. Landen, and S. H. Glenzer (LLNL)

X-ray Thomson-scattering diagnostics were employed to measure the electron density and temperature of shock-compressed matter in the Fermi-degenerate state, which is of great interest to test dense-plasma modeling and to address fundamental physics questions such as the equation of state and the structure of dense matter. Powerful laser-produced x-ray sources of 6 keV have been used to probe the dense state, making possible a quantitative *in-situ* diagnostic.¹ A 250- μm -thick beryllium (Be) foil [Figs 120.56(a) and 120.56(b)] was driven by 12 beams smoothed with distributed phase plates (SG-4) in a counter-propagating geometry of heater beams. Laser intensities of $2 \times 10^{14} \text{ W/cm}^2$ in 3-ns-long flat pulses were applied onto each side of the Be.

The Compton-scattering spectrum measured at a scattering angle of $\theta = 140^\circ$ accessing the noncollective scattering regime with $\alpha = 0.4$ and $k = 5.88 \text{ \AA}^{-1}$ shows a parabolic spectrum down-shifted in energy from the incident radiation by the Compton effect;² the shift is determined by the Compton energy $E_C = h^2 k^2 / 2m_e = 130 \text{ eV}$. The theoretical fits to the measured spectra in Figs. 120.56(c) and 120.56(d) show that the electron density (n_e) changes with delay time. Radiation-hydrodynamic calcula-

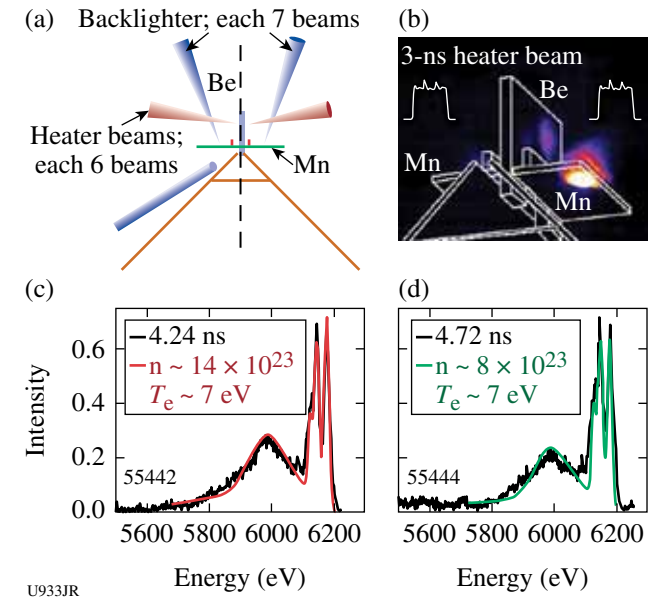


Figure 120.56
(a) Target configuration and (b) time-integrated image for $E > 2 \text{ keV}$ showing the emission produced by heater and probe beams. Scattering data and fit at (c) 4.24 ns and (d) at 4.72 ns.

tions using Hyades estimate the collision of two shocks around 4.3 ns. Calculated spectra using the theoretical form factor indicate compression by a factor of 5 with $n_e \sim 1.4 \times 10^{24} \text{ cm}^{-3}$ by a collision of counter-propagating shocks. Further analysis will address the density and temperature evolution according to the shock propagation.

OMEGA EP-Generated X-Ray Source for High-Resolution 100- to 200-keV Point-Projection Radiography

Principal Investigator: U. Feldman (Artep Inc.)

During the first three months of this NLUF project (which began 15 December 2008) the OMEGA EP transmission crystal spectrometer (ECS) was designed and underwent the required design reviews that assured compliance with the Omega EP Facility requirements. The small standoff distance (25.4 cm) between the target chamber center (TCC) and the ECS crystal made it necessary, on one hand, to place massive shielding fairly close to the TCC as protection from the harsh OMEGA EP hard x-ray radiation environment and, on the other hand, to ensure that the total instrument weight would not exceed the 100-lb limit and that the instrumental center of gravity would be within the TIM's (ten-inch manipulator's) allocated position. The competing requirements forced a totally new spectrometer design.

During May and June the spectrometer parts were machined and assembled and the crystal was cut and polished. In mid-July the crystal was installed and the spectrometer was aligned using the NIST 400-keV industrial tungsten x-ray source. Figure 120.57 shows the spectrometer at the NIST facility and the tungsten spectra recorded on the Rowland circle and at 20 in. and 40 in. from it. On 17 July 2009 the ECS was shipped to LLE for final checks.

On 26–27 August, the ECS was placed in TIM-13 and recorded data from 14 shots. The first shot of each day was at an energy of 35 J to 40 J and a duration of 9 ps to 10 ps; the remainder of the shots were at ~1000 J and 9 ps to 10 ps. Additional information on the shots is provided in Table 120.XI. The low-energy shots, which were focused on a thin foil of Gd, produced clean spectra; on the high-energy shots, however, the spectra were obscured by high background emission. The bright background emission was eventually identified as fairly soft x-ray radiation that was scattered from the general direction of the center of the target chamber. The scattered soft x-ray radiation was eventually removed from the spectra by a 1.2-mm-thick aluminum strip that was placed in front of the image plate and acted as a soft x-ray filter. Spectra from a Gd foil target are shown in Fig. 120.58.

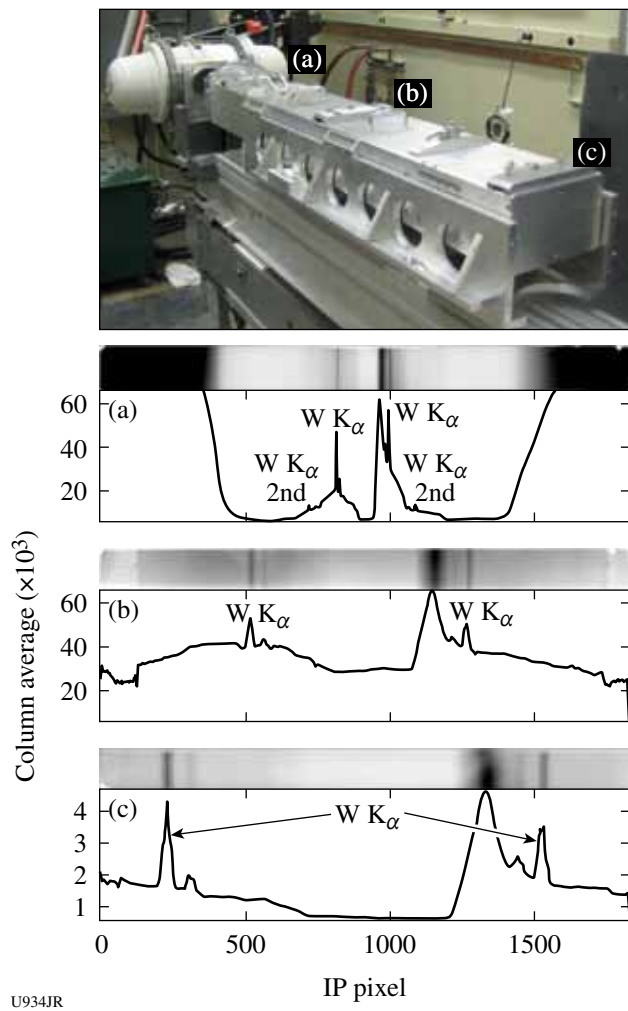


Figure 120.57

The ECS spectrometer at the NIST x-ray facility and sample x-ray spectra at IP positions (a), (b), and (c), on the Rowland circle and at 20 and 40 in. from it, respectively.

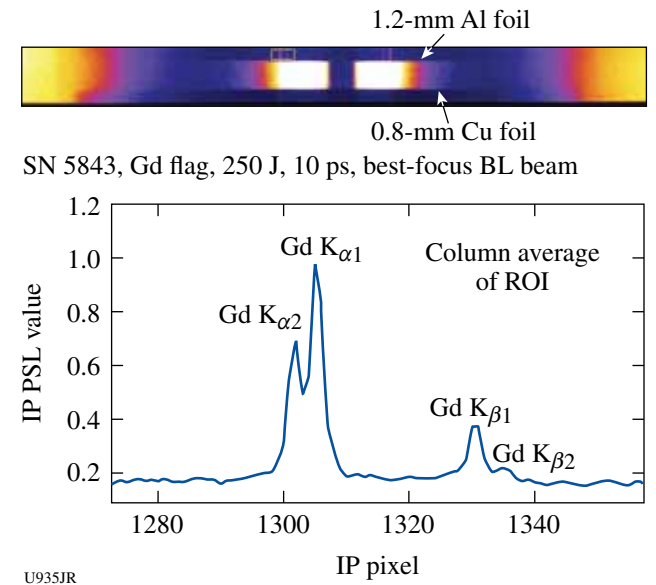


Figure 120.58

X-ray spectra on the ECS from a Gd foil target.

Table 120.XI: Shots on OMEGA EP within PPRad-EP-09, 26–27 August 2009.

Shot numbers	Beam energy (J)	Pulse	Target	Target description	RID	Results
5827	36	9 to 10 ps	FEP-8	Dy foil	29390	Data on ECS, TCS
5828	984	9 to 10 ps	Al-7	Hf foil	28653	No lines
5829	986	9 to 10 ps	Al-1	Ho Dy Tb	29384	No lines
5831	980	10 ps	FEP-2	Ho Dy Tb	29385	No lines
5833	987	10 ps	FEP-9	Dy foil	29386	Lines on TCS
5834	488	9 ps	Al-2	Ho Dy Tb	29388	No lines
5835	486	9 ps	FEP-1	Ho Dy Tb	29389	No lines
5839	35	10 ps	Gd flag	$1 \times 1 \times 0.127$ mm	29404	Lines
5840	982	10	Gd flag	$1 \times 1 \times 0.127$ mm	29405	Lines on all
5841	998	10	Au flag	$2 \times 2 \times 0.05$ mm	29410	No lines on ECS
5842	990	9	Gd flag	$1 \times 1 \times 0.127$ mm	29411	Lines maybe on ECS
5843	249	10	Gd flag	$1 \times 1 \times 0.127$ mm	29412	Nice lines on ECS
5844	975	9	Au flag	$2 \times 2 \times 0.05$ mm	29413	TCS in TIM 13
5845	1053	9	Au flag	$2 \times 2 \times 0.05$ mm	29414	Au lines on ECS

Preliminary results indicate that although the laser was focused to about $50\text{ }\mu\text{m}$, the size of the emitting source was significantly larger ($\sim 400\text{ }\mu\text{m}$).

During September the front end of the three image plate holders was modified by adding a layer of 0.5- to 1.0-mm aluminum. Additional shielding will be provided between the crystal and the TCC. It is expected that these additions will greatly reduce or completely eliminate the scattered radiation problem.

Second-Year Plans

The plan for the second year is to replace the image plate at the 60-in. location, which has pixel sizes of $100\text{ }\mu\text{m}$ or larger, with a pair of electronic detectors that will have a pixel size of the order of $\sim 25\text{ }\mu\text{m}$. The design of the electronic system is in progress. The design change will be implemented on the ECS before the next scheduled run on the OMEGA EP laser in July 2010.

Artep Inc., as part of an earlier project that was associated with measurements of hard x-ray sources on the sun, developed a Soller collimator that consisted of tens to hundreds of foils stacked together. The collimator's pitch (foil thickness and space) is as small as $50\text{ }\mu\text{m}$. Attempts will be made to manufacture and install such a collimator in the optical pass. It is expected that the collimator will not only prevent scattered radiation from reaching the detector but more importantly will provide spectra with spatial resolution of the order of $30\text{ }\mu\text{m}$ at the source.

Ramp Compression Experiments for Measuring Structural Phase Transformation Kinetics on OMEGA

Principal Investigators: T. S. Duffy, J. Wang, and G. Finkelstein (Princeton University); R. F. Smith, J. H. Eggert, P. M. Celliers, D. Braun, and M. Bastea (LLNL); T. R. Boehly (LLE); and Y. M. Gupta (Washington State University)

This proposal was awarded 1.5 shot days on OMEGA in FY09 to explore phase transformations and their associated kinetics in new high-pressure regimes (200 to 500 GPa). These initial shots were focused on two materials that are very important in the study of planetary science: quartz and Fe. To keep these samples in the solid phase (i.e., avoid melt), it is important to minimize the temperature rise during compression. To achieve this, the target package was designed to launch a ramp compression wave into the sample of interest. Here, the compression is quasi-isentropic and the temperature is much smaller than for comparable pressures achieved through shock compression. As shown in Fig. 120.59(a), a composite pulse

shape of $\sim 10\text{-ns}$ duration (18 beams) from the OMEGA laser was used as input into a gas-filled halfraum. This generated a time-dependent x-ray drive, which, via a $20\text{-}\mu\text{m}$ diamond abla-

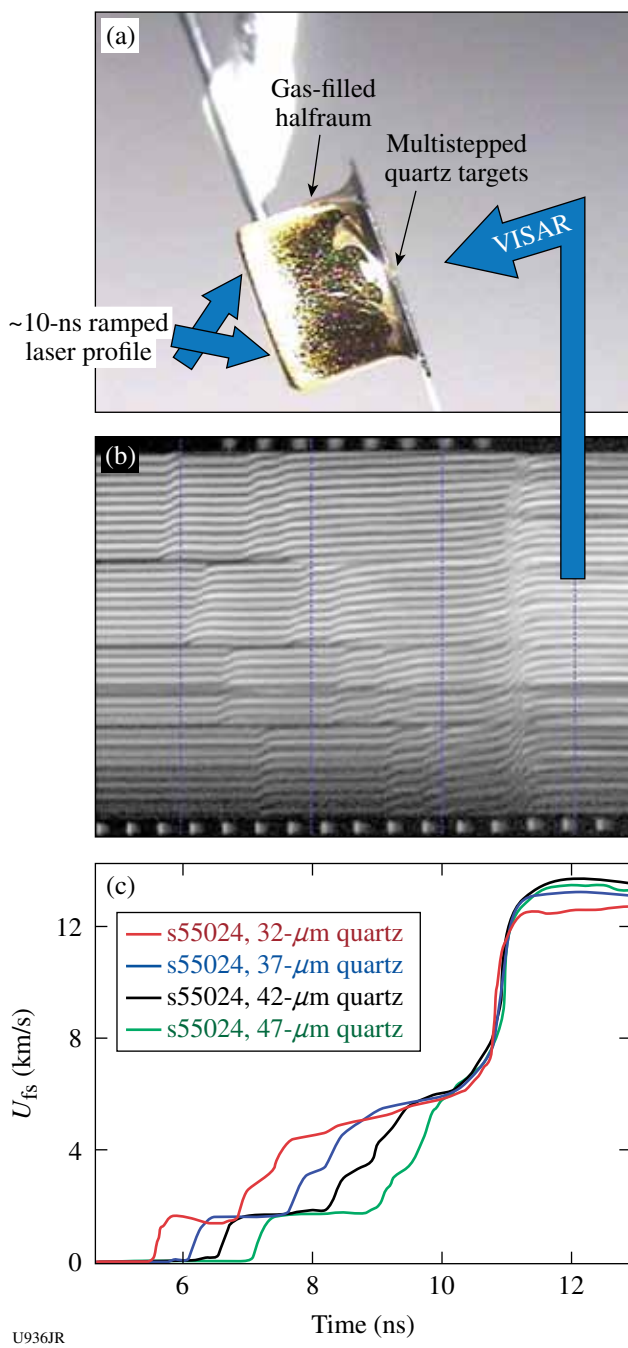


Figure 120.59

(a) A 10-ns ramped laser drive (18 beams) was used to compress a multistep quartz target without shock. (b) The free-surface velocity was recorded using a velocity interferometer (VISAR). (c) The structured free-surface velocity profiles contain information with respect to phase transformations.

tor, launched a ramp compression wave into a multisteped quartz sample. The transmitted compression wave was recorded with a line-imaging velocity interferometer [i.e., velocity interferometer system for any reflector (VISAR), a.k.a. active shock breakout diagnostic] for each step [Fig. 120.59(b)]. These free-surface velocity profiles (U_{fs}) are shown in Fig. 120.59(c). Here the peak velocity of ~ 14 km/s was equivalent to a peak pressure of ~ 260 GPa. The structured nature of these profiles was consistent with the material undergoing one or more structural phase transformations as the pressure within the sample was steadily increased.

In addition to quartz, multisteped Fe samples (Fig. 120.60) were also shot. The target design is described in Fig. 120.59(a). The main difference between the quartz and Fe designs was that each had a unique composite laser-pulse profile, which was optimized from the material's equation of state. The composite pulse shape for Fe is shown in Fig. 120.60(a). This pulse shape resulted in the velocity profiles in a 40-/47-/54-/61- μm multisteped Fe sample shown in Fig. 120.60(b). Here, the peak velocity of 7.1 km/s corresponds to a peak pressure of ~ 250 GPa.

In FY09 a total of 16 shots were taken for this experiment. Analysis is ongoing for both the quartz and Fe data sets to extract equation-of-state (stress-density) and phase-transformation information. Future campaigns will focus on optimizing the design to ramp compress to peak pressures exceeding 5 Mbar (500 GPa). For reference the peak pressure at the center of the Earth is ~ 360 GPa.

Laboratory Experiments of Supersonic Astrophysical Flows Interacting with Clumpy Environments

Principal Investigator: P. Hartigan (Rice University)
Co-investigators: R. Carver and J. Palmer (Rice University); J. M. Foster, P. A. Rosen, and R. Williams (AWE); B. H. Wilde and M. Douglas (LANL); A. Frank (University of Rochester); and B. E. Blue (General Atomics)

Strong shock waves occur in many astrophysical systems, and the morphology of the emission lines that occur from the hot gas behind these shocks is often highly clumpy. The objective of this sequence of NLUF experiments is to develop scaled laboratory experiments to study the hydrodynamics of clumpy supersonic flows. The laboratory work complements new astrophysical images from the Hubble Space Telescope that were motivated by the results of a previous NLUF program.

In the past year, a new target concept was designed and tested in which several dozen 130- μm -diam sapphire spheres were embedded within a cylindrical foam target and a strong shock was propagated through this composite. We also compared how the shock propagation differs between a highly clumped target and a uniform one with the same overall density. The shots were successful, and we were able to observe the small clumps as they were entrained within the passing shock. This situation has a close astrophysical analog in many outflows from young stars (see Fig. 120.61).

In the last year the Astrophysical Journal accepted a paper by this collaboration that describes the results from the previous set of experiments examining the shock waves that occur when a collimated jet deflects from a single large obstacle.

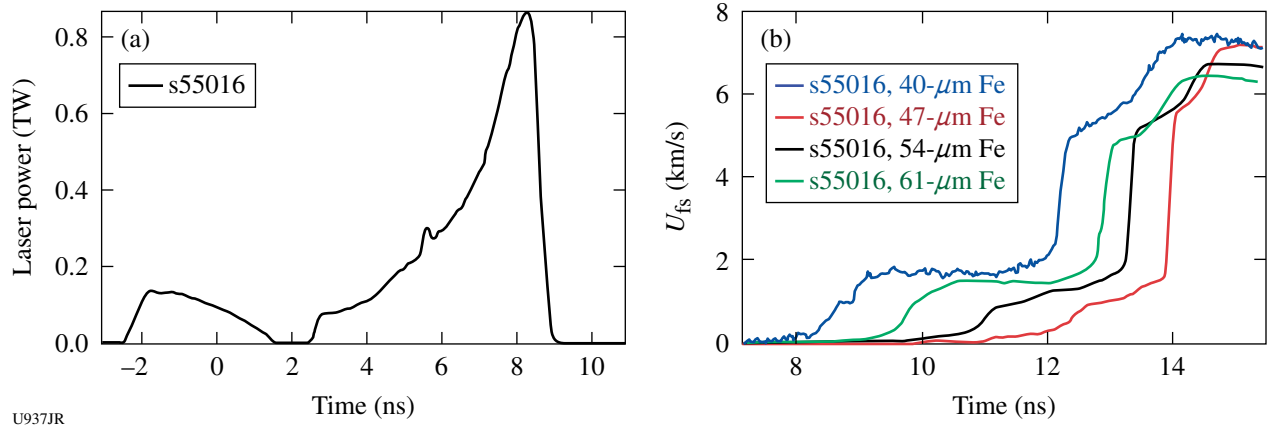


Figure 120.60

(a) Composite laser pulse shape (18 beams) was used to compress a multisteped Fe target without shock. (b) The free-surface velocity was recorded using a velocity interferometer (VISAR). Peak pressures of 3 Mbar were achieved in the Fe sample.

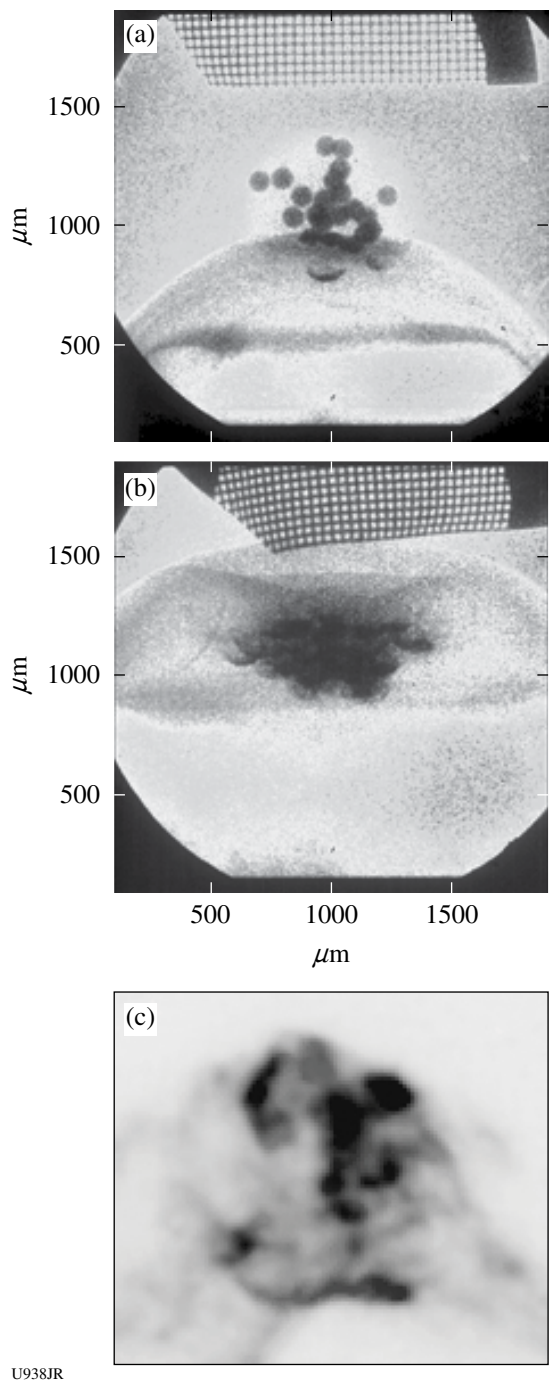


Figure 120.61

[(a),(b)] A strong bow shock propagates through a foam within which are embedded numerous sapphire spheres. Small bow shocks form around each of the spheres as they are overrun and entrained by the main shock wave. The scales are in microns, and the herringbone pattern at the top is a grid used to verify the scale of the images. (c) The astrophysical analog, HH 47, as observed with the Hubble Space Telescope. In all cases the clumps are embedded in a flow that moves from the bottom to the top in the figures.

FY09 Low-Density Plasma Interactions

Principal Investigators: L. Willingale, K. Krushelnick, and A. Maksimchuk (University of Michigan); P. M. Nilson, C. Stoeckl, and T. C. Sangster (LLE); and W. Nazarov (University of St. Andrews)

The propagation of relativistically intense laser pulses into near-critical-density plasma has been shown to be influential on the rear-side proton acceleration,³ and it is of interest for fast-ignition scenarios to determine laser penetration.^{4,5} Investigations of proton acceleration and laser propagation using the OMEGA EP laser (1000 J, 10 ps, $2 \times 10^{19} \text{ W/cm}^2$) interacting with low-density targets have been performed. Very low density, submicron-pore-size CHO foam targets (3 to 100 mg/cm³) produce plasmas of between 0.9 n_c and 30 n_c , where n_c is the nonrelativistic critical density. Proton beams are observed from the rear side to have maximum energies of up to 51 MeV.

Also, proton radiography, which can image quasi-static electromagnetic fields and density perturbations, is used to investigate the interaction of the 1000-J, 10-ps laser pulse interaction with a 1.5- n_c plasma. A schematic of this experiment is shown in Fig. 120.62. Using the second OMEGA EP short-pulse beam (700 fs, 250 J) to create the proton beam (proton energy of up to 60 MeV) and detecting the different proton energy images using a radiochromic film stack make it possible to obtain a picosecond resolution “movie” of the 10-ps laser interacting

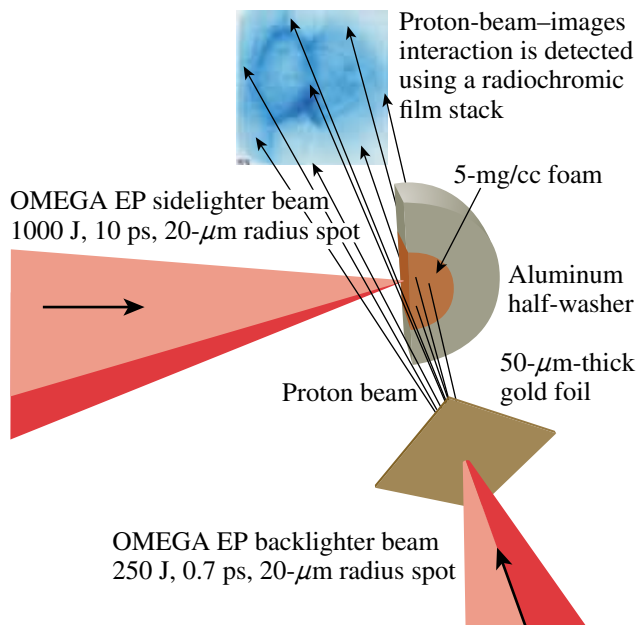


Figure 120.62

Experimental setup for the proton radiography.

with the foam target. The transit time from the proton source foil to the interaction means the different energy protons pass the main interaction at different times. The technique also requires that the interpulse timing be known accurately, which was verified using the ultrafast x-ray streak camera. Examples of the proton radiographs are shown in Fig. 120.63. The most-striking feature is the rapidly expanding front, back toward the laser from the target surface. It is traveling at a velocity of up to $1 \times 10^8 \text{ ms}^{-1}$, which corresponds to proton energies of about 50 MeV. Filamentary structures are observed where the laser has passed through the pre-plasma.

Three-Dimensional Studies of Low-Adiabat Direct-Drive Implosions on OMEGA

Principal Investigator: R. Mancini (University of Nevada, Reno)

Determining the spatial structure of implosion core temperature conditions is of current interest in inertial confinement fusion experiments. Three methods have been developed and tested in OMEGA direct-drive implosions to extract temperature spatial profiles from the analysis of narrowband

x-ray images recorded with a DDMMI instrument. The targets consisted of plastic shells filled with deuterium gas and a trace amount of argon for diagnostic purposes and driven with a low-adiabat $\alpha \sim 2$ pulse shape. The analysis methods treat space integration and radiation transport effects with different levels of approximation.

The emissivity ratio of $\text{Ly}_\beta/\text{He}_\beta$ argon lines is strongly dependent on electron temperature T_e but only weakly dependent on electron density N_e ; therefore, it can be used as a temperature diagnostic. The first method considers the ratio of $\text{Ly}_\beta/\text{He}_\beta$ image intensities. If we neglect the radiation transport effect, each intensity point on the image plane can be interpreted as the line integral of the emissivity along a given chord in the plasma source. Therefore, the ratio of $\text{Ly}_\beta/\text{He}_\beta$ intensities on the image plane corresponds to the ratio of average emissivities along chords in the core, and this ratio can be converted into an average or effective electron temperature T_e integrated along the chord. The result of this analysis is displayed in Fig. 120.64. The x and y coordinates in the surface plot correspond to the coordinates on the image plane. The

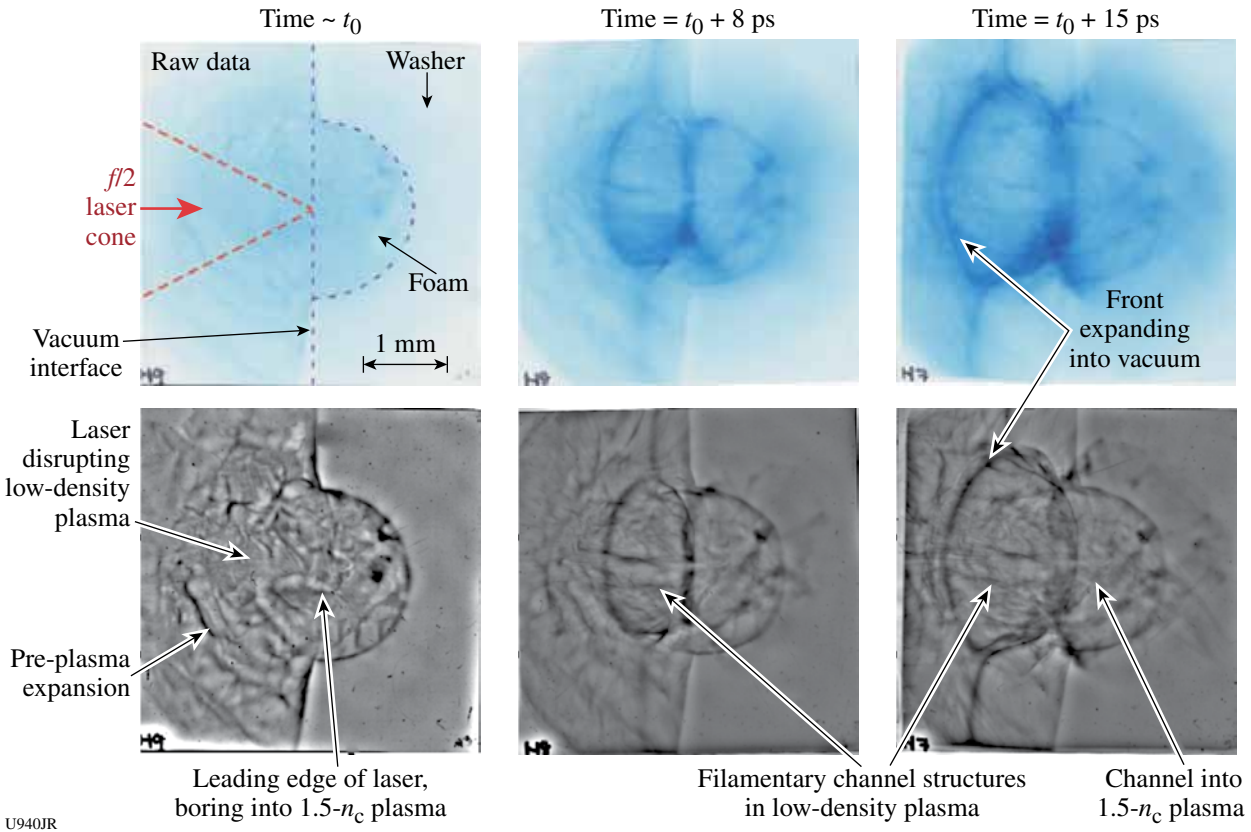


Figure 120.63

Proton images from a single shot of the 1000-J, 10-ps laser (coming in from the left) interacting with the $5\text{-mg}/\text{cm}^3$ foam target. The top row shows the raw data; the bottom row shows the same images enhanced to bring out the features.

electron temperature T_e varies in the range from 900 eV near the core edge to 1400 eV in a region off core center. We note that no symmetry assumptions or geometry inversions are required to perform this analysis.

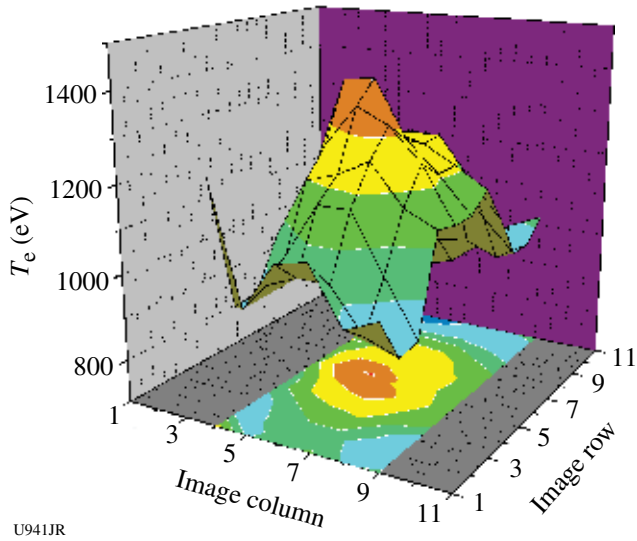


Figure 120.64
Electron-temperature T_e spatial distribution obtained from the ratio of $\text{Ly}_\beta/\text{He}_\beta$ image intensities.

The second method splits the core into a collection of core slices and uses an Abel inversion procedure for each core slice to go from intensity distribution on the image plane to emissivity profile in the plasma source. The Abel inversion unfolds the line integration corresponding to chords in each core slice to yield local emissivity in the core slice, but it still assumes negligible radiation-transport effects. Also, the application of the Abel inversion procedure requires local axial symmetry in each core slice. To satisfy this condition, intensity profiles associated to a given core slice must be made symmetric about a suitable center point. This operation partially removes some of the asymmetries observed on the image, thereby yielding Abel-inverted emissivities as a function of radial coordinate r in the core slice. As a result, the ratio of Abel-inverted $\text{Ly}_\beta/\text{He}_\beta$ emissivities can be converted into a spatial profile of T_e as a function of the radial coordinate in the core slice, i.e., $T_e(r)$. The collection of $T_e(r)$ profiles from all core slices represents a quasi-three-dimensional map of the electron-temperature spatial distribution. The result of this analysis is shown in Fig. 120.65. The x and y coordinates in the surface plot now correspond to core slice label and a projection of the radial coordinate in the core slice on the image plane. While this analysis still neglects the radiation-transport effect, the unfolding of the chord line integration via the Abel inversion results

in an electron temperature that ranges from about 900 eV near core edge to 1900 eV inside the core but off the core center. This temperature distribution is axially symmetric in each core slice but it still has some of the asymmetry present in the image data.

Finally, the third method is an attempt to unfold both the chord line integration and the radiation-transport effect. As in the second method, the core is split into slices and each core slice is assumed to be axially symmetric. Then, a multi-objective Pareto genetic algorithm is used to drive a search in parameter space with the goal of finding the temperature and density profiles that yield the best simultaneous and self-consistent fits (i.e., approximations) to three objectives: the He_β image intensity distribution, the Ly_β image intensity distribution, and the space-integrated line spectrum. Alternatively, the $\text{Ly}_\beta/\text{He}_\beta$ image intensity ratio can also be used as an objective instead of one of the image intensities. Optimal fits are obtained by following up the genetic algorithm search with a “fine-tuner” step driven by a nonlinear least-squares minimization algorithm. The image intensity distribution on the image plane is approximated by transporting the line radiation, one photon energy at a time, inside the core slice via an integration of the radiation transport equation. The result of this analysis is shown in Fig. 120.66. Accounting for both space integration and radiation transport effects yields a temperature spatial distribution in the core that spans the range from 900 eV near core edge to 2250 eV inside the core, resulting in a temperature spatial structure with the steepest gradients. Therefore, neglecting space integration and radiation transport effects leads to a

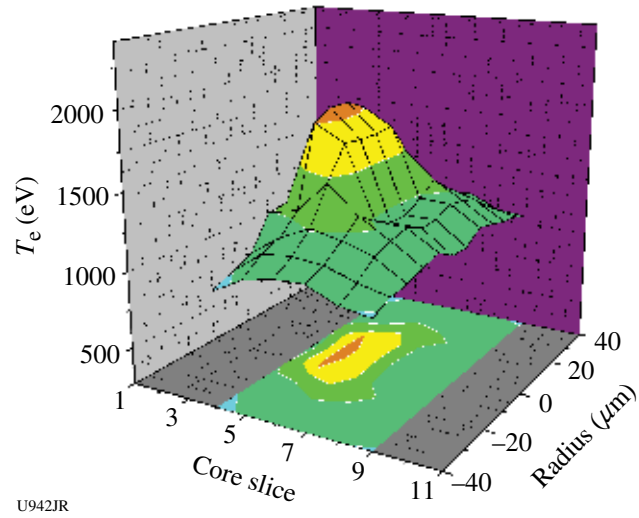


Figure 120.65
Electron-temperature T_e spatial distribution obtained from the ratio of $\text{Ly}_\beta/\text{He}_\beta$ Abel-inverted emissivities.

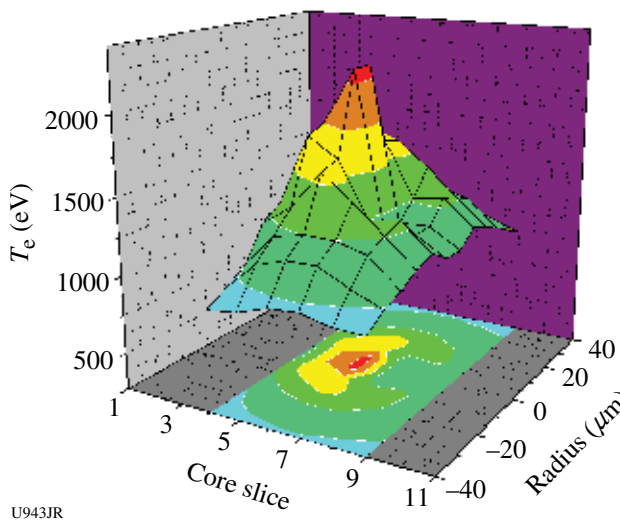


Figure 120.66

Electron-temperature T_e spatial distribution obtained from a search and reconstruction method driven by a Pareto genetic algorithm.

temperature spatial structure characteristic of the shallowest spatial gradients, while taking both effects into account yields a spatial structure with the steepest spatial gradients. Work is in progress to extend these methods to account for image data recorded simultaneously along three lines of sight with three DDMMI identical instruments.

Proton Radiography of Direct- and Indirect-Drive ICF Experiments and HEDP Plasmas

Principal Investigators: R. D. Petrasso and C. K. Li

(Massachusetts Institute of Technology)

Co-investigators: F. H. Séguin and J. A. Frenje (MIT); J. P. Knauer and V. A. Smalyuk (LLE); J. R. Rygg and R. P. J. Town (LLNL).

MIT's NLUF Program has continued an ongoing series of experiments utilizing charged-particle radiography in the study of plasmas and transient electromagnetic fields generated by the interactions of OMEGA laser beams with plastic foils, direct-drive inertial confinement fusion (ICF) target capsules, hohlraums, indirectly driven ICF targets, and plastic or metal foils combined with foam cylinders (for laboratory-scaled astrophysical jets). This work, involving novel studies of field instabilities, magnetic reconnection, ICF implosion dynamics, and self-generated electromagnetic fields in ICF implosions and hohlraums, has already resulted in many publications, including six in Physical Review Letters^{6–11} and one in Science,¹² as well as several invited talks^{13–21} and many contributed talks at conferences. While most of the experiments have

used exploding-pusher backscatterers on OMEGA to produce monoenergetic protons and alpha particles,²² work this year used protons from backscatterer foils driven by OMEGA EP short-pulse beams. One experiment involved the simultaneous use of both types of backscatterer.

Illustrating one of these important series of experiments, Fig. 120.67 shows the basic setup that was used for the first observations of self-generated fields associated with laser-irradiated hohlraums.¹⁰ An exploding-pusher backscatterer was driven by 21 OMEGA beams, while two hohlraums to be studied were driven by ten beams each (the isotropic emission of the backscatterer makes it possible to image multiple objects simultaneously in different directions), as shown in Fig. 120.67(a). The backscatterer produced short bursts (~130 ps) of monoenergetic protons at two different energies (3.3 MeV and 15 MeV), as shown in Fig. 120.67(b), and the special detector pack based on CR-39 nuclear track detectors made it possible for separate images to be recorded at each energy. As indicated in the left part of Fig. 120.67(a), a metal mesh was placed on the end of each hohlraum nearest the backscatterer; this divided the incident particles into beamlets whose deflec-

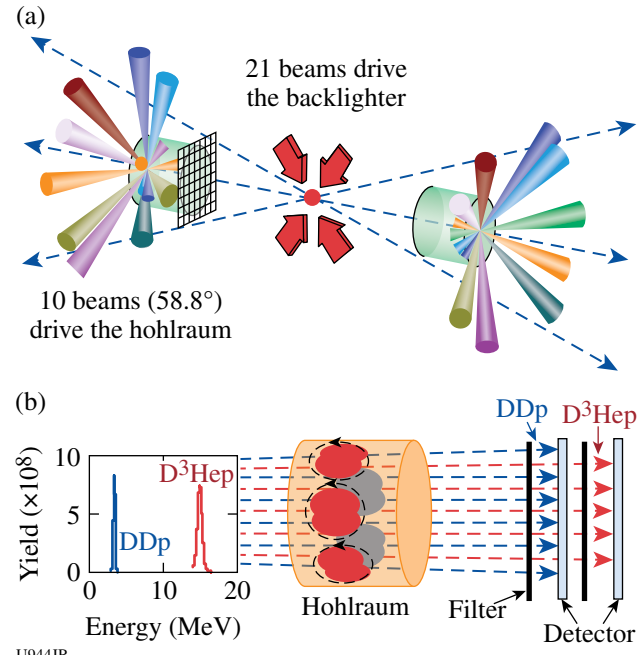
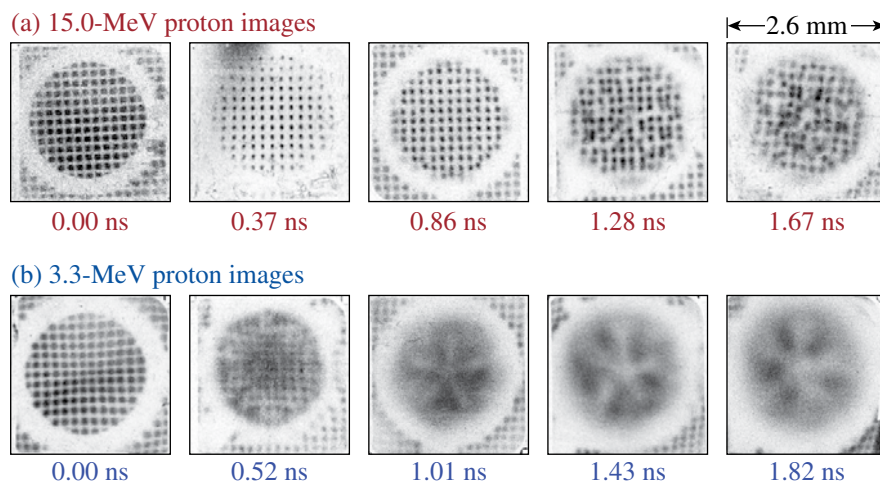


Figure 120.67

(a) Experimental setup, with proton backscatterer, subject hohlraums, and laser beams. (b) Typical energy spectrum and CR-39 detector pack. The distance between the backscatterer and the mesh (detector) was 0.7 (27) cm. Filters in the detector pack were carefully chosen so that 3.3-MeV and 15-MeV protons were recorded on the front and back detectors, respectively.

tions in the image plane could be measured for quantification of particle trajectory bending within the hohlraum caused by electric and/or magnetic fields.

Figure 120.68 shows sequences of proton images covering a time period from the beginning of the laser pulse ($t = 0$ ns) to 0.8 ns after it was turned off ($t \approx 1.8$ ns). At earlier times ($t \geq 0.9$ ns) the beamlet arrays in the 15-MeV images [Fig. 120.68(a)] show minimal displacement by fields or plasma, but beamlets have different sizes at different times, reflecting the presence of an E field of $\sim 2 \times 10^9$ V m $^{-1}$ at ~ 0.37 ns that then decays away. At later times the 15-MeV beamlets show some chaotic spatial structure, indicating that their trajectories have been affected by large-field and plasma effects. In the 3.3-MeV images, beamlet arrays are coherently distorted by $t = 0.52$ ns and disappear altogether (due to stronger deflections) at later times. Quantitative analysis of the beamlet displacements indicates the presence of B fields with peak values of $\sim 10^6$ Gauss. The five-prong asterisk-like fluence pattern in the 3.3-MeV proton images at $t \geq 1.01$ ns was shown to be a consequence of the staggered distribution of laser beams on each hohlraum wall. The ten beams were grouped into five pairs that produced five plasma bubbles; the asterisk pattern was caused by scattering of the protons in Au-plasma jets between the bubbles shooting inward from the hohlraum wall at about \sim Mach 4 (~ 1000 μ m ns $^{-1}$). The Au density was inferred to be ~ 10 mg cm $^{-3}$ (note that this should not occur in an ignition hohlraum, where a gas fill would impede the jets). These experimental results have important implications for understanding the precise conditions and plasma dynamics inside vacuum hohlraums and provide an impetus for the further development of 3-D multifluid codes with self-consistent field generation.



U945JR

FY09 Laboratory Basic Science Programs

Ten proposals were approved and allocated 25 shot days on the Omega Facility in FY09 (Table 120.X). Unfortunately, because of the DOE funding shortfall in FY09, only 17 days (109 shots) of LBS experiments were actually funded and carried out during this fiscal year. The FY10 solicitation for the LBS Program resulted in 25 proposals with shot requests totaling 63.5 shot days. After peer review by an independent committee, 13 LBS proposals have been recommended for 29 shot days in FY10. Three additional shot days were recommended and approved for FY09 make-up shots. The approved FY10 LBS proposals are listed in Table 120.XII. This section includes brief summaries of LBS experiments carried out in FY09.

Electron–Positron Jets

Principal Investigators: H. Chen and S. C. Wilks (LLNL)
Co-investigators: J. F. Myatt and C. Stoeckl (LLE);
and E. Lang (Rice University)

On 16 April 2009, an LLNL/LLE team performed a Laboratory Basic Science experiment on the OMEGA EP Laser System to study positron production in high-intensity laser interactions with high-Z targets. The OMEGA EP backlighter produced ~ 1 kJ in a 10-ps laser pulse that interacted with a 1-mm-thick Au target. The positrons that were emitted from the rear side of the target were measured with a magnetic positron spectrometer. A quasi-monoenergetic positron beam was observed with a maximum energy of ~ 20 MeV as shown in Fig. 120.69. It is estimated that 10^{12} positrons were produced. This is a factor of ~ 10 more than were produced with a 260-J, 10-ps laser in LLNL experiments.²³ It was anticipated that the number of positrons produced would scale approximately with the laser energy.²⁴ The quasi-monoenergetic positron

Figure 120.68

Radiographs of a laser-driven, vacuum Au hohlraum at different times, taken with (a) 15.0-MeV and (b) 3.3-MeV protons, illustrating spatial structure and time evolution of proton deflection and beamlet size. Pairs of images in (a) and (b) were taken in the same shot, but they represent different sample times because of different proton velocities. In each image, darker means higher fluence; the gray-scale mapping is different in each image to account for the different backlighter yields.

Table 120.XII: Approved FY10 LBS Experiments.

Principal Investigator	Affiliation	Proposal Title	Facility Required
R. Betti	LLE/FSC	Integrated Shock-Ignition Experiments on OMEGA	OMEGA
P. M. Celliers	LLNL	Measurement of the Viscosity of Shock-Compressed Fluids: Studies of Water and Silica	OMEGA
H. Chen	LLNL	Producing Pair Plasma and Gamma-Ray Burst Using OMEGA EP	OMEGA EP
D. E. Fratanduono	LLE	Optical Properties of Compressed LiF	OMEGA and OMEGA EP
D. H. Froula/J. S. Ross	LLNL	First Observations of Relativistic Plasma Effects on Collective Thomson Scattering	OMEGA
S. H. Glenzer	LLNL	Capsules Adiabat Measurements with X-Ray Thomson Scattering	OMEGA
D. G. Hicks	LLNL	Ramp and Multi-Shock Compression of Iron to Several Megabars: Studies Using Extended and Near Edge X-Ray Absorption Spectroscopy	OMEGA
H.-S. Park	LLNL	Study of High-Z Material Properties under Compression Using High-Energy Backscatter Diffraction	OMEGA EP
P. K. Patel	LLNL	Benchmarking Laser-Electron Coupling at Fast Ignition-Relevant Conditions	OMEGA EP
S. P. Regan	LLE	Validating Inelastic X-Ray Scattering from H and H/He Warm Dense Matter with Shock Velocity Measurements: Toward the Equation of State of Jupiter's Core	OMEGA
R. Smith/J. H. Eggert/ S. M. Pollaine	LLNL	Phase Transformation Kinetics	OMEGA
C. Stoeckl/ W. Theobald/W. Seka	LLE	Channeling in Long-Scale-Length Plasmas	OMEGA EP
W. Theobald	LLE	Integrated Core Heating for Fast Ignition	OMEGA and OMEGA EP

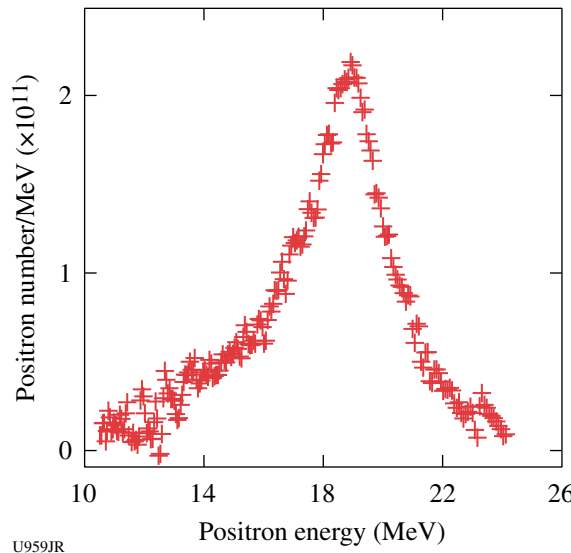


Figure 120.69
Positron spectrum measured on the OMEGA EP laser.

spectrum is likely a cause of positron acceleration from the sheath formed by escaping electrons on the rear surface of the target. The differences between the two experiments will be studied to understand the consequences of these results. The positron-production rate during the laser shot appears to be the highest ever observed in the laboratory.

Positron research has extended over diverse fields from particle physics and astrophysics to medical application. This often requires the production of large numbers of positrons on a short time scale, which has been difficult to supply. The new OMEGA EP results could profoundly alter the direction of the quest of establishing a laser-produced positron source for research in these fields.

X-Ray Absorption Fine Structure Measurements of Iron Compressed to a Few Megabars

Principal Investigators: Y. Ping and D. G. Hicks (LLNL)

Co-investigators: J. H. Eggert (LLNL); B. Yaakobi

and T. R. Boehly (LLE); and R. Hemley (Carnegie)

X-ray absorption fine structure (XAFS) measurements were performed on iron that was ramp and multishock compressed to a pressure of a few megabars. By dynamically compressing a few-micron-thick iron sample sandwiched between thin diamond anvils, near-constant pressure conditions were produced inside the iron with the bulk of the pressure evolution taking place in the adjacent, x-ray-transparent diamond anvils. A spherical, imploding backlighter source was used to produce a smooth broadband source of x rays for the absorption measurement. Several different target configurations were studied in the single day of shots performed in FY09 to establish the optimum configuration of target versus backlighter drive and how best to achieve simultaneous measurements of the pressure using a velocity interferometer system for any reflector (VISAR). Success was achieved by maximizing the number of beams used on the backlighter and driving the target package with a stacked, multishock pulse. The resulting XAFS spectra (Fig. 120.70, compared to an undriven target) were analyzed using the FEFF code and found to give a compression of 1.55 and a temperature of 6000 K, with a pressure of 2.5 Mbar obtained from the VISAR. A modified analysis is being developed to determine the radial distribution function $g(r)$ from these data. Future work will scan through different regions of pressure, density, and temperature space to map out the iron phase diagram.

Probing H/He Warm Dense Matter with Inelastic X-Ray Scattering: Toward the Equation of State of Jupiter's Core

Principal Investigator: S. P. Regan (LLE)

Co-investigator: G. Gregori (LLNL)

The objective of this research is to measure the equation of state (n_e , T_e , Z) of direct-drive, shock-heated, planar cryogenic H/He targets using spectrally resolved x-ray scattering (i.e., inelastic x-ray scattering) in the 1- to 100-Mbar range. The H/He warm dense matter is relevant to planetary interiors. The largest planet in our solar system, Jupiter, is composed primarily of H and He, having a predicted pressure in the tens-of-megabars range. The research has a synergistic relationship with the programmatic direct-drive inertial confinement fusion (ICF) research being conducted at the Omega Facility. It works in parallel with the ICF research, which uses inelastic x-ray

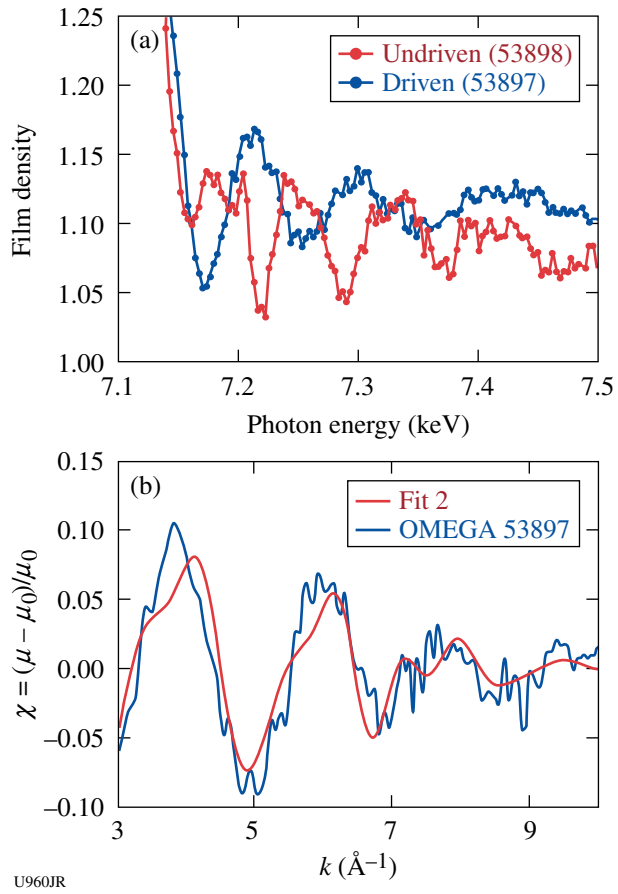


Figure 120.70

(a) Comparison of raw x-ray absorption spectra for undriven iron and multishocked iron compressed to ~ 2.5 Mbar. (b) A best fit to the x-ray absorption coefficient as a function of wave number gives a compression of 1.55 and a temperature of 6000 K.

scattering to study the equation of state (EOS) of direct-drive, shock-heated, planar cryogenic deuterium targets. In the truncated LBS shot schedule, one day on OMEGA was dedicated to demonstrating this experimental platform. A planar liquid deuterium target was chosen to maximize the likelihood of success. The polyimide ablator was irradiated with a 6-ns constant-intensity ($\sim 10^{14}$ W/cm 2) laser drive forming an ~ 100 - μm -thick layer of shocked deuterium, which is uniform in the transverse dimension over a 0.5-mm diameter. The 1-D predictions for the laser-ablation-driven shock wave are $P = 12$ Mbar, $T_e = 22$ eV, $n_e = 2 \times 10^{23}$ cm $^{-3}$, $\rho = 0.8$ g/cm 2 , and $Z = 1$. A collimated beam of Cl Ly α emission (2.96 keV) was scattered from the shocked deuterium and detected with a gated x-ray spectrometer at a scattering angle of 90°. The measured spectrum of Cl Ly α emission (2.96 keV) and He-like satellites transmitted through the shocked liquid deuterium is shown in Fig. 120.71(a). The measured spectrum of noncollective x-ray scattering for Cl Ly α emission at 90° (diamonds) is compared

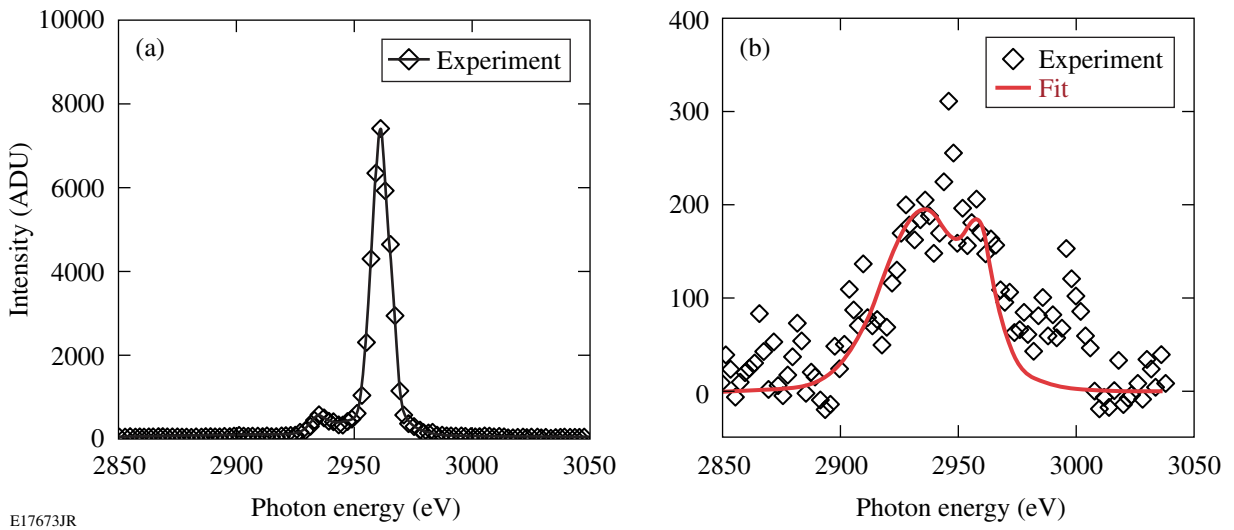


Figure 120.71

(a) Measured spectrum of Cl Ly α emission (2.96 keV) and He-like satellites transmitted through the shocked liquid deuterium; (b) measured spectrum of noncollective x-ray scattering for Cl Ly α emission at 90° (diamonds) compared with spectrum predicted for $T_e = 20$ eV, assuming $n_e = 1 \times 10^{23} \text{ cm}^{-3}$ and $Z \sim 1$.

with spectrum predicted (red curve) for $T_e = 20$ eV, assuming $n_e = 1 \times 10^{23} \text{ cm}^{-3}$ and $Z \sim 1$ in Fig. 120.71(b). The initial results are promising; however, further optimization in the experiment is needed to improve the noisy, scattered x-ray signal.

Integrated Shock-Ignition Experiments on OMEGA

Principal Investigators: W. Theobald and R. Betti (LLE)

Parametric plasma instabilities are of concern in an ignition target design with spike-pulse intensities in the range of 10^{15} to 10^{16} W/cm^2 and pulse durations of approximately sev-

eral hundred picoseconds. The instabilities degrade the laser energy coupling to the capsule and increase the fraction of the laser energy transferred to hot electrons, which is a potential source of preheat that can reduce the final core compression in functional ICF implosions.

To test the effect of laser-plasma instabilities and hot electrons, shock-ignition laser-plasma experiments have been performed on the OMEGA laser with shock-generating laser intensities of up to $\sim 8 \times 10^{15} \text{ W/cm}^2$ (Ref. 25). Figure 120.72 shows a schematic of the experiments. The compression pulse

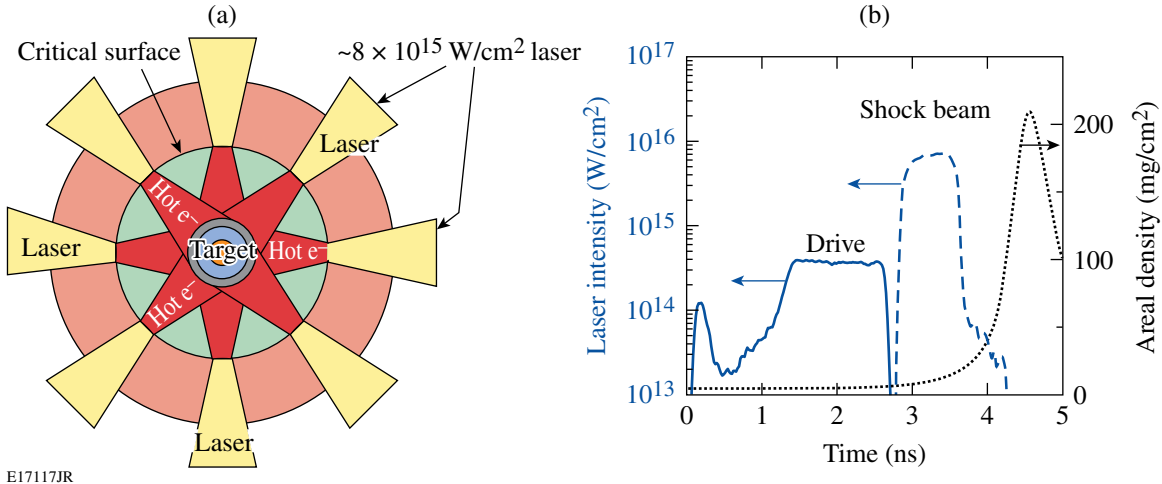


Figure 120.72

(a) Schematic of the setup for studying laser-plasma interactions and preheating at high laser intensities relevant to shock ignition. Forty of the OMEGA laser beams implode the capsule at low intensities. Twenty delayed beams are tightly focused onto the critical-density surface, where plasma instabilities lead to the generation of energetic electrons heating the dense core. (b) Pulse shapes of the 40 drive beams (solid), 20 shock beams (dashed), and areal-density evolution (dotted).

consists of a shaped low-adiabat pulse (solid) using 40 OMEGA beams with ~ 13.6 kJ of UV laser energy. The targets were 36- μm -thick, 430- μm -outer-radius, deuterated plastic shells coated outside with a 0.1- μm layer of aluminum and filled with D₂ gas with a pressure of ~ 30 atm. A late shock was driven by the remaining 20 UV beams that were delayed and tightly focused on the compressed core to achieve intensities at the critical-density surface ranging from $\sim 2 \times 10^{15}$ to $\sim 8 \times 10^{15} \text{ W/cm}^2$.

The effect of high-intensity shock beams on neutron and hard x-ray yields was studied as a function of the delay between the 40 and 20 beams [Figs. 120.73(a) and 120.73(b)]. The delay time defined by the onset of the high-intensity beam with respect to the start of the drive pulse was varied from 2.3 ns to 2.9 ns. The neutron yield increased by a factor of ~ 7 from 5×10^8 to $\sim 3.5 \times 10^9$ for the shortest time delay. Two reference implosions with only 40 drive beams produced neutron yields of 1.4×10^8 and 3.7×10^8 ; the solid line in Fig. 120.73(a) represents the average of these yields. Figure 120.73(b) shows the hard x-ray signal, which is indicative of hot-electron production. A similar trend is observed for the hard x-ray yield, showing a larger amount of hot electrons generated at shorter time delays. The measured neutron yields of the 40-beam implosion show that, despite large target-illumination nonuniformity, a significant amount of the high-intensity-pulse energy is coupled into the capsule, producing up to $\sim 20\times$ more neutrons and a strong hard x-ray signal.

Integrated Fast-Ignition Experiments

Principal Investigators: W. Theobald and C. Stoeckl (LLE)
Co-investigators: R. Betti and J. A. Delettrez (LLE); R. S. Stephen (General Atomics); and A. J. MacKinnon (LLNL)

Integrated fast-ignition (FI) experiments²⁶ began in FY09 at the Omega/Omega EP Laser Facility. The targets were 40- μm -thick empty CD shells of ~ 870 - μm outer diameter, where a hollow gold cone with a full opening angle of 34° was inserted

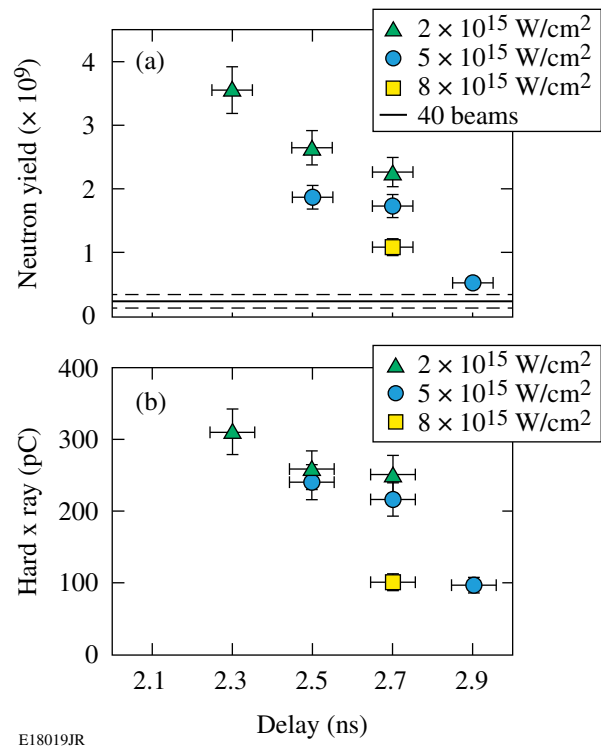


Figure 120.73

(a) Measured neutron yield and (b) hard x-ray yield versus the delay time of the high-intensity beam. The different symbols represent different focus positions with respect to the critical-density surface. The solid line in (a) is the average yield for 40-beam implosions; the dashed lines represent the error range. The 40-beam implosions produced no measurable hard x-ray signal.

through a hole in the shell (see Fig. 120.74). The cone had a sidewall thickness of 10 μm with 10- and 15- μm -thick tips. A low-adiabat laser pulse comprised of a short picket pulse and a shaped ~ 2.7 -ns drive pulse with 351-nm wavelength and ~ 18 kJ of energy imploded the capsule. The 1053-nm-wavelength short pulse was injected through the hollow cone, had an energy of 1 kJ and a duration of 10 ps, and was focused to a spot of ~ 40 - μm diameter containing 80% of the laser energy. The corresponding peak laser intensity at the center of the tip of the cone was estimated to be $\sim 6 \times 10^{18} \text{ W/cm}^2$.

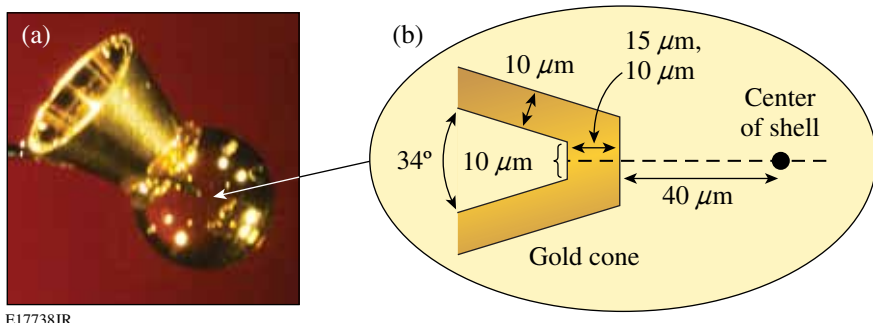


Figure 120.74

(a) Photograph of a gold re-entrant cone target;
(b) schematic showing the cone-tip dimensions.

X-ray images show a threefold increase in x-ray emission with short-pulse energy of up to 1 kJ compared with similar implosions without a short-pulse beam. The pinhole images provide only qualitative information. Yield measurements of the 2.45-MeV neutrons from D–D fusion reactions are required to obtain quantitative information on the coupling efficiency. Neutron-yield measurements were challenging because of the emission of an intense γ -ray pulse. The strong background consisted of bremsstrahlung emission generated by MeV electrons streaming through the gold cone target. The γ -ray pulse induced a fluorescence background in the neutron detectors that persisted for several hundred nanoseconds and masked the much weaker neutron signal. A new neutron detector that was developed to overcome this problem now reliably measures neutron yields in integrated FI experiments. The detector uses an organic liquid scintillator that is saturated with molecular oxygen.

Figure 120.75 shows the measured neutron yield from integrated shots obtained at various arrival times of the short-pulse laser. The solid line represents the measured yield without the short-pulse laser. The neutron yield increased more than a factor of 2 with an appropriately timed OMEGA EP beam producing up to $1.5 \pm 0.6 \times 10^7$ additional neutrons. Initial DRACO/LSP simulations were performed to study core heating in the integrated fast-ignition (FI) experiments. The calculated neutron-yield increase caused by fast-electron heating is $\sim 2 \times 10^7$ if it is assumed that $\sim 10\%$ of the short-pulse energy is converted into fast electrons. The simulations did not take radiation

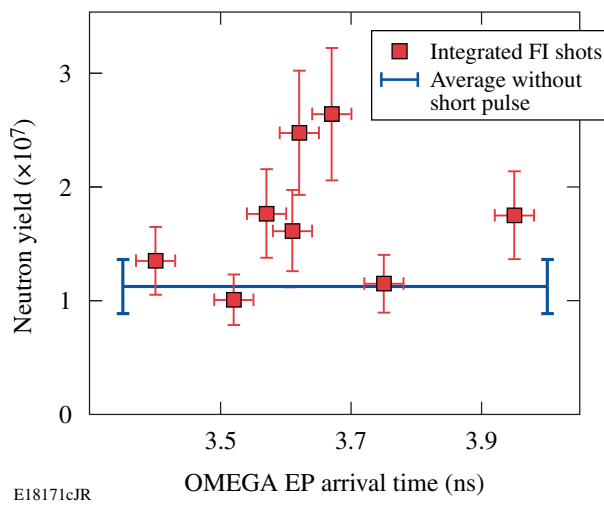


Figure 120.75
Measured D–D neutron yield from integrated fast-ignition shots (squares) versus timing of the short-pulse laser. The solid line represents the measured yield without the short-pulse laser.

transport and power balance into account, which leads to an over-prediction of density and temperature of the imploding shell. The calculated neutron-yield increase caused by the short-pulse laser is probably optimistic because the predicted higher density leads to a larger fraction of stopped fast electrons and because the gold cone material was not included in the electron-transport calculation. Fast-electron transport through the tip of the gold cone is significantly affected by the material properties and will affect the neutron yield.

FY09 LLNL OMEGA Experimental Programs

In FY09, LLNL led 238 target shots on the OMEGA Laser System. Approximately half of these shots supported the National Ignition Campaign (NIC). The remainder were dedicated to experiments for the high-energy-density stewardship experiments (HEDSE).

Objectives of the LLNL-led NIC campaigns on OMEGA included

- *Laser–plasma interaction studies in physical conditions relevant for the National Ignition Facility (NIF) ignition targets*
- *Demonstration of $T_r = 100$ -eV foot-symmetry tuning using a re-emission sphere*
- *X-ray scattering in support of conductivity measurements of solid-density Be plasmas*
- *Experiments to study the physical properties (thermal conductivity) of shocked-fusion fuels*
- *High-resolution measurements of velocity nonuniformities created by microscopic perturbations in NIF ablator materials*
- *Development of a novel Compton radiography diagnostic platform for inertial confinement fusion (ICF) experiments*
- *Precision validation of the equation of state for quartz*

The LLNL HEDSE campaigns included the following:

- *Quasi-isentropic (ICE) drive used to study material properties such as strength, equation of state, phase, and phase-transition kinetics under high pressure*
- *Development of a high-energy backlighter for radiography in support of material strength experiments using OMEGA EP and the joint OMEGA/OMEGA EP configuration*
- *Debris characterization from long-duration, point-apertured, point-projection x-ray backscatterers for NIF radiation transport experiments*

- Demonstration of ultrafast temperature and density measurements with x-ray Thomson scattering from short-pulse-laser-heated matter.
- The development of an experimental platform to study nonlocal thermodynamic equilibrium (NLTE) physics using direct-drive implosions
- Opacity studies of high-temperature plasmas under LTE conditions
- Characterization of copper (Cu) foams for HEDSE experiments

1. National Ignition Campaign

Laser–Plasma Interactions: The FY09 laser–plasma interaction experiments continued to emulate the plasma conditions expected along the laser-beam path in inertial confinement fusion designs. An interaction beam (Beam 30) aligned along the axis of a gas-filled hohlraum is used to study laser-beam propagation. This year, the effect of polarization smoothing was shown to increase laser-stimulated Brillouin scattering backscatter thresholds by about the $1.6\times$ factor expected analytically and from simulations.²⁷ Second, the sensitivity of stimulated Raman scattering to density was checked in NIC-relevant plasmas.²⁸ The results will be presented as an invited talk at the APS DPP 2009 meeting.

Symmetry Diagnosis by Re-emission Sphere: The indirect-drive NIC proposes to set the first 2 ns of hohlraum radiation symmetry by observing the instantaneous soft x-ray re-emission pattern from a high-Z sphere in place of the ignition capsule. The soft x-ray measurements require low-Z windows over diagnostic holes and the laser beams that otherwise would interact with these windows have to be turned off. To assess this technique under NIC conditions, we used the Omega

Laser Facility to image the re-emission of Bi-coated spheres placed inside a vacuum hohlraum with 200-ps temporal, 50- to 100- μm spatial, and 30% spectral resolution. The experiment is shown schematically in Fig. 120.76. Different from the previous experiments performed in scale-0.6 NIF hohlraums,²⁹ the new experiments were performed in larger scale-0.93 NIF hohlraums, making it possible to achieve a hohlraum laser-entrance-hole (LEH) size and inner laser-beam illumination, similar to upcoming NIF experiments, by azimuthally steering four inner beams away from the diagnostic window. Furthermore, compared to the experiments of Ref. 29, these experiments use a less-perturbing off-axis stalk rather than a thin CH tent to hold the capsule.

As shown in Fig. 120.77, by using 1-ns square laser pulses, we achieved hohlraum radiation temperatures measured with Dante that are similar to those calculated for future NIF experiments. The laser beams smoothed with SG4 phase plates generated intensities at the hohlraum wall that are similar to the foot of the NIF ignition design.

We acquired good re-emission images in the 0.4- to 1.3-ns time interval corresponding to 85- to 115-eV NIF foot hohlraum temperatures for both 900- and 1200-eV energy bands at several inner-to-outer beam power balances; the images are shown in Fig. 120.78. The x-ray background from the sphere stalk was negligible, validating the target design for upcoming NIF re-emit experiments. The data confirm the required measurement accuracies of $<3\%$ P_2/P_0 and P_4/P_0 Legendre mode flux asymmetry demonstrated in Ref. 29. Furthermore, the image signal-to-noise ratio is in agreement with a Planckian model for sphere re-emission, similar to Ref. 29.

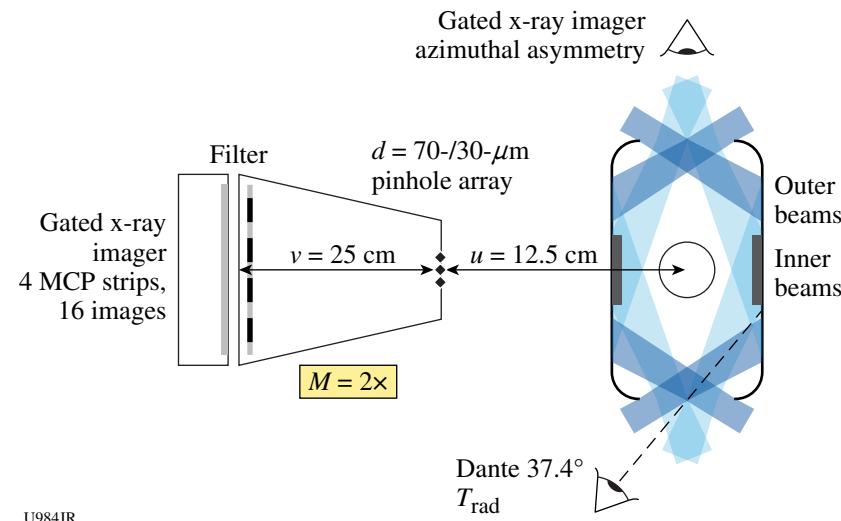


Figure 120.76
Re-emission experimental setup for the NIF and OMEGA.

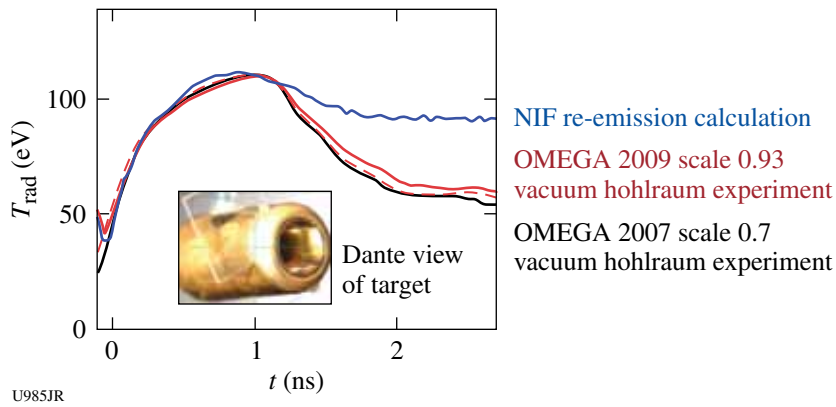
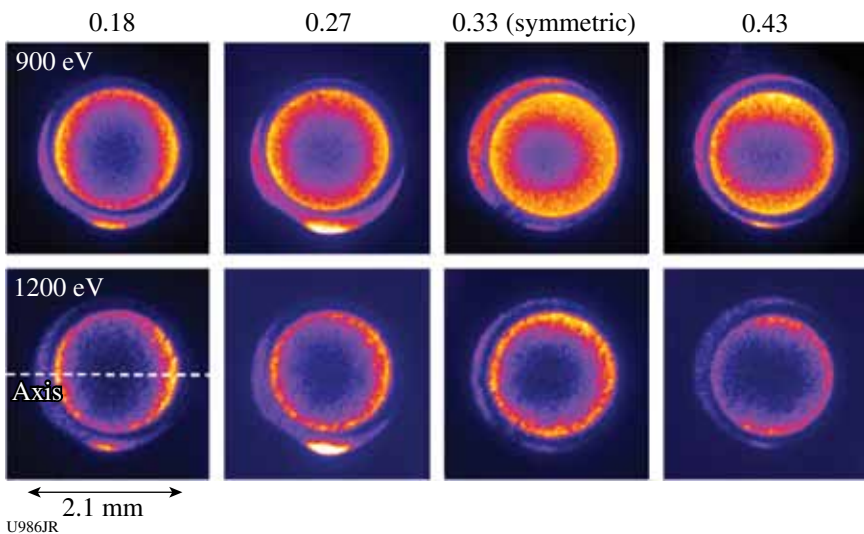


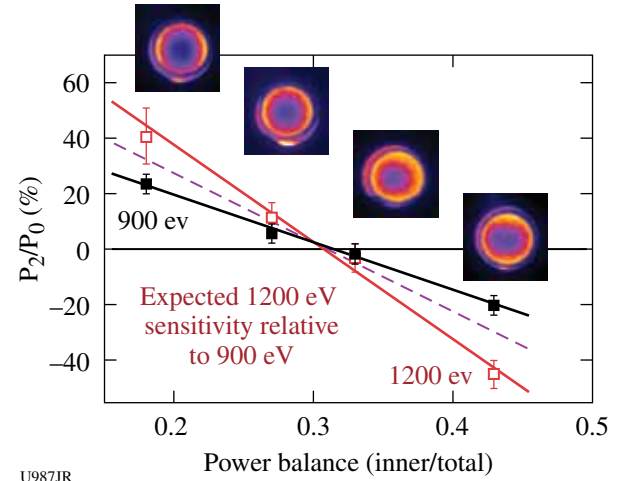
Figure 120.77
Hohlraum radiation temperatures measured with Dante in the OMEGA experiments and calculated for the NIF.



As shown in Fig. 120.78, by changing the inner-to-outer beam power balance that will be used to tune early time P_2/P_0 in NIF ignition targets, we were able to change the radiation symmetry at the capsule from pole hot to equator hot. Figure 120.79 shows the measured average P_2/P_0 as a function of power balance.

The measured P_2/P_0 sensitivity to power balance per beam is consistent with Ref. 29, where smaller hohlraums, larger LEH (75% versus 60% of the hohlraum diameter), and fewer inner beams (4 versus 8) were used. In both experiments the measured 1200-eV to 900-eV P_2/P_0 relative sensitivity of 2 is larger than the $h\nu$ ratio (1.33), which is given by an ideal Planckian model for the sphere re-emission. This difference is under investigation.

X-Ray Thomson Scattering—Conductivity of Warm, Dense Matter: The goal of these FY09 experiments was to isochorically heat a 250- μm Be foil to sufficiently high temperatures in order to observe upshifted plasmon signals with collective x-ray Thomson scattering (XRTS). Quantitatively measuring the ratio of upshifted over downshifted plasmon strength enables one to infer the electron-plasma temperature based



on first principles from the detailed balance relation, i.e., it is proportional to the Boltzmann factor $\exp(-h\nu_{\text{res}}/k_B T_e)$, with $h\nu_{\text{res}}$ the plasmon shift.

We utilized the XRTS target platform, which had been proven very successful in experiments on shock-compressed Be. For isochoric heating we employed L-shell x rays^{30,31} that were created in thin Ag, Au, or Rh foils that were directly mounted to the Be, cf. Fig. 120.80(a) for a schematic experimental setup. Time delayed to the 10 heater beams, 16 probe beams created the Cl Ly α x-ray probe at 2.96 keV. The source spectrum is plotted in Fig. 120.80(b). The x rays scattered off the rear Be surface under a 40° scattering angle were recorded by the gated Thomson spectrometer, which is based on high-opacity pyrolytic graphite as the Bragg crystal.

We obtained the best results with a silver x-ray converter foil. The scattering spectrum (black solid line), plotted in Fig. 120.80(b), shows inelastically scattered contributions that are up- and downshifted in energy compared to the Cl Ly α source line. The plasmon features are rather broad since the collectivity parameter $\alpha = 1.22$, putting the experiment just into the collective scattering regime. The best fit (red line) to the data is achieved for $T_e = 18$ eV and $n_e = 1.8 \times 10^{23} \text{ cm}^{-3}$. The temperature is determined from detailed balance with an accuracy of 20%.

D₂ Thermal Conductivity: Reflectance and thermal conductivity of deuterium increase dramatically during compression above 1 Mbar. Simultaneous measurements of velocity, reflectance, and emissivity are being used to investigate the transport properties of cryogenic D₂ compressed by multiple shocks up to 6 Mbar at 7000 K (see Fig. 120.81). In FY10 reliability improvements to the experimental platform will enable one to measure D₂ transport properties across a wide region of phase space.

Capsule Instability Seeding by Shock Nonuniformity: Two consecutive shot days were devoted to CAPSEED campaigns in FY09. The primary focus of these campaigns was to study Be ablator samples of varying quality in order to compare them with results from detailed metrology such as grazing-angle x-ray scattering, electron microscopy, and surface profile measurements. The OMEGA high-resolution velocimeter (OHRV) diagnostic was configured with higher sensitivity than previ-

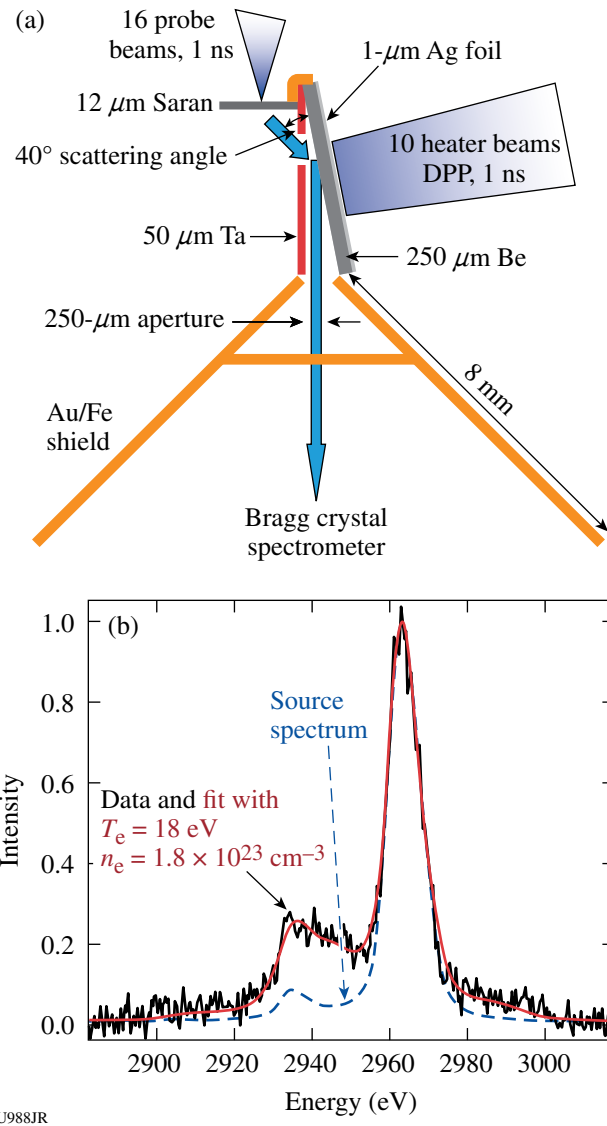


Figure 120.80

(a) Experimental setup to isochorically heat a 250-μm Be foil that is characterized with a Cl Ly α x-ray probe at 2.96 keV. Shields block the direct line of sight to the spectrometer (toward the bottom). (b) X-ray Thomson scattering data show up- and downshifted plasmon signals that make it possible to infer temperature from a detailed balance relation.

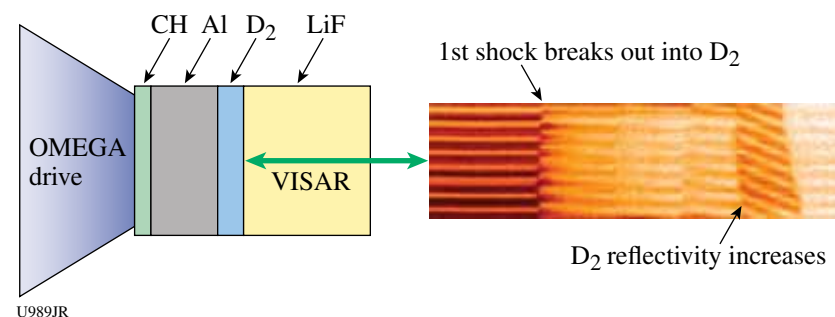


Figure 120.81

Experimental setup and VISAR record of multi-shock compressed D₂ to 6 Mbar. A dramatic increase in the D₂ reflectance can be seen in the streak record at the arrival of the final shock.

ous experiments to reduce the noise floor as low as possible. Analysis of the data led to several conclusions: (1) the velocity nonuniformities in high-quality Be samples are effectively at the noise floor of the OHRV, which meets the NIF requirement for ablator performance; and (2) poor-quality sample batches produced a higher level of nonuniformities than better-quality sample batches. The velocity nonuniformities observed in the poor-quality batches (Fig. 120.82) were attributed to the presence of a significant fraction of voids in the samples. The sample quality is batch dependent, so it is possible to identify high- and low-quality batches after fabrication. This will help to eliminate low-performing batches from the NIF experiments using electron microscopy and x-ray scattering. Future developments will focus on improving the noise floor of the instrument and continuing with high-sensitivity measurements on CH(Ge) and diamond samples.

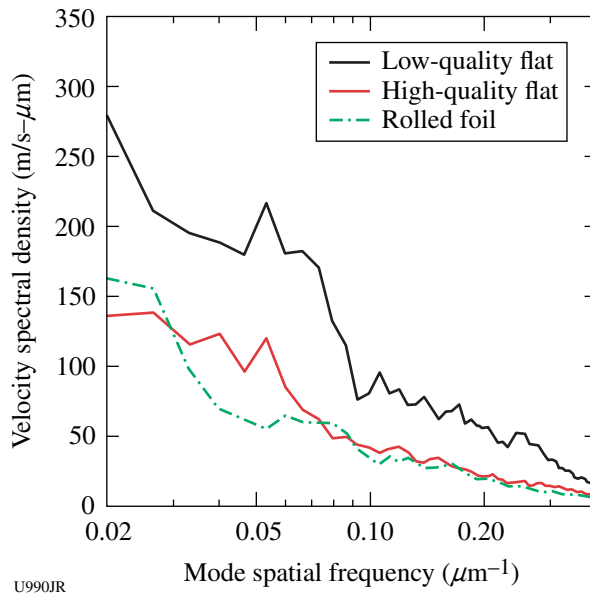


Figure 120.82
Velocity amplitude spectra recorded for three different Be sample types. The flats were Cu-doped sputtered Be foils, and the rolled foil was a polished sample of commercially available Be foil.

Compton Radiography: The goal of the Compton radiography campaign is to build a novel diagnostic platform for ICF. In FY09 we successfully obtained the first-ever radiographs of implosions, at photon energies around and above 60 keV, where Compton scattering largely dominated the opacity of the plastic shell. In our experiments we used 60 beams of the OMEGA laser for direct-drive implosions of 40- μm -thick, 870- μm -diam CH capsules filled with 3 atm of DD gas, located at OMEGA's target chamber center. As a backscatterer we used a 10- μm -diam Au wire, 300 μm long, in a point-projection,

end-on geometry 10 mm from the CH shell. The backscatterer was driven by the OMEGA EP short-pulse beam, delivering ~1 kJ at 10 ps in a 100- μm -square spot size. The time delay between the OMEGA EP short pulse and the OMEGA laser pulses was chosen to match the time of peak compression predicted by LILAC 1-D simulations. To record the radiographs, we designed and built a dedicated Compton radiography snout (CRS) consisting of a three-stage collimator, a layered structure of Al-Pb to shield against neutrons and high-energy x and γ rays, and a permanent magnetic field to deflect electrons away from the radiography line of sight. CRS allows for the insertion of filters at different locations and hosts a Fujifilm BAS imaging plate detector at about 400 mm from target chamber center. By progressively increasing filtration in the CRS, we obtained good-quality radiographs (with a signal-to-noise ratio of a few at 2% contrast) at (average) photon energies of approximately 60 keV, 80 keV, and 100 keV. As an example, Fig. 120.83 shows a radiograph of the imploding CH shell, near peak compression, at $t = 4$ ns, obtained at a photon energy of ~60 keV. The

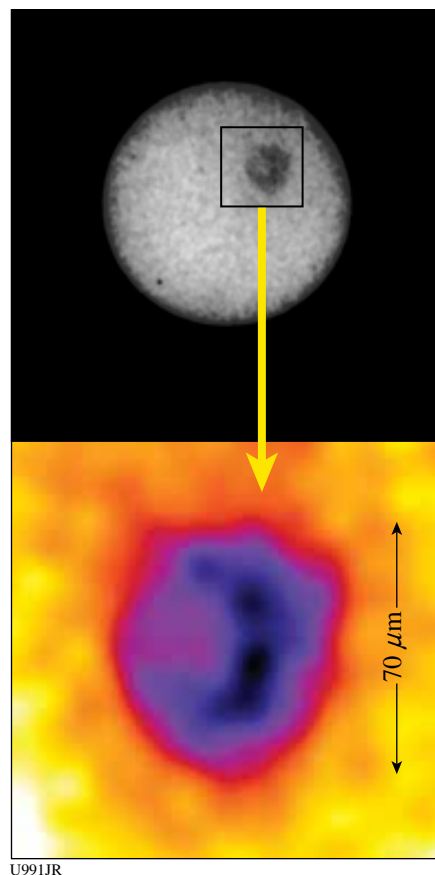


Figure 120.83
Compton radiograph of CH shell near peak compression: $\langle h\nu \rangle \sim 60$ keV.
(a) CH shell radiograph inside the shadow of a CRS collimator; (b) blowup of radiograph.

diameter measured from the radiograph was $70\text{ }\mu\text{m}$: very close to the value of $60\text{ }\mu\text{m}$ predicted by LILAC 1-D simulations. The CRS features a built-in step wedge filter that allows one to reconstruct the backlighting Bremsstrahlung spectrum and therefore measure the density from the radiograph.

Precision Validation of Quartz Equation of State (EOS): CH_n EOS measurements performed earlier in the year relied on quartz as the impedance-matching standard. The quartz (SiO₂) Hugoniot, measured several years ago on OMEGA, was found to be in good agreement with a linear shock velocity to particle velocity relation [see Fig. 120.84(a)]. This fit was also in agreement with earlier Russian measurements up to 6 Mbar and a single 20-Mbar point. However, given the sensitivity of impedance-matching measurements to uncertainties in the impedance-matching standard, it was necessary to further increase our confidence in the quartz Hugoniot. This was done by using a new “bootstrap” impedance-matching method, whereby quartz ($\rho_0 = 2.65\text{ g/cc}$) is impedance matched to another polymorph of SiO₂ fused silica ($\rho_0 = 2.2\text{ g/cc}$) [see Fig. 120.84(b)]. Since each Hugoniot probes a slightly different region of the SiO₂ high-pressure phase diagram, the results are highly sensitive to derivative quantities, in particular the slope of the $U_s - U_p$ relation and the Gruneisen parameter.

2. High-Energy-Density Stewardship Experiments

Material Properties: In FY09 five experiment campaigns on OMEGA and OMEGA EP were performed in support of the material dynamics effort: thin-walled hohlraum drive development (1/2 day each, two campaigns); low-density foam reservoir

tests (1/2 day); tantalum Rayleigh–Taylor experiment using OMEGA plus OMEGA EP in a joint experiment day; and high-energy backlighter characterization (one OMEGA EP day).

Quasi-Isentropic Compression Hohlraum Drive Development: The main goal of the first half-day of OMEGA shots was to test the thin-walled hohlraum’s performance to decrease the late-time radiation temperature (Tr) to delay and reduce the strength of the late-time shock in the quasi-isentropic pressure drive platform. The thin-walled hohlraums had a 1- μm Au wall with 100- μm -thick epoxy backing. In this experiment the ablator was 75 μm of CH, to make a direct comparison with thick-walled hohlraum data from previous shots in March 2008. Our data suggest that the thin-walled hohlraums do delay the arrival of the late-time shock, so we will be able to utilize this platform for our strength experiment. The other goal for this campaign was to test low-density foams as the final layer in our reservoir. We tested 50-mg/cc SiO₂ aerogel (100 and 200 μm thick) and 100-mg/cc carbonized resorcinol formaldehyde (CRF) (50- μm -thick) foams. The ablator was 25 μm of Be. Comparison between the data and the simulations showed that these low-density foams worked well and showed no hydro-instabilities. The simulations of the velocity interferometry system for any reflector (VISAR) data show abrupt velocity steps for each reservoir layer, corresponding to the foam followed by the CH (12.5% Br) layer. The data also showed distinct velocity steps for each reservoir layer, but the transition between layers was smoother than the simulated results, likely because of hydrodynamic mixing at the interface. Both simulations and data showed a late-time stagnation shock.

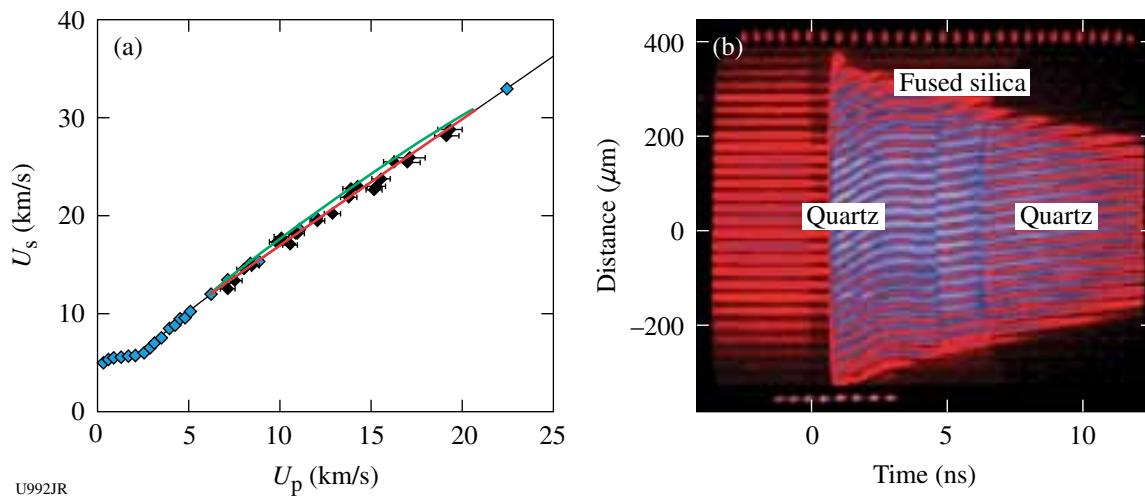


Figure 120.84

(a) Previously measured quartz Hugoniot. The red line provides the best linear fit to data; the green line provides a possible outlier fit to the data. New measurements were designed to determine possible deviations from the original linear fit. (b) Impedance matching of a quartz/fused silica/quartz target.

The goal of the second half-day of OMEGA shots was to test the thin-walled hohlraum drive using both Al and Ta witness samples to verify that they give consistent drive measurements. These two witness plate samples gave consistent results. The second goal of this half-day was to test the stacked CRF foam reservoir properties: 50 μm of 500-mg/cc CRF followed by 100 μm of 50-mg/cc CRF. We used 25- μm Be ablators for all shots during this half-day. This reservoir scales to a NIF design that reaches 5 Mb in a Ta-strength experiment. Post-shot simulations match well with the measured drive using the stacked foam reservoir. The simulated VISAR results predicted abrupt velocity steps, corresponding to each layer in the reservoir. The data, however, showed much smoother transitions between the different layers in the reservoir, likely because of hydrodynamic mixing between the layers. Provided this mixing is reproducible, this added smoothing improves the drive by minimizing shock heating.

ICE Gradient-Density Reservoir Development: The goal of this half-day of OMEGA shots was to test the foam reservoir performance for the material strength experiment. Therefore we used thick-walled hohlraums for this experiment (since the foam in the reservoir modifies only the early-time drive). We tested the low-density, 50-mg/cc SiO_2 foams by measuring the shock-breakout (SBO) times from 75/100/125 μm of SiO_2 foam thicknesses. The data matched the predictions. The second part of the experiment was to test stacked foam layers in the reservoir of 500-mg/cc CRF (50 μm thick) and 50-mg/cc SiO_2 (100 μm thick). The release profile and the SBO's on various material layers were compared to simulations, with poor agreement between the detailed interface arrival times and shape. This could be due to uncertainties in the EOS of the SiO_2 foam.

ICE Tantalum Rayleigh–Taylor Experiments: We have successfully performed the first OMEGA and OMEGA EP joint shots (60-beam long-pulse laser plus OMEGA EP short-pulse laser combined) to measure Ta Rayleigh–Taylor (RT) ripple growth to test models of Ta material strength at \sim 1-Mbar pressures and high strain rates of \sim 10⁷ s⁻¹. The OMEGA EP laser was used to generate a high-energy backlighter (>20 keV) with high spatial resolution (<10 μm) to probe a 50- μm -thick Ta sample with 3- μm peak-to-valley sinusoidal ripples. We had four joint shots to measure the Ta RT growth, interleaved with six OMEGA-only (long-pulse) shots to measure the hohlraum drive. The joint-shot radiography technique worked well. For a few of the joints shots, the OMEGA EP beam slightly missed the 100- μm -diam micro-flat backlighter target, producing low-signal images. The growth-factor measurements require a good understanding of the backlight spectrum. Figure 120.85

shows the experimental configuration, Fig. 120.86 shows the target details, and Fig. 120.87 shows a resulting Ta RT radiography image using the high-energy Ag backlighter. Future

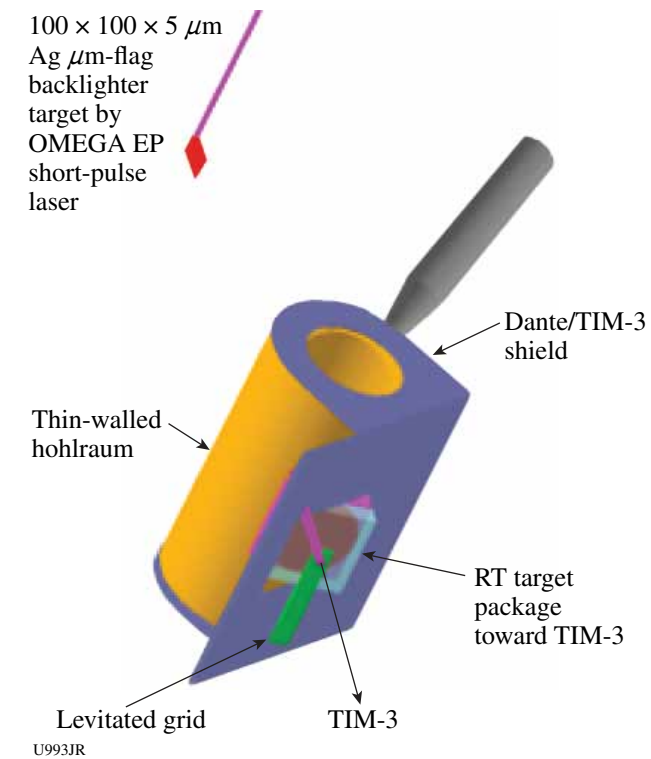


Figure 120.85
ICE tantalum Rayleigh–Taylor (ICE Ta RT)-09A experimental setup.

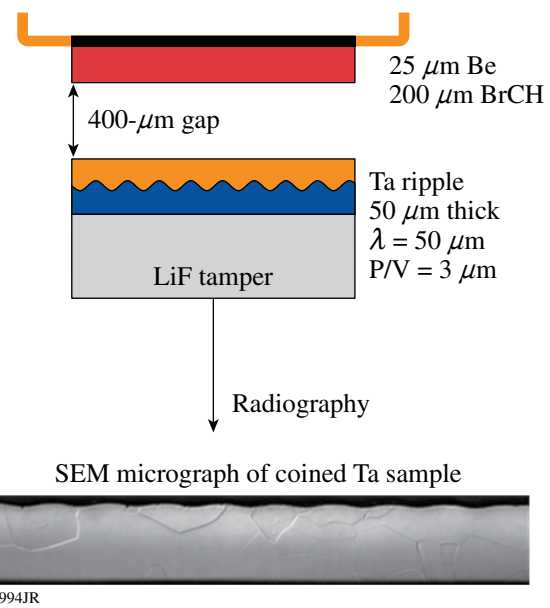


Figure 120.86
ICE tantalum Rayleigh–Taylor (ICE Ta RT) target details.

experiments will acquire data that will allow us to compare predictions of Ta strength using standard material models (PTW, Steinberg–Guinan) at \sim Mbar pressure. In conclusion, we have demonstrated that Rayleigh–Taylor experiments for Ta (and other high-Z) samples are possible, and this type of experiment opens up a new capability for high-photon-energy radiography on OMEGA experiments. This experiment also led to three invited talks: IFSA 09 (The Sixth International Conference on Inertial Fusion Science and Applications, San Francisco, CA, September 2009); APS/DPP (American Physical Society, Atlanta, GA, November 2009); and JOWG-37 (Livermore, CA, October 2009).

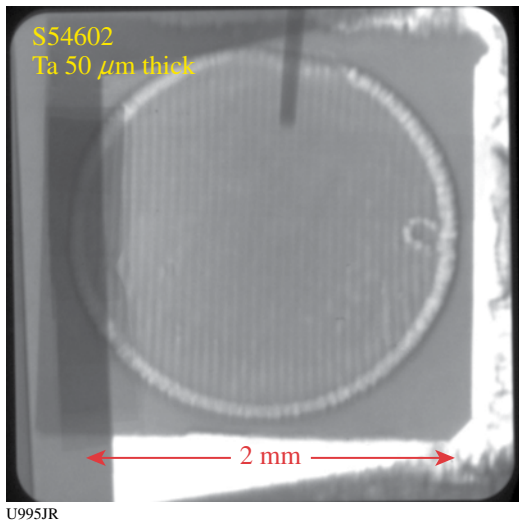


Figure 120.87
ICE Ta RT radiography using OMEGA + OMEGA EP joint shot.

High-Energy Backlighter (HEBL) Development: The goal of the HEBL OMEGA EP campaign was to measure the high-energy backlighter spectrum that would be utilized for the Ta Rayleigh–Taylor strength experiment on the NIF. The high-energy backlighter is created by the OMEGA EP short-pulse beam illuminating a micro-flag target. The absolute spectrum will be crucial to the quantitative analysis of results from the radio-graphy data. We utilized a transmission crystal spectrometer (TCS) that covers a 15- to 70-keV range; a Bremsstrahlung x-ray spectrometer that covers 70 keV to 1 MeV; and Ross-pair filters to get an absolute yield in the 20- to 70-keV range. We had six shots total and our settings were changed to test backlighter repeatability, laser spot-size dependency, and radiography object dependency. By combining detectors that span different energy ranges we were able to produce a composite spectrum from 15 keV to 1 MeV, as shown in Fig. 120.88.

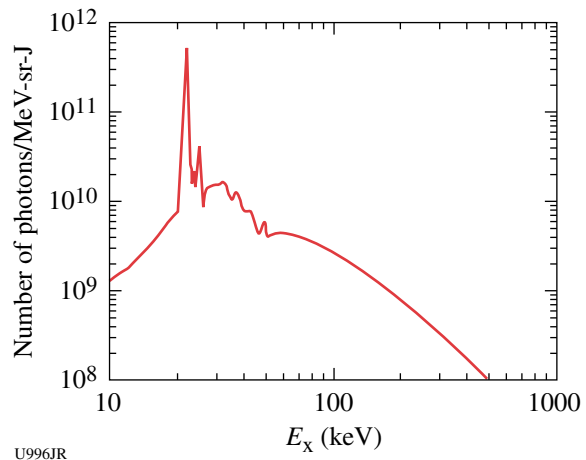


Figure 120.88
High-energy backlighter spectrum using the OMEGA EP short-pulse laser. Measurements were made using many different detectors.

Debris Characterization from Long-Duration Point-Source Backlighters: An 8-ns point-source backlighter developed on OMEGA was demonstrated on the NIF for streaked radiography. This configuration provided sufficient photons, high spatial resolution (\sim 20 μ m), and instrument protection from debris. To extend this to multiframe 2-D radiography, experiments were performed on OMEGA to characterize the debris and signal level. Pinhole-apertured point-projection backscatterers generally produce either solid or liquid ballistic spall from the pinhole substrate, which generally is accelerated normal to the pinhole surface. On experiments where using a tilted pinhole substrate is undesirable, diagnostics must be protected from spall launched directly at the x-ray detector. This is traditionally done with thick pieces of beryllium that can offer protection without sacrificing x-ray transmission.

Alternate materials are being developed for debris mitigation for pinhole-apertured point-projection backscatterers that are pointed directly at imaging diagnostics. We tested several thicknesses of aluminum and boron carbide (B_4C) for debris mitigation. Twenty OMEGA beams (10-kJ laser energy) drove a Ni pinhole-apertured point-projection backlighter (75- μ m-thick Ta pinhole substrate) from P6 toward up to six 75- μ m-thick or up to three 150- μ m-thick filters. These filters were spaced at least 15 mm apart in the MSpec snout in TIM-6, with an image plate in the static pinhole camera array detector. We found (see Fig. 120.89) that three 150- μ m-thick B_4C filters encapsulated in 8- μ m Kapton let debris penetrate the rear-most filter once or twice, whereas three 75- μ m-thick Al filters or two

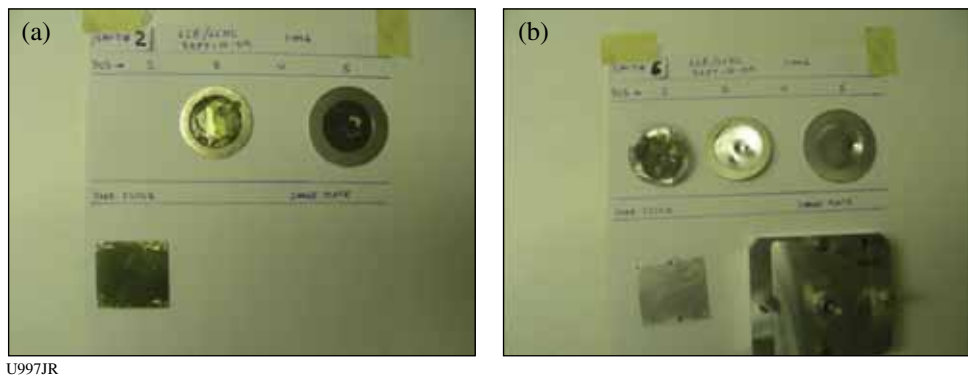


Figure 120.89

Damaged filters from debris testing. (a) Three 150- μm -thick B₄C-Kapton filters, showing one pinhole in the rear filter; (b) four 75- μm -thick Al filters, with the first three showing some ballistic damage, and a clean rear filter.

150- μm -thick Al filters stopped all the ballistic debris, leaving at least one clean rear filter. This suggests that the debris can be mitigated while allowing sufficient x-ray transmission.

X-Ray Thomson Scattering: The objective of this campaign was to demonstrate ultrafast temperature and density measurements with x-ray Thomson scattering from short-pulse-laser-heated matter. In March 2009, we used OMEGA EP to heat a 200- μm beryllium cube with a 1-kJ, 10-ps short-pulse laser beam and performed the first noncollective x-ray scattering measurements using a Zn K _{α} x-ray probe at 8.62 keV (see Fig. 120.90). The probing x rays were produced by the second

OMEGA EP 10-ps short-pulse laser beam. On the first day of shots, we performed a total of four shots including the very first shots with two short-pulse beams fired simultaneously for target physics experiments. In addition, we successfully fielded the new Zink von Hamos high-efficiency x-ray spectrometer, a dedicated diagnostic developed for the K _{α} x-ray Thomson-scattering project. This instrument has shown elastic and inelastic scattering signals of beryllium with only 180 J in the probe beam.

Since these experiments were the first to use both OMEGA EP short-pulse laser beams simultaneously on target, we had to field

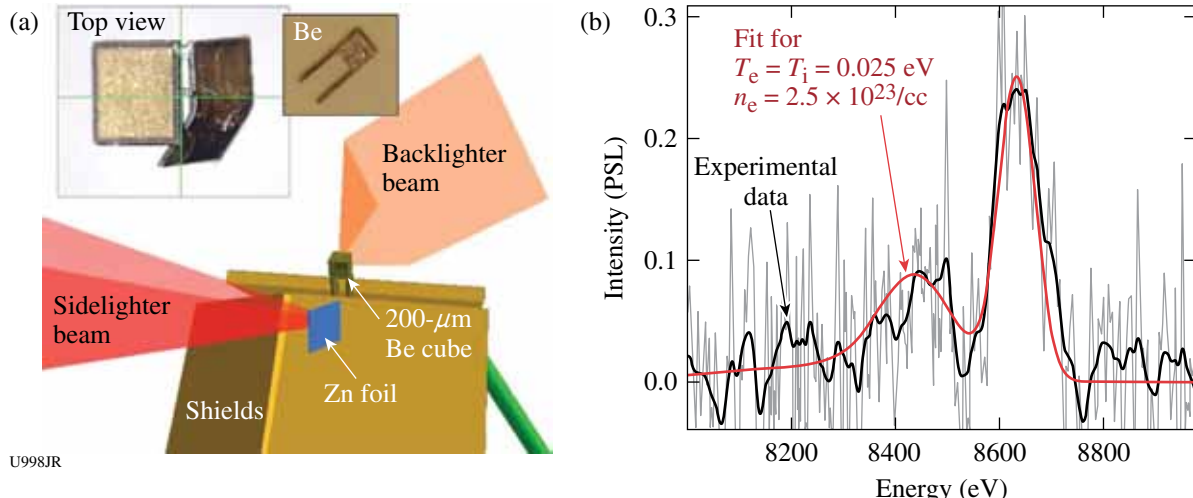


Figure 120.90

(a) Experimental setup showing the OMEGA EP backlighter beam heating a 200- μm Be cube. The OMEGA EP sidelighter beam creates a Zn K _{α} x-ray probe at 8.62 keV. Shields block the direct line of sight to the spectrometer (toward the bottom). (b) X-ray Thomson-scattering spectrum from cold beryllium, measured with only 180 J in OMEGA EP sidelighter beam. The downshifted inelastically scattered Compton feature is fitted with the parameters for cold, solid beryllium.

dedicated diagnostics to measure beam synchronization. We achieved synchronization to an accuracy of only 250 ± 200 ps, which must be improved in the future to reach ~ 100 ps for this experiment. We also employed low-energy activation shots (50 J) to successfully record the x-ray source spectrum and to determine the spectrometer dispersion. The third shot of the day delivered ~ 1 kJ within a 10-ps pulse in the *backlighter* beam to heat the Be and ~ 1.3 kJ in the *sidelighter* beam to create the x-ray probe. Since the sidelighter shot was higher in energy than originally anticipated, we reduced the energy to 180 J on the last shot of the day. Nevertheless, we were able to record elastic- and inelastic-scattering signals of cold beryllium. This is a very promising result. We also assessed the bremsstrahlung level and background levels. These measurements will enable us to improve the experimental design to measure plasma temperatures of short-pulse-laser-heated beryllium with high temporal resolution using K_{α} x-ray Thomson scattering on future shots.

Non-LTE Implosions: The goal of the non-LTE campaign is to build a platform to study the energy balance in implosions by measuring ion, electron, and radiation temperatures as a function of high-Z dopant concentration. In our FY09 experiments, we used 60 beams of the OMEGA laser for direct-drive implosions of thin ($4\text{-}\mu\text{m}$) glass capsules filled with 10 atm of D^3He gas and Kr gas as a spectroscopic tracer. The relative concentration of DD and 3He was varied during the shots, the Kr concentrations were 0.001 and 0.005 atm, and some capsules also contained as much as ~ 0.1 atm of Xe. As a time-resolved electron temperature (T_e) diagnostic, we fielded a mica conical crystal spectrometer that was coupled to a streak camera and viewed K-shell emission lines from the Kr dopant. Time-integrated spectra were also recorded with the HENEX spectrometer. We also fielded a high-resolution spectrometer to use the Doppler broadening of x-ray lines for measuring the ion temperature T_i .

We observed a decrease in the DD/DT yield ratio with increasing Xe concentration. This trend is well reproduced by LASNEX/DCA:T simulations. We observed an increase in the DD/DT yield ratio with increasing DD concentration as well as an increase in the ion temperature, inferred from proton and neutron emission time histories and spectra. Increasing Xe dopant concentration appears to reduce compression-phase T_i by coupling to radiative cooling.

We inferred the time-integrated electron temperature T_e from a Bremsstrahlung functional form fit to the continuum part of the spectra recorded by HENEX. As reported in Fig. 120.91, T_e shows a linear decrease with an increase in Xe

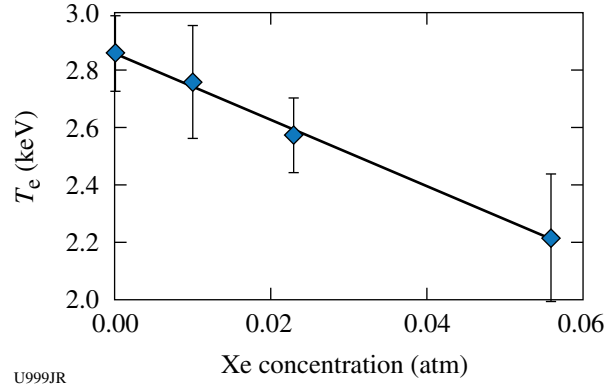


Figure 120.91

Time-integrated T_e , inferred from HENEX spectra, shows a linear decrease with an increase in Xe-dopant concentration.

dopant concentration: a behavior reproduced by simulations, although experimental measurements give values higher by a factor of about 30%.

We used the time-resolved spectra from the conical crystal spectrometer to study the temporal evolution of the Kr He_{β} lines. The $He_{\beta_2}/He_{\beta_1}$ line ratio shows a peak in the central 50 ps of the Kr emission as well as a decrease with increasing Xe concentration, as shown in Fig. 120.92.

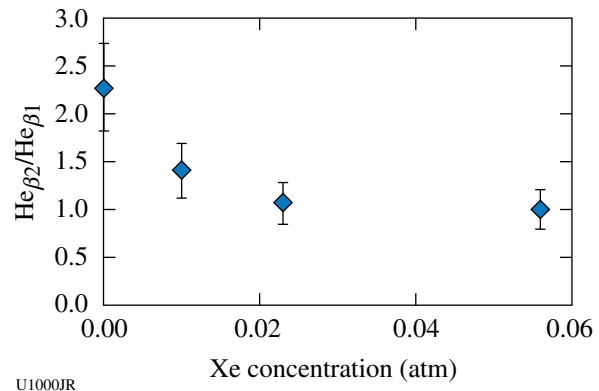


Figure 120.92

The $He_{\beta_2}/He_{\beta_1}$ line ratio, measured from conical crystal spectra, shows a decrease with increasing Xe concentration.

High-Temperature Plasma Opacity: In FY08 LLNL completed the development of a high-temperature laser opacity platform. In FY09, detailed x-ray transmission spectra from fully characterized, high-temperature plasmas were produced using the OMEGA laser to provide validation benchmarks for the x-ray opacity codes (and associated data tables) underlying

simulations of radiation transport experiments. Shots in FY09 produced detailed benchmark data on tantalum–titanium and sodium chloride–titanium plasmas. In these experiments, 24 beams heated a 1.6-mm-diam hohlraum, which in turn radiatively heated and expanded a tamped Ti foil. Additional beams drove two broadband backscatterers: a rear-wall burnthrough halfraum (14 beams) and a Kr-filled “dynamic hohlraum” capsule implosion (10 beams). Looking through the sample to these backscatterers, two broadband spectrometers characterized the sample transmission from 250 eV to 1600 eV and 3000 eV to 5500 eV, respectively; the lower energy band encompassed the bulk of the Rosseland mean opacity. The plasma density of 0.05 ± 0.01 g/cc, measured by expansion radiography, agreed well with pre-shot calculations. The plasma temperature implied by the titanium ionization features in the 3000- to 5500-eV spectra was 110 ± 5 eV (Fig. 120.93). Rosseland mean opacity data from 250 to 1600 eV is now being analyzed. Discrepancies with theory have been observed and are undergoing detailed investigation. For the future, an extension of these techniques to the NIF would enable us to investigate much hotter plasmas at conditions relevant to stellar core modeling, where recent observational data (helioseismology) contradict standard solar models. A small change in the technique will also enable us to perform a scaled experiment to study photoionized plasmas relevant to black hole accretion disk physics.

Characterization of Cu Foams: Two half-days of OMEGA shots (a total of eight) were used in support of characterization of Cu foams for HEDSE experiments. Material characteristics of interest included both the internal energy (EOS) and the opacity of the foams, at several Mbar of pressure. Pure metal foams are of use as backscatterer sources, as low-density materials for radiation–hydrodynamic experiments and opacity experiments. The first set of shots used a hohlraum to drive a CH ablator paired with a Cu foam (density about 0.89 g/cm 3) and a SiO $_2$ payload (density 0.05 g/cc). The purpose of this experiment was to measure, on the same shot, shock breakout from the Cu into the (transparent) SiO $_2$, shock velocity in the SiO $_2$, and the position of the Cu/SiO $_2$ interface by point-projection radiography. The results are sensitive to the EOS of the Cu foam but not to the opacity. Post-shot simulations agreed with the experimental results. A typical radiograph from this series is shown in Fig. 120.94(a).

The second round of shots continued characterization of Cu foam by using the Cu as an ablator in a hohlraum-driven experiment. The Cu ablator for a typical target is shown during the machining process [Fig. 120.94(b)]; the Cu foam density was about 0.89 g/cm 3 . The shock-breakout time and the foil burnthrough time are sensitive to the opacity as well as the internal energy of the foam. The post-shot simulations were again consistent with the experimental results. These results

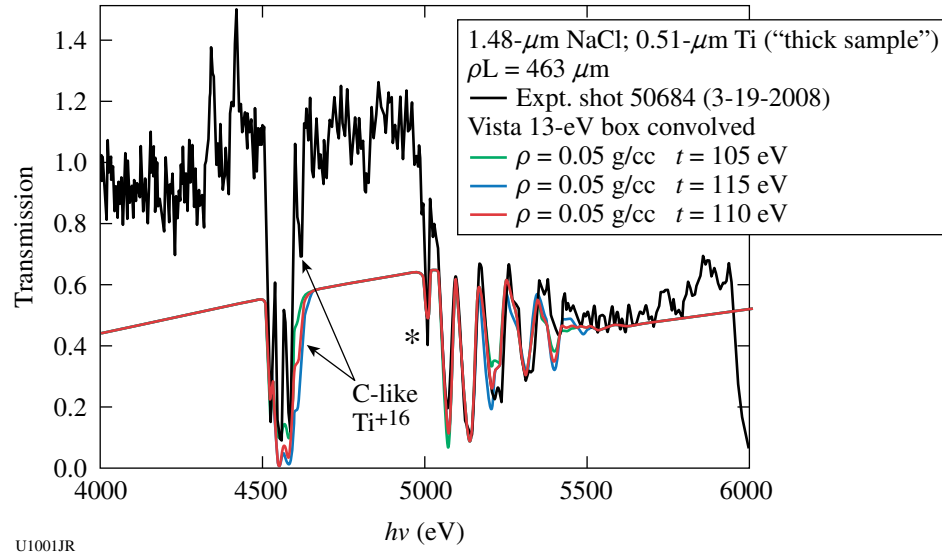


Figure 120.93

X-ray transmission opacity data from gated space-resolved titanium absorption spectra for photon energies from 4 keV to 5.9 keV. To the left are $n = 1$ to 2 absorption lines of F-like to C-like Ti, with the C-like feature being strongly temperature dependent. To the right are $n = 1$ to 3 lines of the same ions, plus a narrow feature from the Ne-like ion (*). Analysis using the VISTA opacity model indicates a temperature of 110 ± 5 eV for densities in measured range, 0.050 ± 0.010 g/cc.

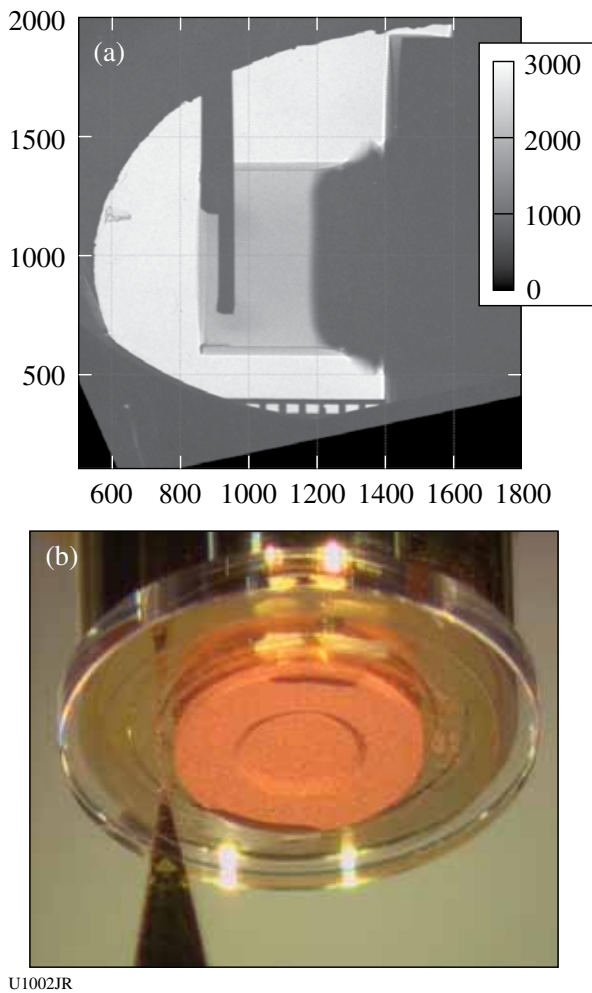


Figure 120.94

(a) A typical radiograph taken during a shock-breakout experiment; (b) a picture of one of the copper foam ablator targets.

will allow us to proceed in FY10 with designing experiments using this Cu foam.

This work performed under the auspices of the U.S. Department of Energy by Lawrence Livermore National Laboratory under Contract DE-AC52-07NA27344.

FY09 LANL OMEGA Experimental Programs

Los Alamos National Laboratory (LANL) successfully fielded a range of experiments on the OMEGA laser during FY09 in support of the national program. LANL conducted a total of 104 target shots: 93 on OMEGA and 11 on OMEGA EP. Collaborations with LLNL, LLE, LULI, NRL, MIT, NSTec, UCSD, and AWE remain an important component of LANL's program on OMEGA.

NIF-5: The NIF-5 campaign had many successes during the course of FY09. The NIF-5 spectrometer, a high-resolution x-ray spectrometer, was qualified for use on OMEGA. Preliminary analysis of the spectra indicates the spectrometer is performing as expected.

In June 2009, the NIF-5 campaign conducted experiments to study hydrodynamic features caused by a radiation drive. The target (Fig. 120.95) consisted of a gold hohlraum. Connected to the hohlraum was a gold tube and a Be tube. A plastic (CH) foam filled the Be tube and the Au tube and extended into the hohlraum. The hohlraum (1200- μm outer diameter) was heated on each end by 15 lasers beams using a 1-ns square pulse. The x rays created by this interaction then heated the CH foam. A Sc backscatterer [Fig. 120.95(b)] was illuminated with laser beams to create x rays to diagnose the foam in the Be tube.

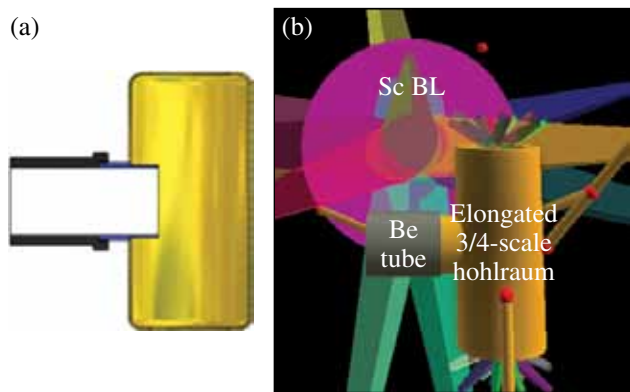


Figure 120.95

(a) A schematic of the target showing the placement of the foam in the Be tube, the Au tube, and the hohlraum; (b) a Visrad model showing the backscatterer and the target.

Two of the radiographic images obtained are shown in Fig. 120.96. The top half of the figure shows a radiograph of a radiatively induced shock in a 120- mg/cm^3 foam, 5.9 ns after the hohlraum drive lasers were fired. The bottom half shows a radiograph of a radiatively induced shock in 104- mg/cm^3 foam, 4.7 ns after the hohlraum drive beams were fired. The results of these experiments are being analyzed and will be used to help improve our future simulations.

High-Z: The purpose of the high-Z project is to investigate the effect of high-Z dopants on D_2 fusion burn. This is an ongoing project in which we have obtained a large data set showing that dopant gases such as ${}^3\text{He}$, Ar, Kr, and Xe degrade the yield in an inertial confinement fusion (ICF) implosion. This

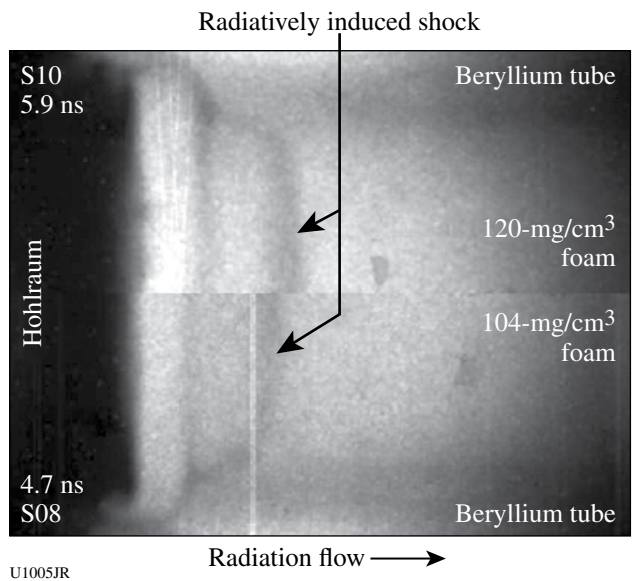


Figure 120.96

The top half of the figure shows a radiograph of a radiatively induced shock in a 120-mg/cm³ foam, 5.9 ns after the hohlraum drive beams were fired. The bottom half shows a radiograph of a radiatively induced shock in 104-mg/cm³ foam, 4.7 ns after the hohlraum drive beams.

degradation is more than calculated by our codes and occurs mostly during the latter compression stages of the implosion, after the initial shock reflects off the axis and hits the capsule shell. The reason for the degradation is unknown but understanding this degradation was the focus of FY09 activities.

The high-Z project successfully completed two full days of experiments on OMEGA in FY09. The first day of experiments focused on testing whether the OMEGA EP laser could be used as an x-ray backlighter for obtaining radiographs of imploded glass capsules. The capsule, a 4.3-mm-thick, 925- μm -diam SiO₂ capsule filled with 8.75 atm of deuterium and 0.1 atm of argon, was driven by a 0.6-ns-long pulse with a maximum energy of 239 J/beam and also by a distributed polarization rotator, an SG-4 phase plate, and full smoothing by spectral dispersion. The reason for radiographing the shell at late times is to determine if our simulation codes are correctly predicting the amount of ablation from the shell and the properties of the glass during the implosion. The backlighter was a 15- μm -thick iron foil illuminated by an OMEGA EP beam with a pulse length of about 10 ps and an irradiance of less than $5 \times 10^{15} \text{ W/cm}^2$. We obtained nine shots on this shot day, five of which included the OMEGA EP laser. We were able to obtain good data on nearly every shot, although we determined that the x-ray intensity of the 6.7-keV Fe backlighter was not as bright as the implosion

at the times of interest, as demonstrated in the results shown in Fig. 120.97. The spectral radiance of the backlighter, with a measured energy conversion efficiency of about 3×10^{-5} , was found to be weaker than the emission from the implosion by a factor of 8 (Fig. 120.98). The second day focused on testing a new experimental platform using Fe-doped glass shells. The doped shells were used to provide a source of Fe ions in the gas, which could then emit x rays that can be measured by an MMI (multiframe monochromatic imager) diagnostic. The MMI is useful in obtaining spatial profiles of temperature and density in the gas (something we do not presently measure) and would provide important information for understanding the yield degradation. On this day we were again quite successful in obtaining good data for a total of 12 shots. We used glass capsules that had 0%, 0.3%, or 0.9% Fe in the glass. We were able to measure the emission of the Fe lines but determined that the emission levels were too weak at these dopant levels to ensure successful application of the MMI diagnostic. We are pursuing plans to develop glass shells that have a higher concentration of Fe, but there are important target fabrication issues that remain to be addressed.

OMEGA EP Ions Campaign: LANL led a series of ion-generation experiments (26 March and 17 August) on OMEGA EP performed by experimental Principal Investigator (PI) K. Flippo with diagnostic PI's J. Cobble (TPIE) and D. Offermann (LANL PFPII-mod and THVL). These experiments were carried out in collaboration with UCSD, LLNL, and LLE/UR under the project leadership of LANL's M. Schmitt.

In the first series of shots (26 March), we had a total of seven shots on target that provided good data on the performance of OMEGA EP in terms of ion energies from dielectric targets [chemical vapor deposition (CVD) diamond] and conductors (Cu) using the PFPII loaded with Radiochromic film as the primary diagnostic. Figure 120.99 compares the beam quality and spectrum from (a) copper and (b) CVD diamond targets at 15- μm thicknesses. The beam profile from the 15- μm target had a well-defined outer edge of the proton beam and a higher temperature to the beam, 5.58 keV versus the beam from the copper target, which had a large defuse beam, and an inner darker beam, with a characteristic temperature of 3.79 keV. Overall the beam from the copper target contained more protons in the 4- to 36-MeV range, but fewer total ions in the higher end of the spectrum, 15 MeV to 36 MeV. Approximately 2.04% and 1.81% of the laser energy was converted into protons for CVD and copper, respectively.

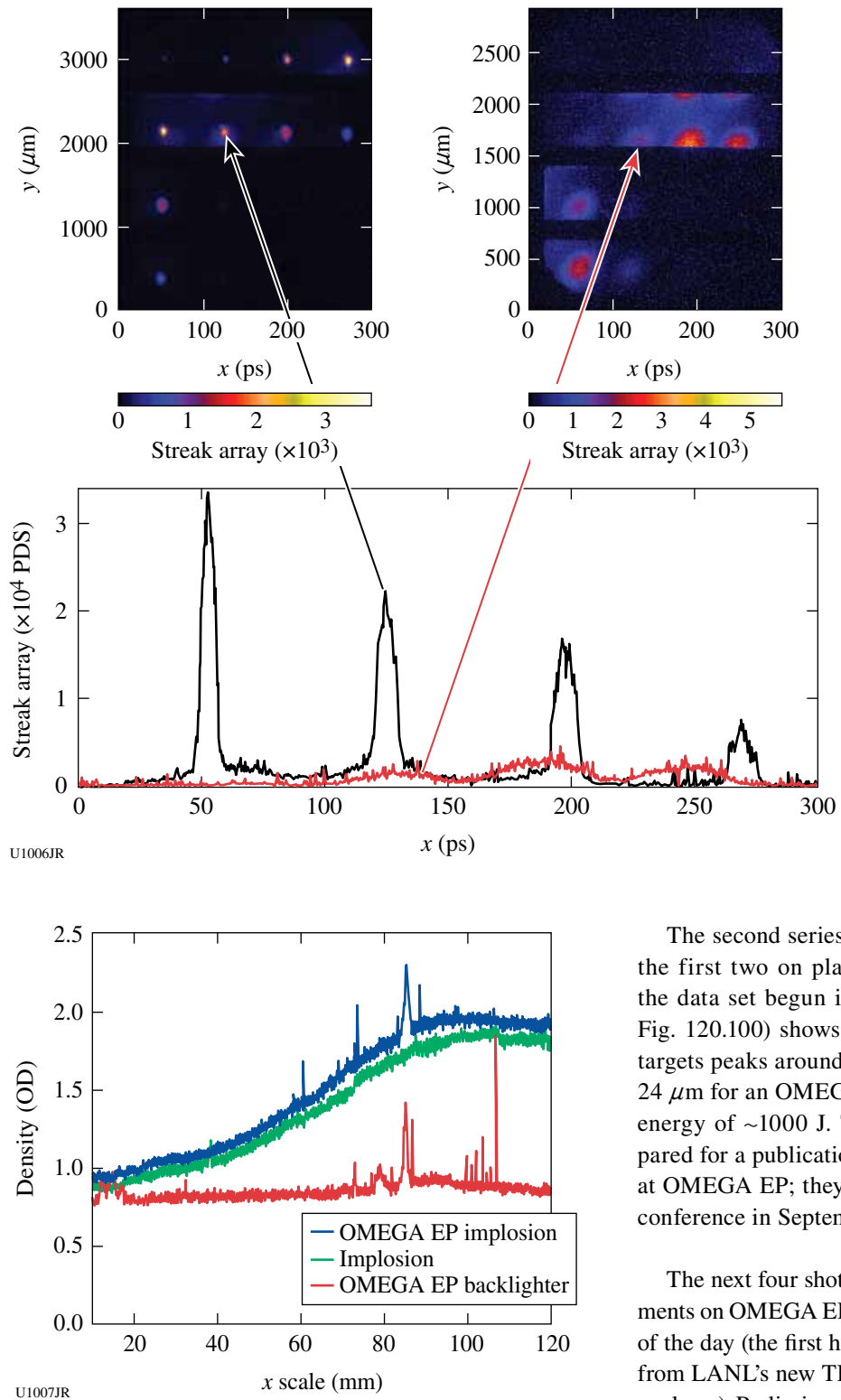


Figure 120.98

Spectral radiance measured by an XRS spectrometer showing the relative emissions of the implosion, backscatter, and the combined spectrum.

Figure 120.97
X-ray framing-camera images and lineouts from the OMEGA EP joint shots 53548 and 53549. Shot 53548 shows an image that includes the backscatter and the capsule, while shot 53549 shows the intensity of the backscatter only. The lineouts were taken from the second horizontal frame and show the relative intensity of the emission from the imploding capsule and the x-ray backscatter.

The second series of shots (18 August) yielded six shots, the first two on planar diamond foil targets, completing the data set begun in March. The completed data set (see Fig. 120.100) shows that proton beam energy from planar targets peaks around 45 MeV for a target thickness of about $24 \mu\text{m}$ for an OMEGA EP pulse length of 10 ps and a pulse energy of $\sim 1000 \text{ J}$. These results are currently being prepared for a publication documenting the first ions generated at OMEGA EP; they were also presented at the IFSIA 2009 conference in September.

The next four shots were used to perform focusing experiments on OMEGA EP using hemi-shell targets. The third shot of the day (the first hemi) was the first shot to give good data from LANL's new TPIE diagnostic (a ion energy and species analyzer). Preliminary analysis of the PFPII data indicates that the beam quality from the hemis is good and laminar.

The last shot explored the generation of ions over a large area of the hemi-shell (need for higher flux ion beam generation)

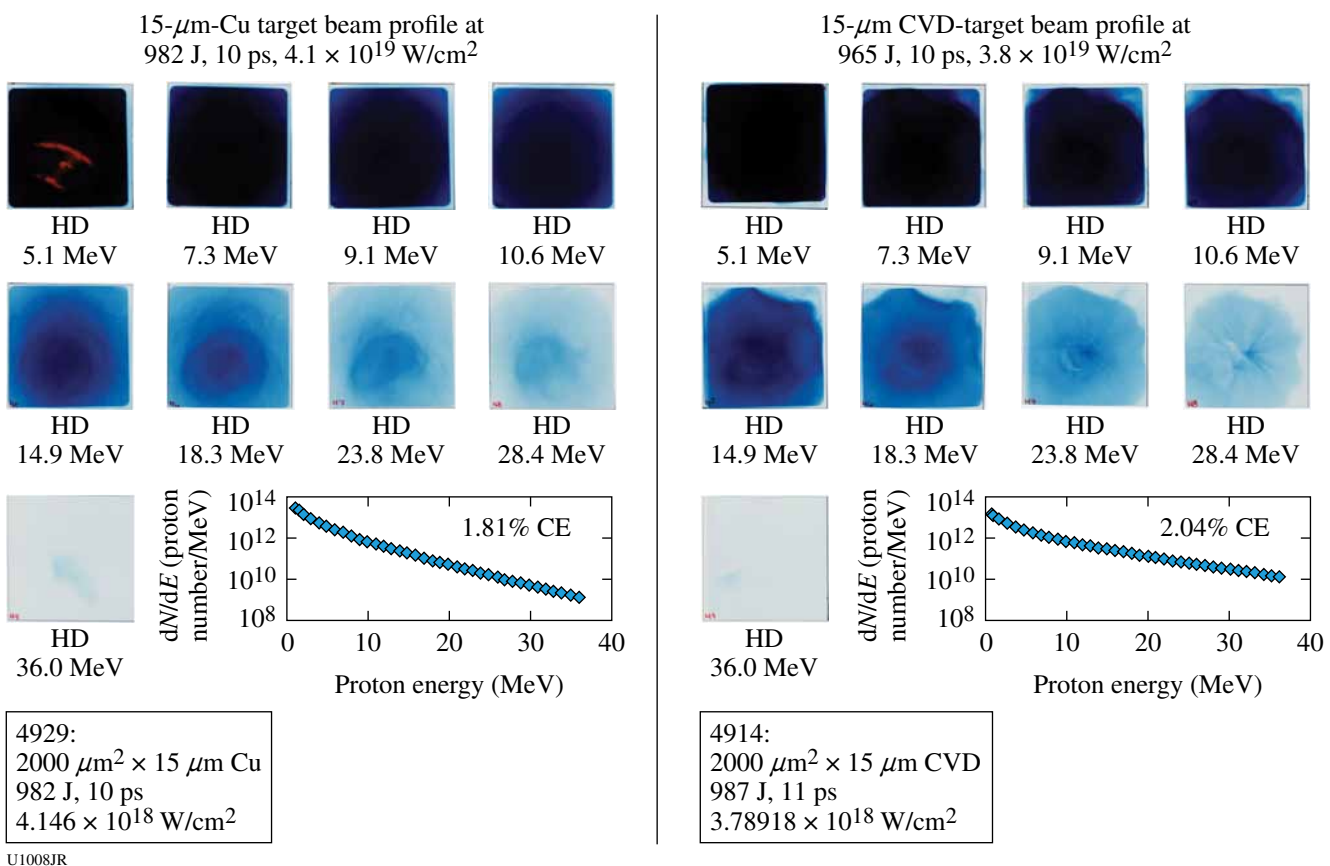


Figure 120.99

Comparison of 15-μm CVD diamond target (right panel) with 15-μm-copper target (left panel). The panels show PFPII data from the RCF film stack with energies associated for each layer, and a calculated proton spectrum fitting the data in the lower right of each panel.

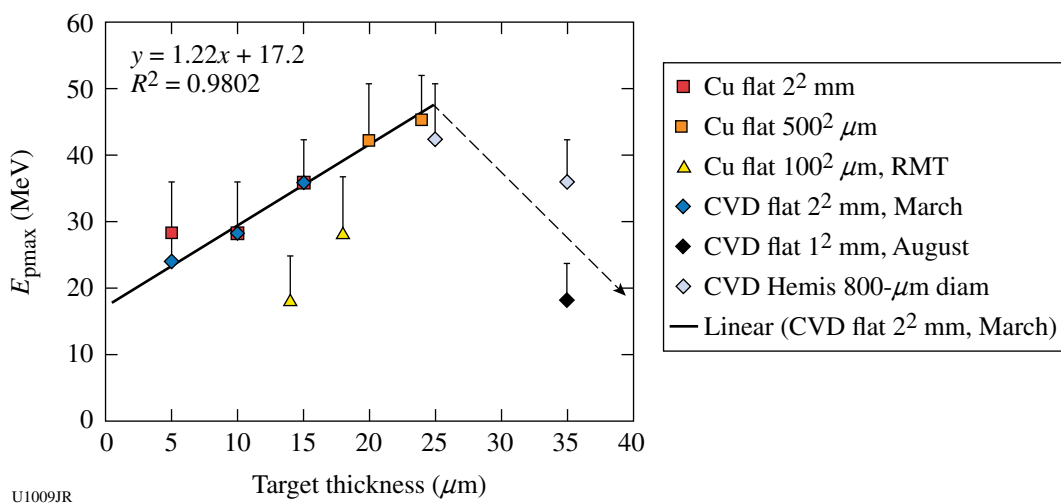


Figure 120.100

OMEGA EP proton scaling with target thickness and an area showing a linearly increasing trend toward 25-μm thickness for CVD (diamond) and Cu targets with areas greater than $100^2 \mu\text{m}^2$, with a drop after 25 μm and lower performance in general for targets with areas smaller than $500^2 \mu\text{m}^2$.

by using a large laser focus at the target. Data were generated using a copper grid behind the hemi that provided information on the focal quality of the ion beam. The TPIE diagnostic performed well in the completely retracted TIM position using a 250- μm pinhole aperture but with low flux. On a later shot, the TPIE was run in 30 in. and the CR39 moved to the 10-cm position to increase the flux and reduce noise. This provided us with information on the dynamic range of the TPIE instrument. Preliminary analysis of this data indicates that improved performance will be achieved if we add shielding to reduce the noise on the CR39.

Gamma Reaction History Diagnostics: A gamma reaction history (GRH) diagnostic has been developed for the National Ignition Campaign and thoroughly tested on OMEGA this year. The GRH is a follow-on design to the Gas Cherenkov Detector (GCD-1), which has been productive on OMEGA for the past ten years.³² Figure 120.101 depicts the GRH currently installed on OMEGA. It is designed to detect the 16.7-MeV gamma rays that are emitted in approximately one of every 10,000 DT fusion reactions. These gammas are converted, primarily through Compton scattering, to relativistic electrons inside the domed port cover. The electrons traveling faster than the speed of light in a pressurized gas generate UV/visible Cherenkov radiation, which is collected with off-axis parabolic reflectors into an ultrafast photomultiplier tube (PMT).^{33,34} Varying the pressure of the gas (typically CO₂ or SF₆) varies the index of refraction and hence the Cherenkov threshold (requires $v_e > c/n$, where v_e is the electron velocity, c is the speed of light, and n is the index of refraction of the gas). The electrical PMT signal is sent to a Mach-Zehnder modulator in the electronics

enclosure for optical transmission to digitizers without loss of bandwidth.³⁵ A complete system impulse response has been measured to be ~95 ps—fast enough to measure the expected burn widths of 80 ps to 150 ps from the THD campaign planned for the spring of 2010 at the National Ignition Facility (NIF). Fiber-optic connectors make it possible for timing fiducials and calibration signals to be injected directly into the optical path and provide a dry-run capability for verifiable reliability.

The higher laser energies and neutron yields expected at the NIF dictate larger standoff distances for diagnostics. The advantage of gamma rays over neutrons is that they do not suffer velocity Doppler spreading with increasing distance, so gamma-ray detectors can be placed a significant distance from the imploding capsule without loss of signal bandwidth. Increasing standoff distance, however, also reduces the subtended solid angle and therefore measurement sensitivity, so the instrument must be designed to maximize sensitivity. The GCD-1 routinely operates at 20 cm from target chamber center (TCC) by insertion into a ten-inch manipulator (TIM). This necessitated a compact, coaxial design utilizing Cassegrain optics. By mounting the GRH outside the chamber, we were able to take advantage of off-axis light collection utilizing off-axis parabolic mirrors for increased Cherenkov light collection. The GRH-6m at the NIF will be only two orders of magnitude less sensitive than GCD-1 at 20 cm, even though it will be located 30× farther away from TCC. For the NIF, the GRH-6m will consist of four gas cell channels run in parallel for increased redundancy and reliability plus the ability to run at several gamma-ray threshold energies to diagnose various gamma rays of interest [e.g., $t(d,\gamma)$ at 16.7 MeV, $t(h,\gamma)$

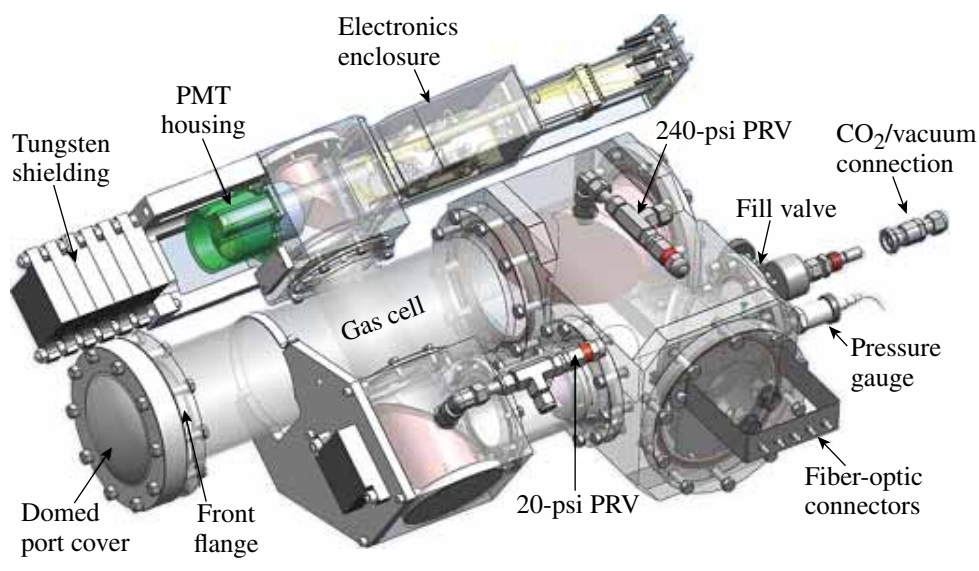


Figure 120.101
First GRH-6m channel, currently installed on OMEGA.

at 19.8 MeV, $^{12}\text{C}(n,n')$ γ at 4.4 MeV]. These detectors will be capable of measuring fusion bang times relative to the t_0 of the composite laser pulse to within 50 ps and burn widths to within 5 ps to 10 ps at yields $>1 \times 10^{13}$ at the NIF. These parameters will be key in diagnosing shell velocity and the various possible failure modes in attempts at ICF ignition on the NIF. The GRH may also prove useful as a means of providing a time-resolved measure of ablator ρR , indicative of ablator mass remaining and ablator/fuel mix.

Figure 120.102 shows a gamma-ray measurement from an imploded DT-filled plastic capsule with the GRH pressure with 100 psia of CO_2 (\sim 6-MeV Cherenkov threshold). Also shown is a background measurement from a previous shot with the CO_2 removed, resulting in no Cherenkov production, but still exhibiting direct gamma interaction with the PMT (this background is also present when the PMT input window is blocked with black tape). DT fusion gammas and $n-\gamma$ from DT fusion neutrons passing through the imploding capsule [primarily $^{12}\text{C}(n,n')$ γ from CH capsules] interact directly with the PMT, causing the “precursor” peak approximately 4.1 ns before bang time. The speed-of-light transit time from TCC through the optical delay of the Cherenkov cell is calculated to be 4.26 ns longer than the direct line-of-sight (LOS) transit time from TCC to the microchannel plate (MCP) in the PMT (i.e., directly through the tungsten shielding). Other experiments have shown that 6 in. of tungsten shielding is adequate to eliminate direct LOS gammas (and x rays), so the precursor from these shots with 9 in. of shielding must be from gammas originating at TCC reaching the MCP on scattering paths delayed approximately 160 ps relative to a direct LOS path, or an extra 4.8 cm. Addi-

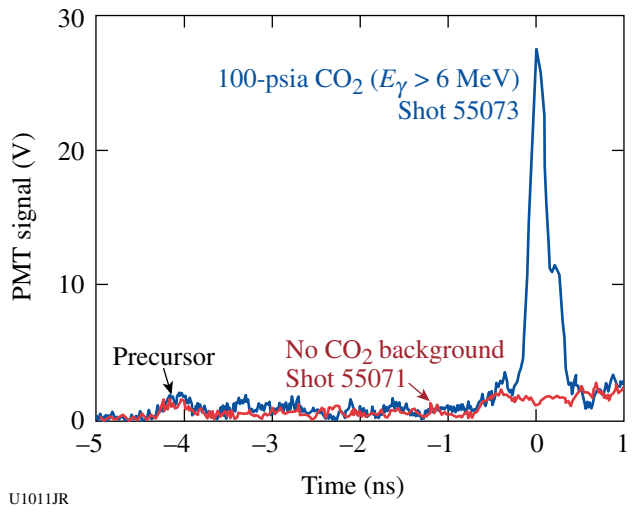


Figure 120.102
GRH data from high-yield shots with (blue) and without (red) pressurized CO_2 .

tional small peaks after the precursor are $n-\gamma$ generated by interaction of DT neutrons with mass near TCC. Similar peaks have been correlated with various TIM-based diagnostics as they are moved near TCC. These masses must be closer than 22 cm from TCC to generate a signal before or at bang time because of the slower transit time of the neutrons. Although the current background levels are adequate for bang-time and burn-width measurements, the shielding being designed for the NIF will do a much better job of further reducing the background.

In July the GRH was absolutely timed using x rays generated with 100-ps laser pulses directed onto gold ball targets. The γ -to- e^- converter in the GRH was replaced with a BC-422 x-ray sensitive scintillator for these shots. The x rays/scintillator photons have essentially the same transit time through the system as the γ rays/relativistic electrons/Cherenkov photons. As a result the x-ray pulse can be used to generate a t_0 time stamp on the scope from which the optical fiducial is calibrated. Figure 120.103 shows an x-ray shot and a high-yield shot overlaid by lining up the fiducials. The difference between the rising edge of the x-ray pulse and the peak of the fusion signal is representative of the absolute bang time.

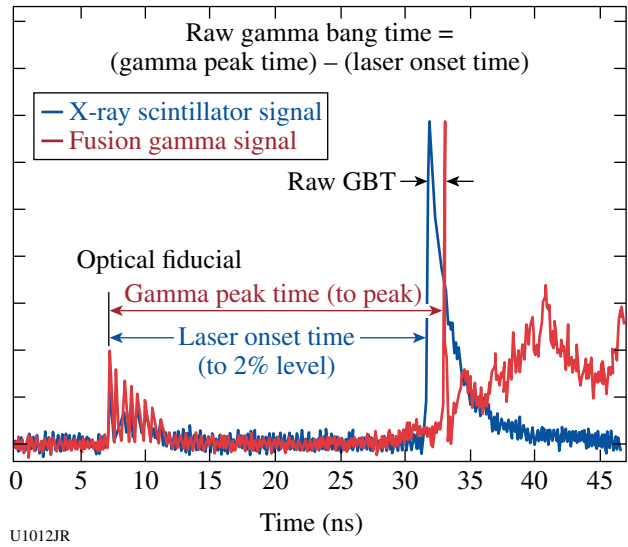


Figure 120.103
X-ray pulse from a gold ball target (blue) used to calibrate an optical timing fiducial overlaid with a Cherenkov signal from a high-yield DT shot.

In addition to the GRH development, the Gas Cherenkov Detector also continued to provide valuable insight into gamma-ray physics. In particular, a secondary gamma experiment (a.k.a., “hockey puck” experiment) was carried out using GCD-1. The primary experimental objective was to simulate the neutron-induced secondary gamma ($n-\gamma$) production

from a NIF hohlraum, thermomechanical package (TMP), and implosion capsule. During four shot days within FY09 (November, April, May, and July), three group of pucks were placed between TCC and GCD: (1) Au and Cu pucks for the hohlraum, (2) Al and Si pucks for the TMP, and (3) SiO_2 , Al_2O_3 , and BeO pucks for an implosion glass capsule $n-\gamma$ study. Three key experimental results were obtained in support of the NIF–GRH (gamma-ray reaction history) diagnostic development program:

1. Proximity $n-\gamma$ sources were experimentally characterized. The GCD detected time-delayed and Doppler-broadened $n-\gamma$ signals from all seven pucks. The high-bandwidth GCD can temporally distinguish DT– γ and $n-\gamma$ signals as long as the proximity source is located at least 2 cm from TCC. The $n-\gamma$ sensitivity's dependence on seven materials was found and used to validate the MCNP code. Silicon produced the strongest $n-\gamma$ signal as expected by MCNP simulations.
2. It was experimentally confirmed that the GCD can cut off $n-\gamma$ signals effectively by adjusting energy threshold, which will allow one to measure clean DT– γ without interference of $n-\gamma$ at the NIF. At 9-MeV threshold, it is expected that DT– γ will be at least 10× higher than $n-\gamma$ signals.
3. $n-\gamma$ signals from the hockey puck experiment were used for MCNP/ACCEPT code validation. Also, puck signals served as an *in-situ* GCD calibration source; as a result they provided one method to determine the $D(T, \gamma)/D(T, n)$ branching ratio. Preliminary calculations carried out using four puck materials indicate $D(T, \gamma)/D(T, n)$ ranges from 1×10^{-5} to 4×10^{-5} .

Defect Implosion Experiment (DIME): The Los Alamos DIME campaign involves perturbed spherical implosions, driven by 60 OMEGA beams with uniform, symmetrical illumination (~24 kJ). DT-filled CH-shell targets with equatorial-plane defects are designed to produce a nonspherical neutron burn region. The objectives of the DIME series are to observe the nonspherical burn with the neutron imaging system (NIS) and to successfully simulate the physics of the neutron production. For the first shot day on OMEGA (shots 54135 to 54145), we demonstrated adequate yield for NIS imaging and monitored yield degradation for the presence of defects. The targets had a diameter of 860 μm . All were filled with 5 atm of DT. We used two separate shell thicknesses: 8 μm and 15 μm , thereby testing both exploding pusher and ablative designs. Perfect targets have no defects. Target defect details are shown in Fig. 120.104. For all shots, the groove depth was 2 μm .

The yield compared to perfect capsules was reduced by ~50% for both thick- and thin-walled targets with defects (see Fig. 120.105), although the exploding pusher capsules (thin walls) performed better for total yield. Both the NIS and a gated, x-ray framing camera diagnosed target emission edge-on—in the plane of the defect. In all cases, the NIS obtained neutron images but was not optimal for resolving the defect. This is encouraging because the perturbation was minimal, and additional degradation for larger defects should be less disruptive of yield. Numerical simulations predicted enhanced x-ray emission, as suggested in Fig. 120.106. During the next campaign, experiments will feature larger, deeper channel defects, and the NIS will be more mature.

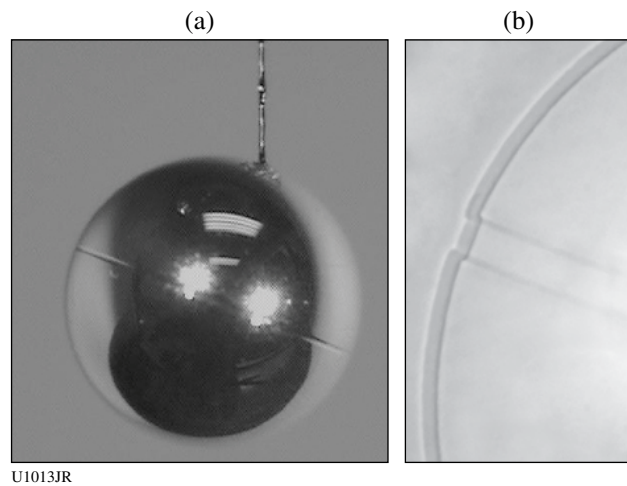


Figure 120.104
(a) LLE photograph of a target with a 20- μm -wide groove defect. (b) A General Atomics radiograph of a 30- μm wide defect with high magnification.

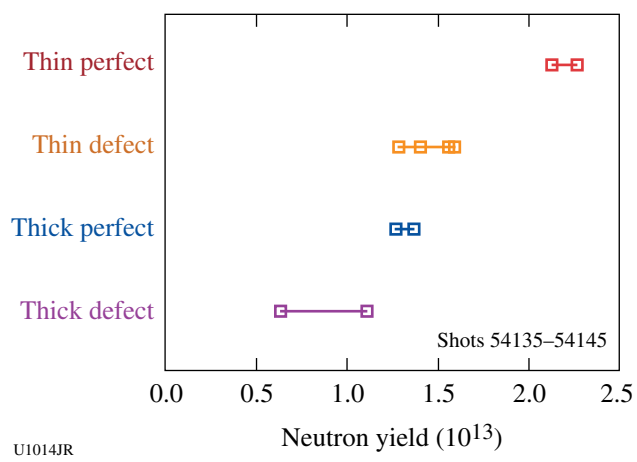


Figure 120.105
Yield for 20- μm -wide, 2- μm -deep groove defects.

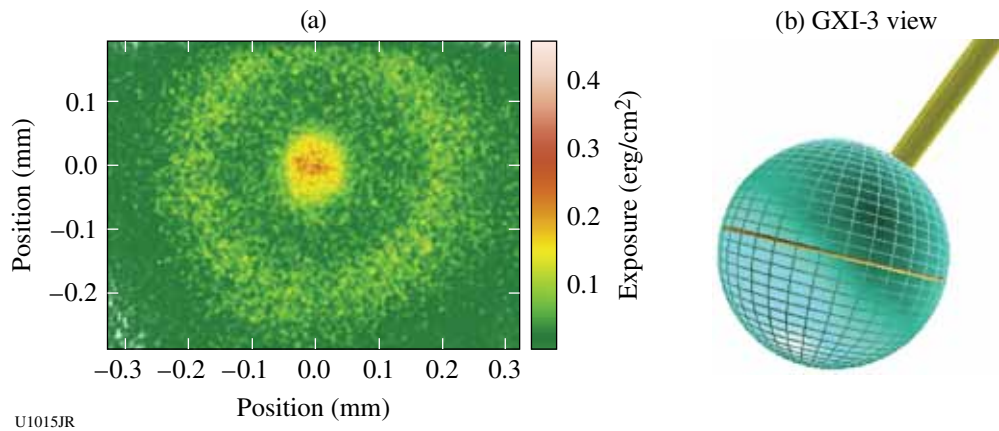


Figure 120.106

(a) A gated, x-ray image (3 to 5 keV) of a defect target implosion suggests enhanced x-ray emission (higher density) in the plane of the defect. (b) The VISRAD view of the GXI-3 x-ray framing camera.

High-Energy Backlighting on OMEGA EP: At the end of January 2009 Los Alamos participated in the first international collaboration on OMEGA EP along with LLE, LLNL, LULI, and NRL. These experiments produced high-quality x-ray images of static gold grids using silver K_{α} emission produced from 100-ps, 1-kJ laser pulses (Fig. 120.107).

Los Alamos experiments in March 2009 were in collaboration with NRL and were limited to the spectroscopic evaluation of high-energy x-ray backscatterers (imaging diagnostics were not available because of requalification). A scan of x-ray yield as a function of pulse duration of silver K_{α} emission was performed and measured with the NRL diagnostic dual-crystal

spectrometer (DCS), which is a high-energy Laue configuration spectrometer. Excellent data were obtained with the spectrometer showing very little change in conversion efficiency with pulse durations ranging from 10 ps to 100 ps.

Neutron Imaging: The Neutron Imaging Campaign made great advances with the NIS to be fielded on the NIF during FY09. Using a staggered approach, different components of the NIF Ia neutron imaging system were tested to ensure that each component functioned properly. The spatial resolution and the DQE of the NIF Ia detector were determined from these experiments. The response and time delay of new paddle detectors were also measured.

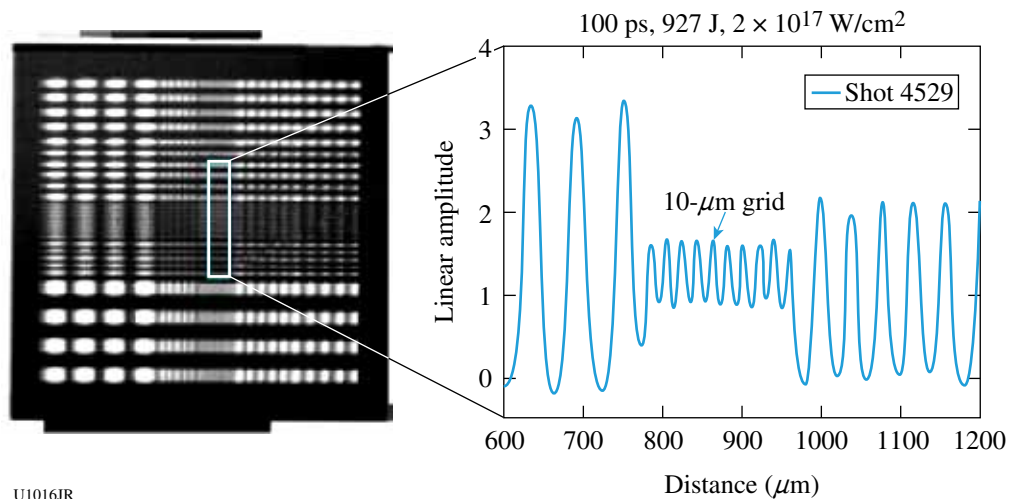


Figure 120.107

(a) A radiographic image of a resolution grid using a silver backscatterer. (b) A lineout from the radiograph demonstrating high spatial resolution.

FY09 AWE OMEGA Experimental Programs

AWE-led experiments on OMEGA in FY09 continued to test radiation-hydrodynamic simulations of hohlraum drive and capsule implosion under conditions where a hohlraum target was driven in a deliberately asymmetric manner.

Techniques to achieve uniform, near-spherical symmetry of radiation drive on a capsule in a laser-heated hohlraum have received detailed attention in the context of inertial confinement fusion. Much less attention, however, has been paid to understanding the hohlraum physics and hydrodynamics in cases where the radiation drive departs significantly from spherical symmetry. In work on the OMEGA laser, AWE has carried out a series of experiments to study the implosion dynamics of a capsule irradiated by a deliberately asymmetric x-ray drive. The experimental data provide a sensitive test of radiation transport within the hohlraum enclosure in which drive symmetry was modulated by using variable albedo layers (low-Z coatings on the high-Z hohlraum wall), asymmetric laser-beam timing, and other techniques. In cases where the radiation drive was highly asymmetric, the imploding capsule developed a well-defined polar jet that interacted with the opposite capsule wall. The hydrodynamics of jet formation and interaction were investigated using x-ray backlighting radiography, providing a sensitive test of hydrodynamic modeling in this strongly converging geometry.

A 1.6-mm-diam, 2.7-mm-overall-length hohlraum was used (Fig. 120.108) and driven with up to 30 beams (1.6-ns pulse duration) from the OMEGA laser. Asymmetry was introduced

by means of an imbalance of laser energy or timing between the two ends of the hohlraum, or by asymmetry of wall material. In some cases the wall material of one half of the hohlraum cavity was aluminum (low albedo, in comparison with the gold wall material of the other half of the hohlraum); in other cases a thin aluminum coating on the gold hohlraum wall was used to introduce a time-varying albedo (low albedo at early time, followed by increased drive after the laser beams burned through the aluminum layer).

Both silica aerogel spheres (600- μm diameter, 325-mg cm^{-3} density) and thin-walled glass capsules (600- μm diameter, 3.5- μm wall thickness, 30- μm -thick CH ablator coating) were used as diagnostics of the angular distribution of radiation drive. The position of the ablation front in the aerogel witness spheres^{36,37} was used to characterize the angular distribution of the drive, whereas the integral effect of asymmetric drive on the implosion hydrodynamics³⁸ was observed in the late-time evolution and jet formation of the thin-shell capsules. Both were diagnosed by x-ray backlighting, using a 4.75-keV titanium area backscatter and x-ray framing camera. Hohlraum wall emission was also characterized using the Dante diagnostic, viewing through the laser entry hole of the hohlraum. The experiments were modeled using the AWE Lagrangian radiation-hydrodynamics code NYM, followed by the Eulerian code PETRA to which the simulation was linked after the mesh in the Lagrangian phase of the simulation became sufficiently distorted to limit further progress. The hydrodynamics simulation was post-processed to generate synthetic radiographs for comparison with the experimental data.

The position of the ablation front in the aerogel witness-sphere experiments was characterized by its decomposition into Legendre polynomials. Figure 120.109 shows a comparison between the amplitudes of Legendre moments from both the experimental data and simulation. The simulation was shown to reproduce the experiment rather closely.

The hydrodynamics of the thin-shelled capsules was significantly more sensitive than that of the foam witness balls to the angular distribution of drive. Figure 120.110 compares experimental data with post-processed images for a NYM-PETRA simulation at different times after the onset of the radiation drive. The hydrodynamics is seen to progress somewhat slower in experiment than simulation (as quantified by the equatorial diameter), and although both experiment and simulation show a well-defined polar jet at late time (Fig. 120.111), the density distribution at the hot pole of the capsule was different in the two cases. It seems likely that these differences arose from

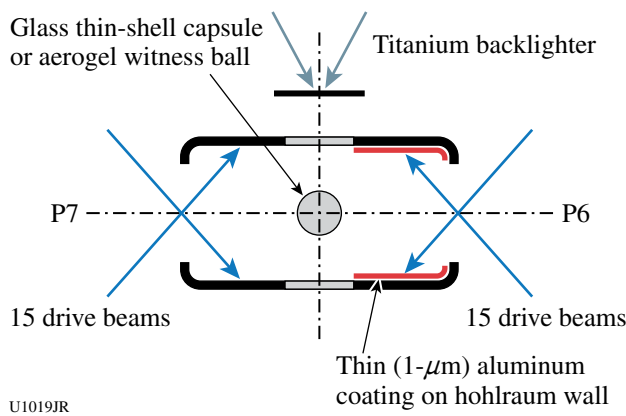


Figure 120.108
Experiment to investigate asymmetric hohlraum drive. The hohlraum was aligned on the P6–P7 axis of the OMEGA target chamber, and asymmetry was introduced by imbalance of laser beam energy and timing from the P6 and P7 directions, and by the use of a low-Z coating on the hohlraum wall.

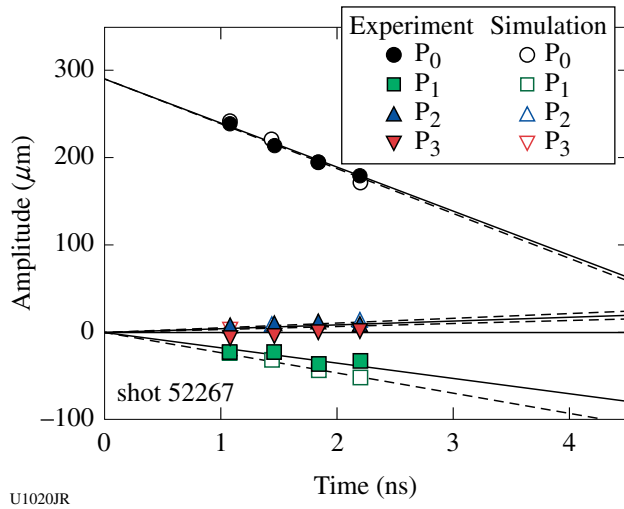


Figure 120.109

Legendre polynomial decomposition of the position of the ablation front in an asymmetrically driven foam witness-ball experiment. The amplitudes of the first four Legendre polynomials (P_0 , P_1 , P_2 , P_3) are shown for both experiment (filled symbols) and simulation (open symbols).

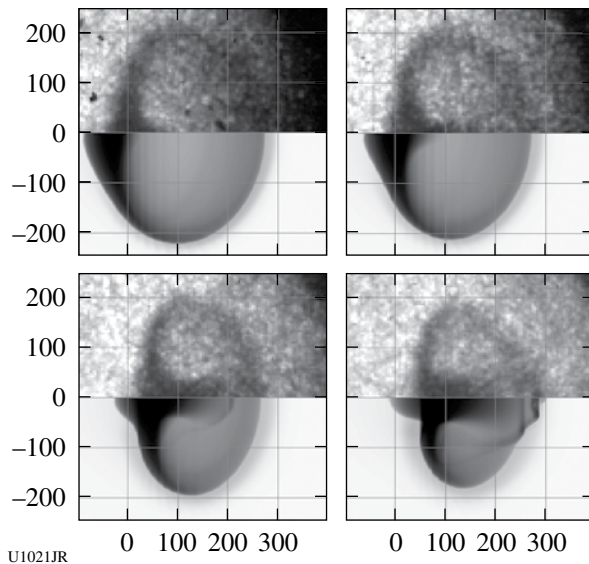


Figure 120.110

Sequence of frames showing experimental data (top) and simulation (bottom) of the implosion of an asymmetrically driven, thin-shell glass capsule. The sequence of times is 2.8, 3.2, 3.6, and 4.0 ns in the experimental data and 2.6, 2.8, 3.0, and 3.4 ns in the simulation. In the simulation, times were chosen to match approximately the experimentally observed equatorial diameter of the capsule. The formation and propagation of the polar jet were reproduced in the simulation, although there are some differences of density distribution at the pole of the capsule. (Units shown are microns.)

subtle differences in the laser hot-spot position, or the albedo of the indirectly heated hohlraum wall, and resolving these differences will form the focus for further work during FY10.

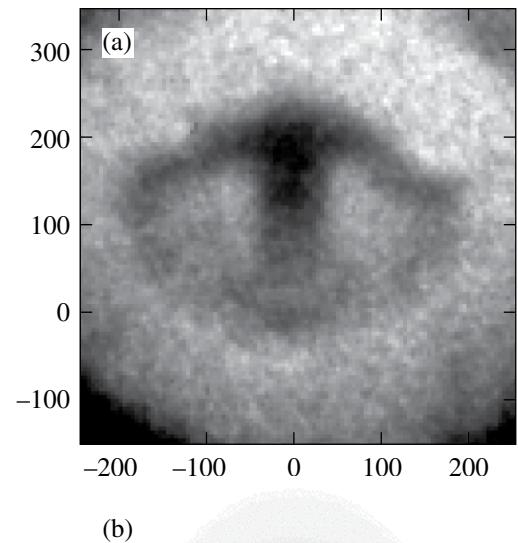


Figure 120.111

The bow shock produced on interaction of the polar jet with the opposite wall of the capsule is clearly seen in (a) experiment (top) and evident also in (b) simulation (bottom).

FY09 CEA OMEGA Experimental Programs

CEA conducted 56 shots on the Omega Laser Facility in FY09. The CEA efforts included the following:

CEA Copper Activation Diagnostic for Primary DT Neutron-Yield Measurement: The neutron yield is one of the most important parameters used to characterize the performance of inertial confinement fusion experiments. For the Laser Megajoule (LMJ) and National Ignition Facility (NIF), neutron-yield measurements will be performed by an array of neutron time-of-flight (nTOF) detectors composed of scintillation counters and chemical vapor deposition (CVD) diamond detectors. An accuracy of 4% is required to measure neutron yield. All these detectors are calibrated against the nuclear activation diagnostic, which is a valuable measurement technique because of its reaction threshold and its absolute calibration. The copper activation method is used for the 14.1-MeV primary DT neutron-yield measurement. This diagnostic has been used as a reference on many laser facilities (PHEBUS, NOVA, OMEGA) and will now be used on future megajoule-scale lasers. Copper activation will be the first nuclear diagnostic installed on LMJ.

The copper disk to be used for this diagnostic is pure copper (99.99%) and is composed of 69.2% of ^{63}Cu and 30.8% of ^{65}Cu . The $^{63}\text{Cu}(\text{n},\text{2n})^{62}\text{Cu}$ reaction has a Q value of 11 MeV. ^{62}Cu decays with a half-life of 9.73 min and emits a positron, resulting in the production of two back-to-back 511-keV gamma rays on annihilation. On the other hand, the $^{65}\text{Cu}(\text{n},\text{2n})^{64}\text{Cu}$ reaction produces ^{64}Cu that decays with a half-life of 12.7 h and emits a positron. The CEA activation acquisition system consists of two 7.62-mm-diam, 7.62-mm-thick NaI(Tl) scintillation detectors. Associated electronics allow us to detect 511-keV gammas in coincidence between two detectors. In 2002 the activation diagnostic was calibrated on a Van De Graaff accelerator at CEA Bruyères le Châtel with an accuracy of 4.5%. The main error contribution comes from the reference detector, which measures the neutron yield delivered by the accelerator. The optimum sensitivity is obtained by using a 10-mm-thick copper disk because it is the best compromise between copper activation and 511-keV gamma detection. We use a 7.62-mm-diam copper disk that is similar in dimension to the NaI(Tl) detectors.

To compare CEA and LLE primary DT neutron calibration, a CEA copper activation diagnostic was implemented on OMEGA during direct-drive implosions of DT capsules yielding 10^{13} primary DT neutrons. The tertiary activation diagnostic (TAD) inserter was used to place copper disks at 40 cm and 100 cm from target chamber center (TCC). Immediately after the shot, the TAD inserter was retracted and the

activated copper disk was extracted from the target chamber. The disk was then dropped into a plastic container by the Target Bay operators and carried to the acquisition systems to be measured. Data acquisition began about 10 min after the shot, and measurements were made every minute for at least 2 h to properly describe the ^{62}Cu and ^{64}Cu decays (see Fig. 120.112). This acquisition technique allows us to remove the ^{64}Cu decay contribution to evaluate the neutron yield with the ^{62}Cu decay only. Since OMEGA shots are at about 1-h intervals, we used two acquisition systems.

A 10-mm-thick, 7.62-mm-diam copper disk was used during the three first shots performed in February 2009 to test our operating procedure (shots 53590 to 53592). We decided to use this sample geometry because its calibration is well known with an accuracy of 4.5%. However, the high copper activation level produced by a 10^{13} neutron yield results in an acquisition system saturation with a dead time of 40% about 30 min after the shots. Therefore, neutron yield was determined using data below a coincidence count rate of 300 c/s. Counting-station saturation is a crucial problem because it prevents us from determining the primary DT neutron yield from ^{62}Cu decay when the ^{64}Cu contribution is minimum, even if it was previously calibrated. To reduce acquisition system saturation in the later shots taken in May, we used 3-mm-thick copper disks placed at 1 m from TCC.

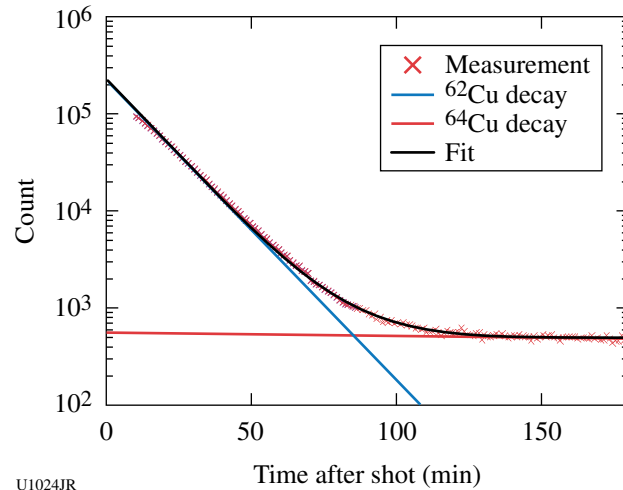


Figure 120.112
 ^{62}Cu and ^{64}Cu decays measured at 1 m from TCC with a 3-mm-thick disk during shot 54460 yielding 2×10^{13} neutrons.

The primary DT neutron yield was compared to the LLE time-of-flight scintillation counter located at 12 m from the target (12mnTOFh). The CEA copper activation diagnostic was used on 19 DT shots. The neutron yields in these experiments ranged from 8.9×10^{12} to 3×10^{13} . The neutron-yield measurement accuracy was 4.6%. Except for one shot (54471), nTOF measurements were consistent with the CEA copper activation. If we compare shot-to-shot CEA copper activation and LLE nTOF measurements, the dispersion is about 3.6% (rms) and the average difference between primary DT neutron-yield calibrations is only 1.8% (see Fig. 120.113).

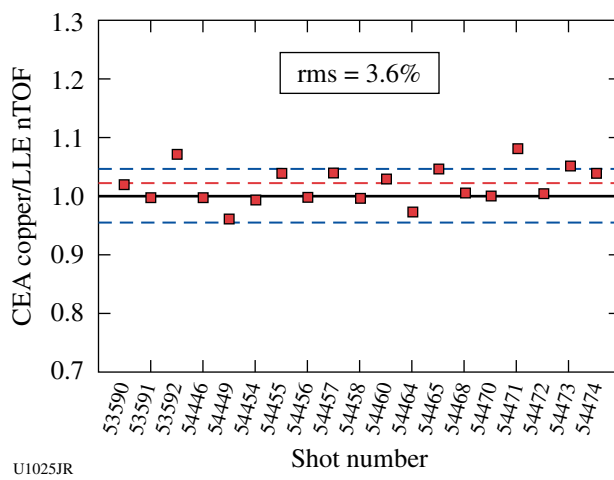


Figure 120.113

Shot-to-shot comparison between CEA copper activation and nTOF neutron-yield measurement. The two independently calibrated neutron-yield diagnostics show a dispersion of 3.6% (dashed blue line) with an average difference of 1.8% (dashed red line).

The 2009 copper-activation measurement campaign confirmed that the CEA and LLE independent neutron-yield calibrations are very close.

It is worth noting that, compared to a 10-mm-thick geometry, the sensitivity of the 3-mm-thick sample was determined with only one calibration measurement at 14.1 MeV. The best way to reduce statistical effects is to perform several measurements with exactly the same sample geometry at the same energy. For this reason, two calibration weeks have been scheduled between 16 and 27 November 2009 on the 4-MV Van de Graaff accelerator at CEA (Bruyères le Châtel). All data acquired on OMEGA will be processed again with this new calibration to determine final results.

MeV Photon X-Ray Sources Produced on OMEGA EP: High-power laser-plasma experiments have been used for sev-

eral years to study the generation of energetic particles. With chirped-pulse-amplification laser systems, the interaction of a high-intensity laser pulse ($I\lambda^2 > 10^{19} \text{ W/cm}^2 \mu\text{m}^2$) with a gas-jet or thin-foil target leads to the generation of relativistic, multi-MeV electrons, accelerated from many physical processes, such as the Brunel effect, ponderomotive or $j \times B$ acceleration, and Wakefield acceleration. If they propagate in a high-Z solid target located behind the interaction area, these relativistic electrons will generate copious high-energy Bremsstrahlung emission. These x-ray photons can be an interesting bright high-energy ($>1 \text{ MeV}$) source for radiography, nuclear activation, radiation effects, and radiation safety studies.

Two experiments were carried out using the “backlighter” of the OMEGA EP laser. For the first experiment performed in a high-power regime (CEA/LLE collaboration), the short pulse delivered up to 300 J in $\tau = 0.6 \text{ ps}$ at a wavelength of $\lambda = 1.053 \mu\text{m}$. The short pulse was focused at the center of the vacuum chamber, at 45° of the normal to the target. Peak laser intensity was estimated to be $\sim 4 \times 10^{19} \text{ W/cm}^2$. Two types of targets were irradiated: 20- μm -thick ($500 \times 500 \mu\text{m}^2$) and 100- μm -thick ($200 \times 200 \mu\text{m}^2$) square gold foils.

For the second experiment performed in a high-energy regime (CEA/AWE collaboration), the short pulse delivered up to 1 kJ in $\tau = 10 \text{ ps}$ and was focused at the center of the vacuum chamber, at 18° off the normal to the target. The peak laser intensity was estimated to be $\sim 8 \times 10^{18} \text{ W/cm}^2$ and the target was a 2-mm-thick, 2-mm-diam Ta cylinder coated with 10- μm -thick plastic. For some of the shots, a nanosecond heating beam (1 kJ, 1 ns, $\phi = 800 \mu\text{m}$) was used to produce a preformed plastic plasma that was intended to increase the short-pulse energy absorption. Since no phase plate was available for the heating beam, a large focal spot was obtained by defocusing the beam.

In these experiments, the ratio $d/(c\tau/2)$, where c is the speed of light in vacuum and roughly corresponds to the speed of the fastest electrons and d is the target thickness, is close to 1 for thin targets (<1 for a 20- μm target and >1 for a 100- μm target) and is well above 1 for a 1-mm-thick target. Electron recirculation in the target is therefore expected to result in greater bremsstrahlung emission and a larger source size in thinner targets.

The high-energy part ($>10 \text{ MeV}$) of the x-ray spectrum was studied from $^{63}\text{Cu}(\gamma,n)^{62}\text{Cu}$ and $^{12}\text{C}(\gamma,n)^{11}\text{C}$ photonuclear reaction measurements. Assuming a Maxwellian distribution for the spectrum $S(E) \sim K_h \exp(-E/T_h)$, where K_h is the amplitude

of the spectrum, T_h can be deduced from an activity ratio measurement. The x-ray dose is inferred using x-ray dosimeters and from the radiography of a tower of Hanoi-shaped structure composed of W (tungsten). The x-ray source size is estimated using a penumbral imaging diagnostic (cylindrical 80-mm-thick W pinhole) and also from the radiography of an image quality indicator (IQI). This IQI is made of two 20-mm-diam W hemispheres with internal sinusoidal modulations. The signal is recorded using image plates combined with Ta reinforcement screens that increase the plate sensitivity for high-energy photons.

Figures 120.114(a) and 120.114(b) show spatial profiles of penumbral images obtained during the high-power-regime experiment with 20- μm -thick and 100- μm -thick gold targets, respectively. These profiles can be estimated with an edge

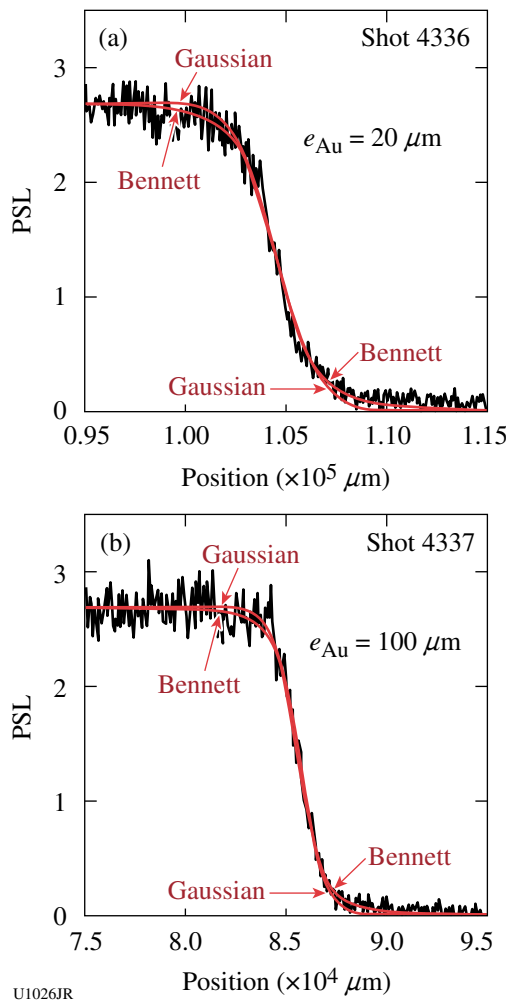


Figure 120.114
Spatial profiles of penumbral images obtained from laser shots on (a) 20- μm -thick and (b) 100- μm -thick gold foils.

response function associated to an x-ray source with either a Bennett or a Gaussian radial profile. The Bennett fit gives a source size of FWHM = 160 μm (resolution $\sim 40 \mu\text{m}$) for the 20- μm -thick foil and FWHM = 90 μm (resolution $\sim 30 \mu\text{m}$) for the 100- μm -thick foil. Surprisingly, a larger x-ray source size was obtained with the thinnest foil. This may be explained by the electron recirculation in targets of different sizes. Activation measurements show a quite high temperature $T_h \sim 10 \pm 4 \text{ MeV}$ for 100- μm -thick foils and a significantly lower temperature $T_h \sim 5 \pm 1 \text{ MeV}$ for 20- μm -thick foils. The effects of electron circulation on bremsstrahlung emission and x-ray source dimensions will be studied using the PIC numerical code Calder coupled to the Monte Carlo code MCNP.

Results from the second experiment using a thick Ta target (2 mm) in a high-energy laser regime show a relatively large x-ray source, FWHM = 400 μm (resolution $\sim 130 \mu\text{m}$), when the heating beam was combined with the short pulse [Fig. 120.115(a)]. Analysis of the radiographic image of the IQI [Fig. 120.115(b)] indicates that a smaller x-ray source (below 200 μm) was obtained when only the short pulse was focused on target, which is in agreement with past results obtained on other laser facilities. The results also show that the x-ray dose produced with only the short pulse was almost one order of magnitude larger than when the heating beam was combined. Since this long pulse had to be defocused here to produce large preformed plasma, the short pulse probably encountered inhomogeneous plasma with transverse density gradients that can lead to laser refraction. Phase plates should be available in FY2010 for long pulse and will be used for the next experiment.

CEA γ -Background Measurements after High-Neutron-Yield Shots on OMEGA: Knowledge of γ doses produced after high-neutron-yield shots is very important for the nuclear safety of megajoule-class laser facilities (NIF and LMJ). Indeed, neutrons produced during fusion reactions can activate the structural materials in the experimental hall, and γ background levels should be monitored after high-neutron-yield shots (DT implosions). Experiments dedicated to these measurements on OMEGA were initiated in 2005 and were continued in 2008 and 2009. These results will allow us to validate Monte Carlo activation calculations and therefore better predict γ background levels after high-gain shots on LMJ.

γ -Dose-Rate Measurements with a FH40 Dosimeter. During the two first campaigns (2005 and 2008), a FH40 dosimeter (based on a plastic scintillator) was used to perform the measurements [see Fig. 120.116(a)]. This dosimeter can measure the γ -dose rate per second (in $\mu\text{Sv}/\text{h}$) in the range of 40 keV to

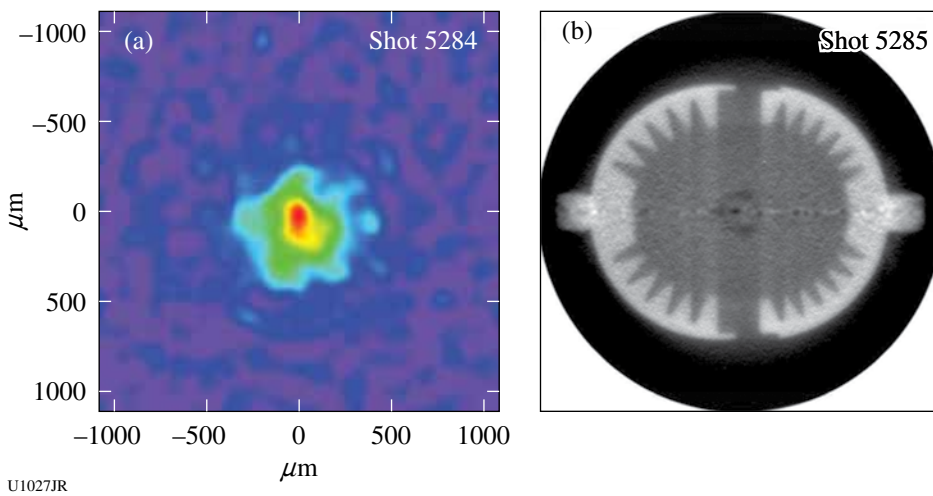


Figure 120.115
Reconstructed image of (a) the x-ray source and (b) radiography of the IQI after tomography obtained during the high-energy laser regime experiment.

1.3 MeV. The dynamic range covers 10 nSv/h up to 100 mSv/h with a 5% uncertainty.

In May 2008, we performed γ -dose-rate measurements at three positions [see Fig. 120.116(b)]:

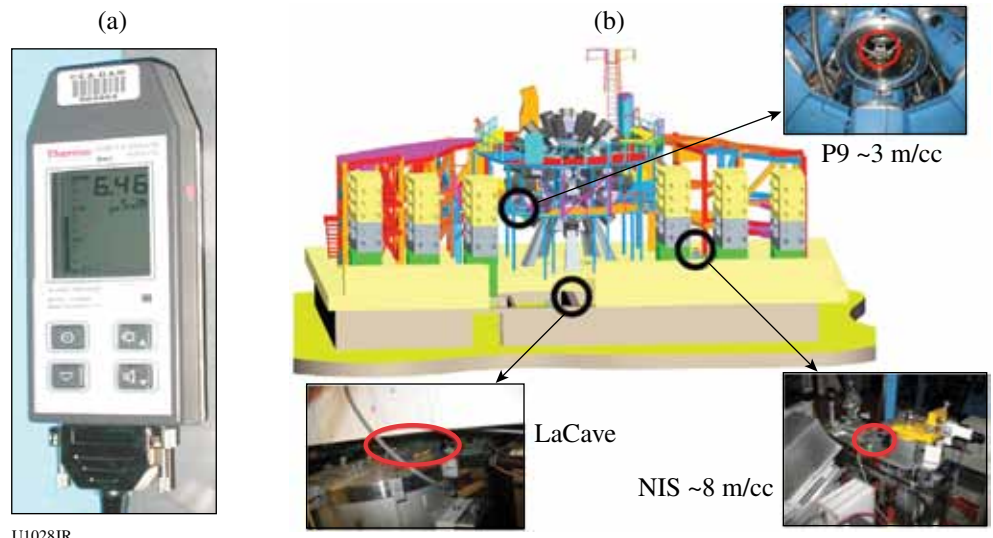
- at ~ 8 m from TCC in the Target Bay [near the CEA-neutron imaging system's (NIS) alignment station]
- at ~ 3 m from TCC in the Target Bay (in the P9 port), and
- in La Cave, just below the target chamber, under the 70-cm concrete slab

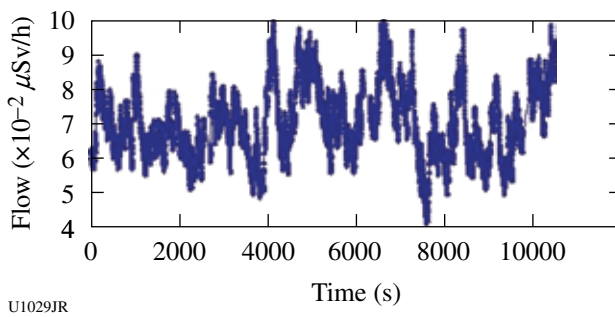
Figure 120.117 shows the γ -dose rate measured by the FH40 dosimeter in La Cave before the high-neutron-yield shot campaign. The mean residual background was $0.07 \pm 0.02 \mu\text{Sv}/\text{h}$.

Similar results were obtained in the Target Bay. During this high-yield shot campaign (21–22 May 2009), 23 shots were recorded (ten at the NIS position, eight in the P9 port, and five in La Cave), for neutron yields ranging from 2.46×10^{12} to 4.3×10^{13} . A typical signal obtained with the FH40 dosimeter is shown in Fig. 120.118, for the “NIS” position (at ~ 8 m from TCC).

Similar temporal behavior was observed in all three positions. At least three materials with a high half-life (>1 min) were activated (red lines on the curve of Fig. 120.118). These results have to be compared with calculations and predictions of Monte Carlo simulations.

Figure 120.116
(a) The FH40 dosimeter; (b) the three positions for the FH40 dosimeter.





γ Spectroscopy with a Germanium Detector. To obtain more-detailed results on this γ background after high-neutron-yield shots, γ spectroscopy was performed with a germanium detector in May 2009. This detector was an N-type germanium coaxial diode with 85% relative efficiency (see Fig. 120.119). The dimensions of the germanium crystal were 79 mm in diameter and 62 mm in length. The resolution was 2 keV for a 1-MeV γ , and the detectable energy range was 100 keV to 3 MeV. To avoid the use of liquid nitrogen, the crystal was cooled with an electronic cryogenic module.

Figure 120.118
 γ -dose rates recorded on OMEGA for shot 51298 (“NIS” position) with the FH40 dosimeter.

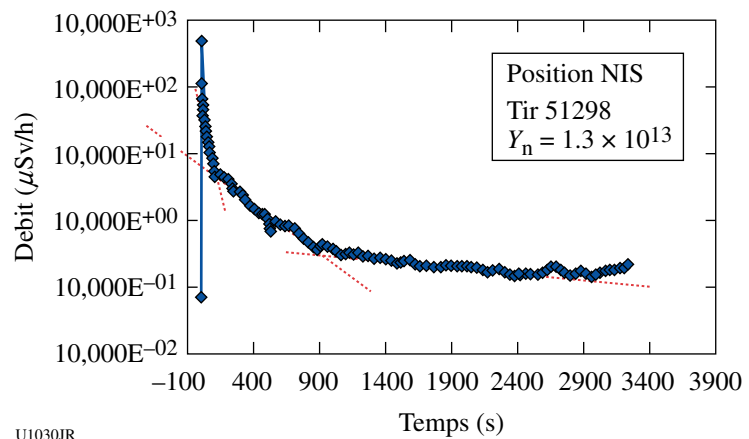


Table 120.XIII: Gamma-ray rates predicted using a Monte Carlo activation calculation for a 5×10^{13} -neutron-yield OMEGA shot at 4 m from TCC.

Time after shot	Rate ($\text{γ}/\text{cm}^2$)	Main radionuclide	Reaction channel	$T_{1/2}$
10 s	5.2×10^2	^{27}Mg	$^{27}\text{Al}(\text{n},\text{p})^{27}\text{Mg}$	9.46 min
100 s	2.3×10^2	^{24}Na	$^{27}\text{Al}(\text{n},\alpha)^{24}\text{Na}$	14.66 h
1000 s	4.7×10^1	^{24}Na	$^{27}\text{Al}(\text{n},\alpha)^{24}\text{Na}$	14.66 h

To protect the electronic device, the detector was inactive during the shot. The high voltage was turned on 2 to 3 min after the shot. To observe the decay time of γ rays, γ spectra were recorded each minute. Figure 120.120 presents a background γ spectrum recorded before the high-neutron-yield shots campaign during a 10-h period. For example, one can clearly see the 1460.8-keV γ ray coming from the ^{40}K nucleus. Other radioactive nuclei present in the environment (concrete, etc.), derived from uranium or thorium, may be identified in the spectrum.

For this campaign (13–14 May 2009), 15 shots were recorded (nine shots in NIS position, four near the aluminum chamber, and two in La Cave). The γ spectrum of Fig. 120.121 was obtained for shot 54446 ($Y_n = 2.58 \times 10^{13}$). The germanium detector was located in the NIS position, at ~ 8 m from TCC. The spectrum shows all γ rays recorded by the germanium detector during the 64-min period after the shot.

Some reaction channels are clearly identified:

- $^{27}\text{Al}(\text{n},\text{p})^{27}\text{Mg}$
- $^{27}\text{Al}(\text{n},\alpha)^{24}\text{Na}$

We also identified neutron activation of iron present in the OMEGA Target Bay structure and also neutron capture on ^{27}Al (because of slow neutrons diffused by the environment).

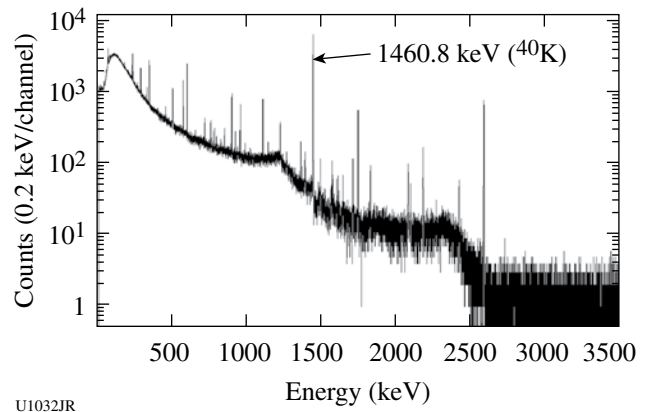


Figure 120.120
 γ -background spectrum recorded by the germanium detector during a 10-h period before high-yield shots.

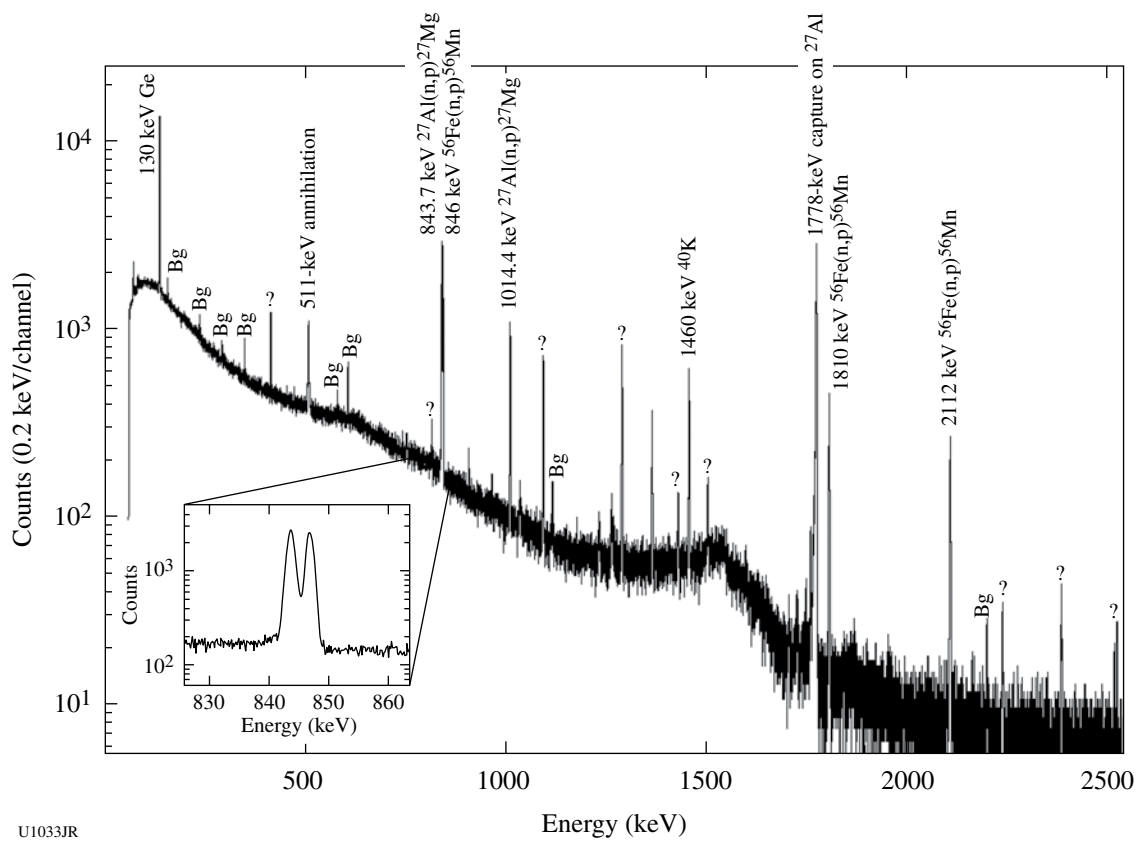


Figure 120.121
 γ spectrum recorded by the germanium detector during a 64-min period after shot 54446 (see text for details).

Some γ rays present in the background spectrum were found and labeled “Bg.” They were caused only by natural radioactivity and not related to the DT shot. Unknown γ rays were present in the spectrum and have to be identified. Data analysis is still in progress in France. The zoom in Fig. 120.121 shows that we can separate closely spaced γ rays thanks to the high resolution of the germanium detector.

As for the γ -dose-rate measurements, these results will be useful in constraining our simulations. Indeed, not all materials of the environment are well known (exact concrete composition, for example), and data from γ spectroscopy will give us some idea of the main radionuclei responsible of γ background after high-neutron-yield shots.

Two New Neutron-Imaging Systems on OMEGA: Neutron imaging system experiments by CEA have been conducted on OMEGA for many years. For the LMJ nuclear diagnostics development, we have tested several imaging techniques based on the use of thick penumbral apertures. It was shown³⁹ that design and alignment are essential for measurement quality. We also experimented with several detector designs and configurations using segmented scintillators,⁴⁰ or capillary arrays filled with a high-refractive-index liquid scintillator.^{41,42} The latter was found to be very efficient and gave a high spatial resolution.

We designed and assembled a large (150-mm entrance diameter) neutron imaging system (LNIS) based on the capillary-filled technique. A large capillary array had to be composed by assembling four arrays of 5-cm length. A large optical-fiber taper reducer (150/75 mm) collected light generated in the scintillator sealed in the capillaries to a fast and large light amplifier (75-mm diameter). This amplifier allows for time gating down to 12 ns with accurate timing precision and therefore makes it possible to select light generated by 14-MeV neutrons interacting with the scintillator material. A second optical fiber taper (75/50 mm) matched the amplifier diameter to a cooled charge-coupled device (CCD) 2084 \times 2084 pixels of $24 \mu\text{m}^2$ (see Fig. 120.122). Two rotations were added to the system to allow for detector autocollimation on the neutron line-of-sight (LOS) path.

Our aim was to test this detector on OMEGA during National Ignition Campaign (NIC) shots. Following the OMEGA qualification procedure (starting in February 2008 with a Preliminary Design Review), we were able to implement this camera using a 13-m LOS on the May 2009 NIC campaign. This detector was placed in the La Cave area. Using this LOS, we obtained a good shielding from scattered neutrons and

γ rays generated in the Target Bay; also, by using our usual penumbral aperture⁴³ at this distance, we were able to obtain a larger magnification ratio and, therefore, a smaller resolution (down to $15 \mu\text{m}$) with this capillary technique detector. Alignment was performed by using our laser technique (for details see Ref. 44) with the alignment station placed on the Target Bay floor at 8 m.

The detector was characterized on an accelerator-generated 14-MeV neutron source and on a Co⁶⁰ gamma-ray source. The images obtained are shown in Fig. 120.123. We note that the capillary assembly is clearly visible. We also distinguish four black spots that correspond to capillaries destroyed during manufacturing. The top-left part of the image is more intense than the rest of the image by a factor of 2 due to light amplifier

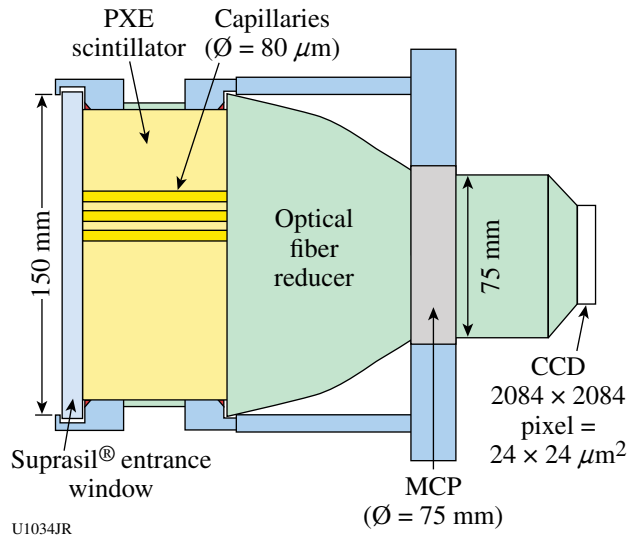


Figure 120.122
LNIS neutron detector scheme.

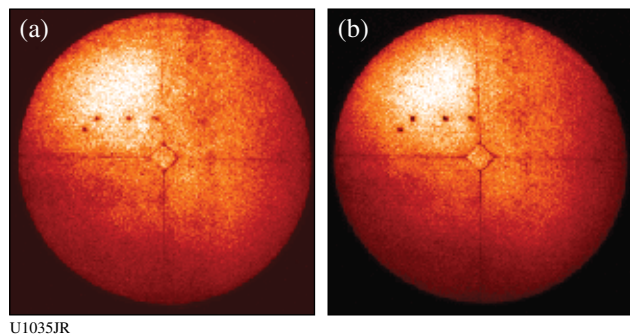


Figure 120.123
(a) Neutron flat-field image yield $8.5 \times 10^3 \text{ n/cm}^{-2}$; (b) Co⁶⁰ γ -rays flat-field image.

inhomogeneity. There is a good agreement between these images, showing that detector response is similar in neutron and γ rays. At low neutron yield (see Fig. 120.124), we were able to register individual proton recoil tracks with a range of about $625 \mu\text{m}$, consistent with detector resolution for 14-MeV neutrons.⁴³

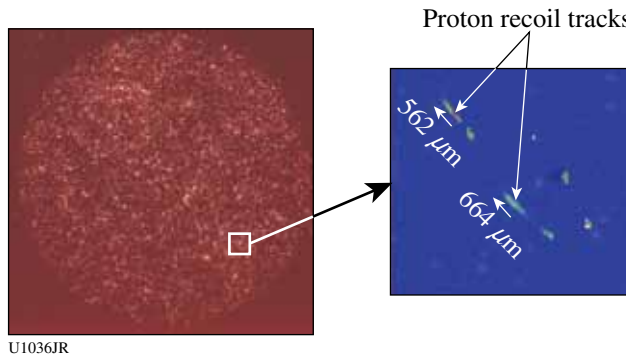


Figure 120.124
14-MeV neutrons image obtained on an accelerator (yield = 53 n/cm^2).

We were able to register ten penumbral images and three flat-field images on the CCD during the two days of target shots. Some shots were dedicated to amplifier time-gating adjustment on DT neutron time of flight. A sample raw penumbral image obtained for shot 54466 at 1.15×10^{13} neutrons is shown in Fig. 120.125(a). In Fig. 120.125(b), one can see that the black spots do not alter image quality since they are not in a region that contains image information. The spots are not visible after flat-fielding the image. The image was then unfolded using our autocorrelation method⁴⁵ [see Fig. 120.126(a)]. In that case, the unfolded image was not corrected from optical transport image distortions. In Fig. 120.126(b) we plotted the vertical and horizontal lineout showing that the source diameter was about $50\text{-}\mu\text{m FWHM}$. Figure 120.127(a) shows an image resulting from the superposition of a 2- to 10-keV x-ray image with a neutron image contour obtained for shot 54466. Figure 120.127(b) is also a superposition of an x-ray image from 7 keV to 9 keV with the same neutron image contour. We see that both images are consistent in shape and size.

A small neutron imaging system (SNIS) was also developed this past year. This system is based on a detector that was specifically designed for low-neutron-yield shots (10^9 to 10^{10} neutrons/ 4π). This detector was implemented at the rear port of the TIM-6 at 4 m from TCC. As for the previous one, this detector is based on a scintillator-filled capillary array. High sensitivity is obtained primarily by the fact that this camera does not contain any optical-fiber reducer between the capil-

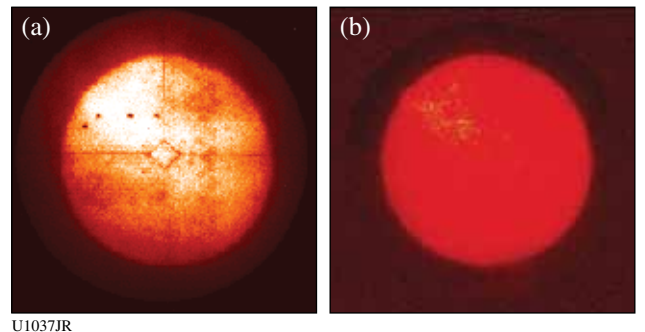


Figure 120.125
(a) Raw image of a DT implosion (shot 54466) yielding 1.15×10^{13} neutrons;
(b) flat-fielded image.

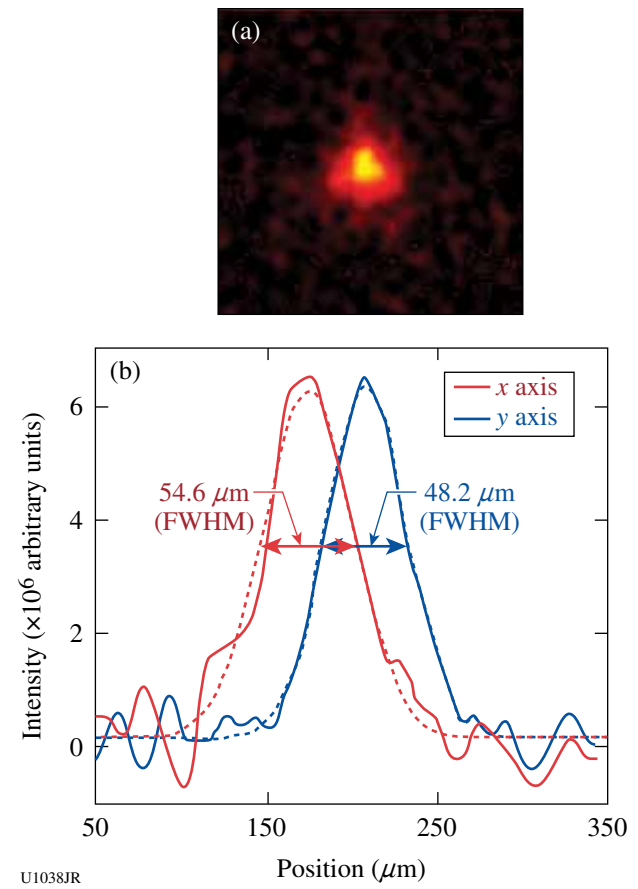


Figure 120.126
(a) Unfolded image using autocorrelation method⁴² (SNR = 16); (b) vertical and horizontal lineouts.

laries and the light amplifier (see Fig. 120.128). The entrance diameter is 40 mm. This detector was also characterized on an a Co⁶⁰ γ -ray source and measurements showed that efficiency is $4\times$ lower than for the traditional NIS. At this distance, the

magnification ratio is smaller; therefore achievable resolution is larger ($43 \mu\text{m}$). At 4 m from TCC, the neutron fluence is 4× higher than at 8 m. The aperture type and alignment technique are the same as used for the larger NIS.

This detector was activated on 16 June shots for indirect-drive, deuterium-filled targets. We were able to register an image on shot 54747 with a neutron yield of 1.37×10^{10} neutrons/ 4π [Fig. 120.129(a)]. In this image, one can see that the statistics are quite low compared to the LNIS image. To reach a reasonable signal-to-noise ratio (SNR) with the autocorrelation technique, the resolution had to be degraded to $54 \mu\text{m}$ in the unfolded image [Fig. 120.129(b)]. This last image reveals a noncircular shape. This observation is contrary to the circular source (caused by the implosion symmetry) that would be expected along the hohlraum axis. This result could be due to source misalignment in the aperture field of view, or aperture misalignment itself, or

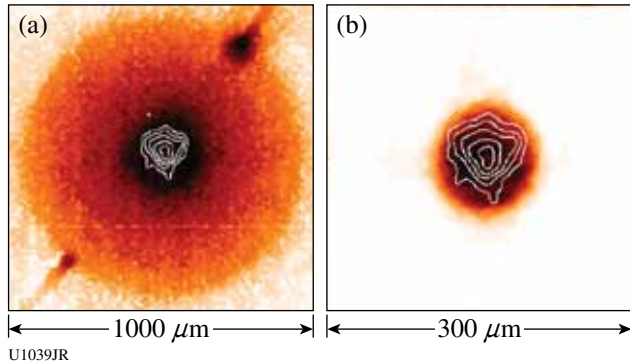


Figure 120.127
(a) Neutron (contours) and x-ray (2- to 10-keV) image superposition; (b) neutron (contours) and x-ray (7- to 9-keV) image superposition.

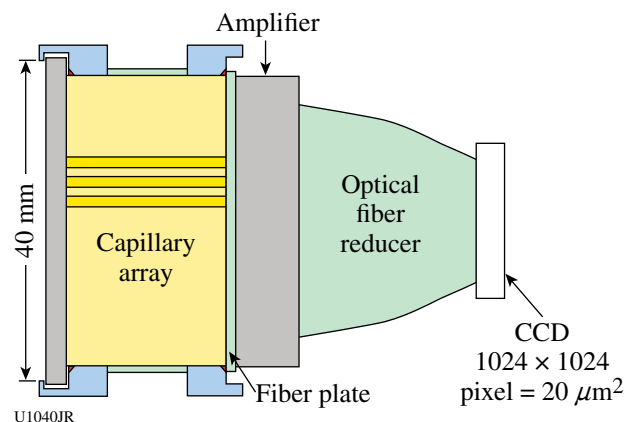


Figure 120.128
SNIS neutron detector scheme.

due to optical coupling between the light amplifier and the fiber plate, which was found imperfect after detector tests. Nevertheless, this camera had demonstrated its particular high sensitivity to low-neutron-yield shots.

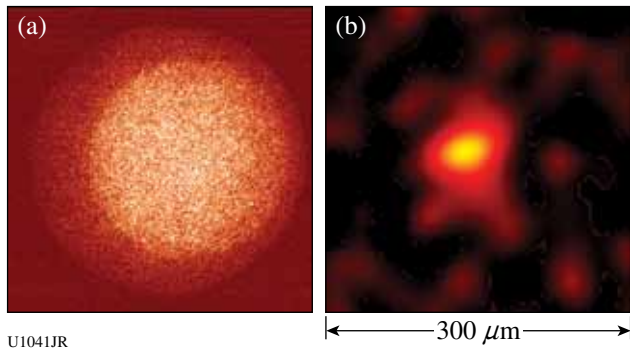


Figure 120.129
(a) Raw image of DD implosion (shot 54747) yielding 1.37×10^{10} neutrons;
(b) unfolded image (SNR = 10, resolution = $54 \mu\text{m}$).

Neutron-imaging measurements were obtained for the first time with $15\text{-}\mu\text{m}$ resolution on OMEGA during the May 2009 NIC campaign. We successfully tested the first part of the LMJ-NIS detector design. This detector resolution may now help us to discriminate the anisotropy in the neutron source linked to the driver energy balance, but this will require specific dedicated experiments.

The first neutron image on an indirect-drive shot was registered with $54\text{-}\mu\text{m}$ resolution. This last image was a milestone for CEA-NIS, which is now able to register images with resolution from $43 \mu\text{m}$ to $15 \mu\text{m}$ and detection threshold from a few 10^9 until the maximum accessible yields on OMEGA.

Next year's experiments will be dedicated to indirect-drive shots and, more particularly, to improving optical coupling between a fiber plate and a light amplifier. This will probably improve light collection and detector sensitivity. Concerning LNIS, a new light amplifier and a new one-block capillary array will be implemented.

Ablative Rayleigh–Taylor Stabilization Mechanisms Experiment: Ablative Rayleigh–Taylor growth measurements in laminated samples were obtained on OMEGA on 17 June 2009. The experimental platform consisted of a gas-filled, 1.2-mm-diam hohlraum along with side-on and face-on radiography x-ray sources (Fig. 120.130).

Rayleigh–Taylor growth measurements were obtained using face-on radiography and are in good agreement with 2-D hydrodynamic simulations based on published theoretical and numerical predictions.⁴⁶ Different behavior was found for homogeneous and laminated samples (Fig. 120.131), the latter showing a strong reduction of the initial perturbation mode.

Side-on radiography shows the absence of Rayleigh–Taylor spikes in the case of laminated samples (Fig. 120.132), while the acceleration was found to be identical for both kinds of samples.

These first experimental measurements strongly motivate new designs using laminated structures for ignition capsules.

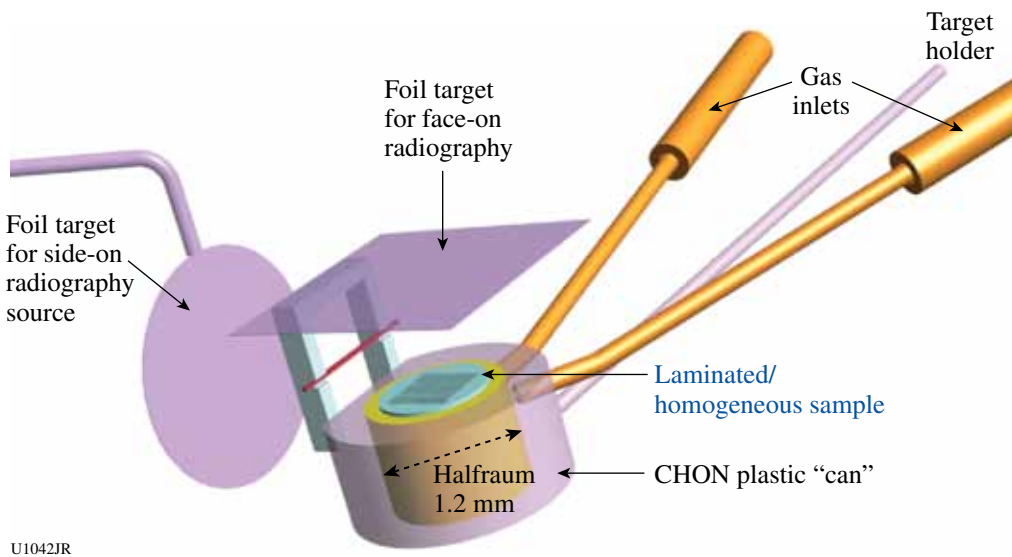


Figure 120.130
Experimental setup.

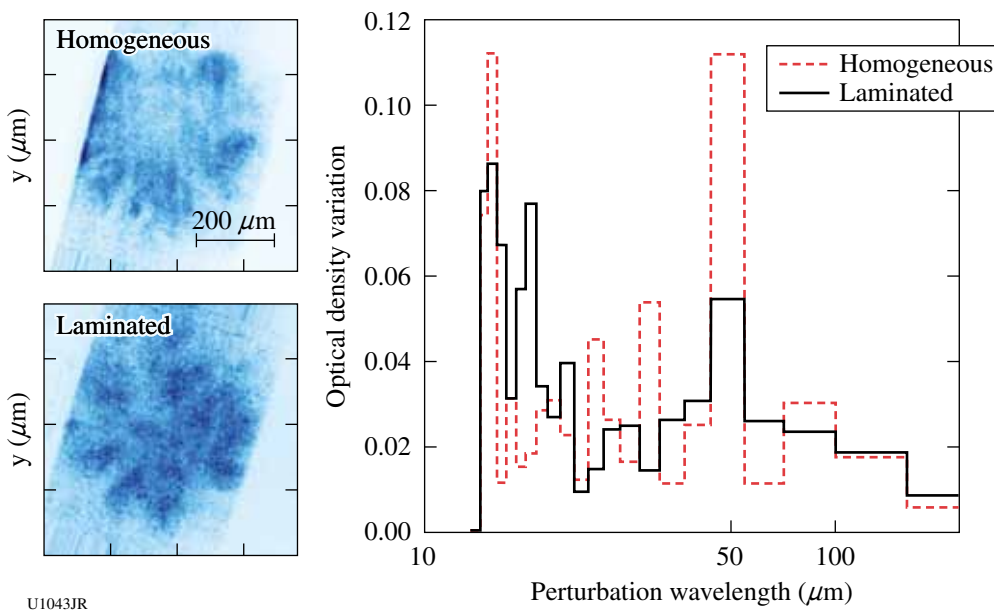


Figure 120.131
Face-on snapshots for homogeneous and laminated samples and corresponding perturbation spectra.

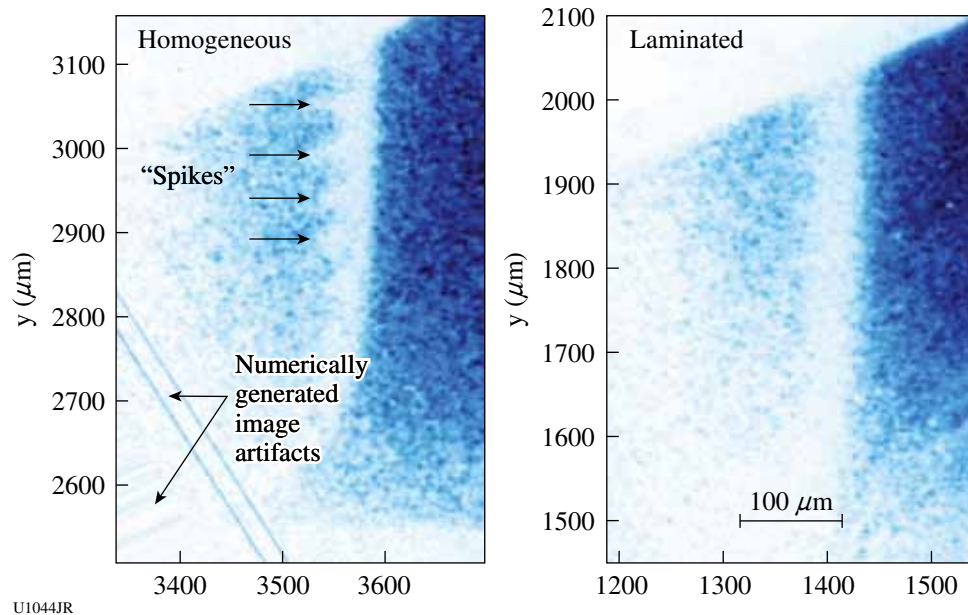


Figure 120.132
Side-on radiographies of (a) homogeneous and (b) laminated samples.

REFERENCES

1. S. H. Glenzer *et al.*, Phys. Rev. Lett. **90**, 175002 (2003).
2. H. J. Lee, P. Neumayer, J. Castor, T. Döppner, R. W. Falcone, C. Fortmann, B. A. Hammel, A. L. Kritchler, O. L. Landen, R. W. Lee, D. D. Meyerhofer, D. H. Munro, R. Redmer, S. P. Regan, S. Weber, and S. H. Glenzer, Phys. Rev. Lett. **102**, 115001 (2009).
3. L. Willingale *et al.*, Phys. Rev. Lett. **96**, 245002 (2006); L. Willingale *et al.*, Phys. Rev. Lett. **102**, 125002 (2009).
4. A. L. Lei *et al.*, Phys. Plasmas **16**, 056307 (2009).
5. G. Li *et al.*, Phys. Rev. Lett. **100**, 125002 (2008).
6. C. K. Li, F. H. Séguin, J. A. Frenje, J. R. Rygg, R. D. Petrasso, R. P. J. Town, P. A. Amendt, S. P. Hatchett, O. L. Landen, A. J. Mackinnon, P. K. Patel, V. A. Smalyuk, T. C. Sangster, and J. P. Knauer, Phys. Rev. Lett. **97**, 135003 (2006).
7. C. K. Li, F. H. Séguin, J. A. Frenje, J. R. Rygg, R. D. Petrasso, R. P. J. Town, P. A. Amendt, S. P. Hatchett, O. L. Landen, A. J. Mackinnon, P. K. Patel, M. Tabak, J. P. Knauer, T. C. Sangster, and V. A. Smalyuk, Phys. Rev. Lett. **99**, 015001 (2007).
8. C. K. Li, F. H. Séguin, J. A. Frenje, J. R. Rygg, R. D. Petrasso, R. P. J. Town, O. L. Landen, J. P. Knauer, and V. A. Smalyuk, Phys. Rev. Lett. **99**, 055001 (2007).
9. C. K. Li, F. H. Séguin, J. R. Rygg, J. A. Frenje, M. Manuel, R. D. Petrasso, R. Betti, J. Delettrez, J. P. Knauer, F. Marshall, D. D. Meyerhofer, D. Shvarts, V. A. Smalyuk, C. Stoeckl, O. L. Landen, R. P. J. Town, C. A. Back, and J. D. Kilkenny, Phys. Rev. Lett. **100**, 225001 (2008).
10. C. K. Li, F. H. Séguin, J. A. Frenje, R. D. Petrasso, P. A. Amendt, R. P. J. Town, O. L. Landen, J. R. Rygg, R. Betti, J. P. Knauer, D. D. Meyerhofer, J. M. Soures, C. A. Back, J. D. Kilkenny, and A. Nikroo, Phys. Rev. Lett. **102**, 205001 (2009).
11. R. D. Petrasso, C. K. Li, F. H. Séguin, J. R. Rygg, J. A. Frenje, R. Betti, J. P. Knauer, D. D. Meyerhofer, P. A. Amendt, D. H. Froula, O. L. Landen, P. K. Patel, J. S. Ross, and R. P. J. Town, Phys. Rev. Lett. **103**, 085001 (2009).
12. J. R. Rygg, F. H. Séguin, C. K. Li, J. A. Frenje, M. J.-E. Manuel, R. D. Petrasso, R. Betti, J. A. Delettrez, O. V. Gotchev, J. P. Knauer, D. D. Meyerhofer, F. J. Marshall, C. Stoeckl, and W. Theobald, Science **319**, 1223 (2008).
13. C. K. Li, F. H. Séguin, J. A. Frenje, J. R. Rygg, R. D. Petrasso, R. P. J. Town, P. A. Amendt, S. P. Hatchett, O. L. Landen, A. J. Mackinnon, P. K. Patel, V. A. Smalyuk, J. P. Knauer, T. C. Sangster, and C. Stoeckl, presented at the 16th Topical Conference on High-Temperature Plasma Diagnostics, Williamsburg, VA, 7–11 May 2006 (invited).
14. C. K. Li, presented at the Fifth International Conference on Inertial Fusion Sciences and Applications, Kobe, Japan, 9–14 September 2007, Paper ThO4.1 (invited).
15. R. Petrasso, presented at the Program of the 49th Annual Meeting of the Division of Plasma Physics, Orlando, FL, 12–16 November 2007, Paper GI1 4 (invited).
16. C. K. Li, presented at the 50th Annual Meeting of the APS Division of Plasma Physics, Dallas, TX, 17–21 November 2008, Paper BI1 5 (invited).
17. R. D. Petrasso, presented at the 2008 APS April Meeting and HEDP/HEDLA Meeting, St. Louis, MO, 11–15 April 2008, Paper 14HE.00002 (invited).
18. R. D. Petrasso, C. K. Li, F. H. Séguin, J. A. Frenje, M. Manuel, D. Casey, N. Sinenian, M. Rosenberg, H. Rir. Landen, J. R. Rygg, R. P. J. Town, R. Betti, J. Delettrez, J. P. Knauer, F. J. Marshall, D. D. Meyerhofer, V. A. Smalyuk, J. M. Soures, C. A. Back, J. D. Kilkenny, and A. Nikroo,

- presented at the Second International Conference on High Energy Density Physics, Austin, TX, 19–22 May 2009 (invited).
19. C. K. Li, presented at The 8th Pacific Rim Conference on Lasers and Electro-Optics (CLEO/Pacific Rim 2009), Shanghai, China, 30 August–3 September 2009 (invited).
 20. C. K. Li, presented at The Sixth International Conference on Inertial Fusion Sciences and Applications (IFSA 2009), San Francisco, CA, 6–11 September 2009, Paper 5.2.3 (invited).
 21. J. A. Frenje, D. T. Casey, F. H. Séguin, C. K. Li, N. Sinenian, R. D. Petrasso, V. Yu. Glebov, T. C. Sangster, D. D. Meyerhofer, S. Hatchett, S. Haan, C. Cerjan, D. Eder, O. Landen, M. Moran, K. Fletcher, and R. Leeper, presented at the Sixth International Conference on Inertial Fusion Sciences and Applications (IFSA 2009), San Francisco, CA, 6–11 September 2009, Paper 3.6.3 (invited).
 22. C. K. Li, F. H. Séguin, J. A. Frenje, J. R. Rygg, R. D. Petrasso, R. P. J. Town, P. A. Amendt, S. P. Hatchett, O. L. Landen, A. J. Mackinnon, P. K. Patel, V. Smalyuk, J. P. Knauer, T. C. Sangster, and C. Stoeckl, *Rev. Sci. Instrum.* **77**, 10E725 (2006).
 23. H. Chen, S. C. Wilks, J. D. Bonlie, E. P. Liang, J. Myatt, D. F. Price, D. D. Meyerhofer, and P. Beiersdorfer, *Phys. Rev. Lett.* **102**, 105001 (2009).
 24. J. Myatt, A. V. Maximov, R. W. Short, and D. D. Meyerhofer, presented at the 49th Annual Meeting of the APS Division of Plasma Physics, Orlando, FL, 12–16 November 2007, Paper CO6 1.
 25. W. Theobald, R. Betti, V. A. Smalyuk, K. S. Anderson, J. A. Delettrez, J. A. Frenje, V. Yu. Glebov, F. J. Marshall, D. D. Meyerhofer, J. F. Myatt, R. D. Petrasso, C. Ren, T. C. Sangster, W. Seka, A. A. Solodov, C. Stoeckl, and B. Yaakobi, “Shock-Ignition Experiments on OMEGA and NIF-Relevant Intensities,” submitted to *Physical Review Letters*.
 26. W. Theobald, K. S. Anderson, R. Betti, R. S. Craxton, J. A. Delettrez, J. A. Frenje, V. Yu. Glebov, O. V. Gotchev, J. H. Kelly, C. K. Li, A. J. Mackinnon, F. J. Marshall, R. L. McCrory, D. D. Meyerhofer, J. F. Myatt, P. A. Norreys, P. M. Nilson, P. K. Patel, R. D. Petrasso, P. B. Radha, C. Ren, T. C. Sangster, W. Seka, V. A. Smalyuk, A. A. Solodov, R. B. Stephens, C. Stoeckl, and B. Yaakobi, “Advanced-Ignition-Concept Exploration on OMEGA,” *Plasma Phys. Control. Fusion* **51**, 124052 (2009).
 27. D. H. Froula, L. Divol, R. L. Berger, R. A. London, N. B. Meezan, D. J. Strozzi, P. Neumayer, J. S. Ross, S. Stagnitto, L. J. Suter, and S. H. Glenzer, *Phys. Rev. Lett.* **101**, 115002 (2008).
 28. D. H. Froula, *Phys. Rev. Lett.* **103**, 045006 (2009).
 29. E. L. Dewald *et al.*, *Rev. Sci. Instrum.* **79**, 10E903 (2008).
 30. T. Döppner, O. L. Landen, H. J. Lee, P. Neumayer, S. P. Regan, and S. H. Glenzer, *High Energy Density Phys.* **5**, 182 (2009).
 31. T. Döppner, P. F. Davis, A. L. Kritcher, O. L. Landen, H. J. Lee, S. P. Regan, and S. H. Glenzer, in *Soft X-Ray Lasers and Applications VII*, edited by J. Dunn and G. J. Tallents (SPIE, Bellingham, WA, 2009), Vol. 7451, p. 74510H.
 32. *LLE Review Quarterly Report* **116**, 249, Laboratory for Laser Energetics, University of Rochester, Rochester, NY, LLE Document No. DOE/NA/28302-866 (2008).
 33. H. W. Herrmann, R. M. Malone, W. Stoeffl, S. E. Caldwell, S. C. Evans, J. M. Mack, P. Sanchez, T. Sedillo, C. S. Young, C. J. Horsfield, D. Drew, E. K. Miller, and V. Yu. Glebov, presented at the 17th Topical Conference on High-Temperature Plasmas Diagnostics, Albuquerque, NM, 11–15 May 2008, Paper D35.
 34. H. W. Herrmann, S. C. Evans, J. M. Mack, C. S. Young, C. J. Horsfield, R. M. Malone, E. K. Miller, V. Yu. Glebov, and W. Stoeffl, presented at the 17th Topical Conference on High-Temperature Plasma Diagnostics, Albuquerque, NM, 11–15 May 2008, Paper D34.
 35. E. Miller, presented at The Sixth International Conference on Inertial Fusion Sciences and Applications (IFSA 2009), San Francisco, CA, 6–11 September 2009, Poster 3.10.110.
 36. P. Amendt *et al.*, *Rev. Sci. Instrum.* **66**, 785 (1995).
 37. P. Amendt *et al.*, *Phys. Rev. Lett.* **77**, 3815 (1996).
 38. A. A. Hauer *et al.*, *Phys. Plasmas* **2**, 2488 (1995).
 39. *LLE Review Quarterly Report* **112**, 270, Laboratory for Laser Energetics, University of Rochester, Rochester, NY, LLE Document No. DOE/SF/19460-790 (2007).
 40. L. Disdier, A. Rouyer, D. C. Wilson, A. Fedotoff, C. Stoeckl, J. L. Bourgade, V. Yu. Glebov, J.-P. Garçonnet, and W. Seka, *Nucl. Instrum. Methods Phys. Res. A* **489**, 496 (2002).
 41. L. Disdier, A. Rouyer, A. Fedotoff, J.-L. Bourgade, F. J. Marshall, V. Yu. Glebov, and C. Stoeckl, *Rev. Sci. Instrum.* **74**, 1832 (2003).
 42. L. Disdier, R. A. Lerche, J. L. Bourgade, and V. Yu. Glebov, *Rev. Sci. Instrum.* **75**, 2134 (2004).
 43. L. Disdier, A. Rouyer, I. Lantuejoul, O. Landoas, J. L. Bourgade, T. C. Sangster, V. Yu. Glebov, and R. A. Lerche, *Phys. Plasmas* **13**, 056317 (2006).
 44. *LLE Review Quarterly Report* **116**, 258, Laboratory for Laser Energetics, University of Rochester, Rochester, NY, LLE Document No. DOE/NA/28302-866 (2008).
 45. A. Rouyer, *Rev. Sci. Instrum.* **74**, 1234 (2003).
 46. L. Masse, *Phys. Rev. Lett.* **98**, 245001 (2007).

